POLITECNICO
MILANO 1863

SCUOLA DI INGEGNERIA INDUSTRIALE
E DELL'INFORMAZIONE

Experimental investigation of microfibers dispersion in fully developed turbulent channel flow

TESI DI LAUREA MAGISTRALE IN
MECHANICAL ENGINEERING-INGEGNERIA
MECCANICA

Author: **Silvia Sambuca**

Student ID:	10599856
Advisor:	Gianluca Montenegro
Co-advisor:	Soldati Alfredo
Academic Year:	2021-22

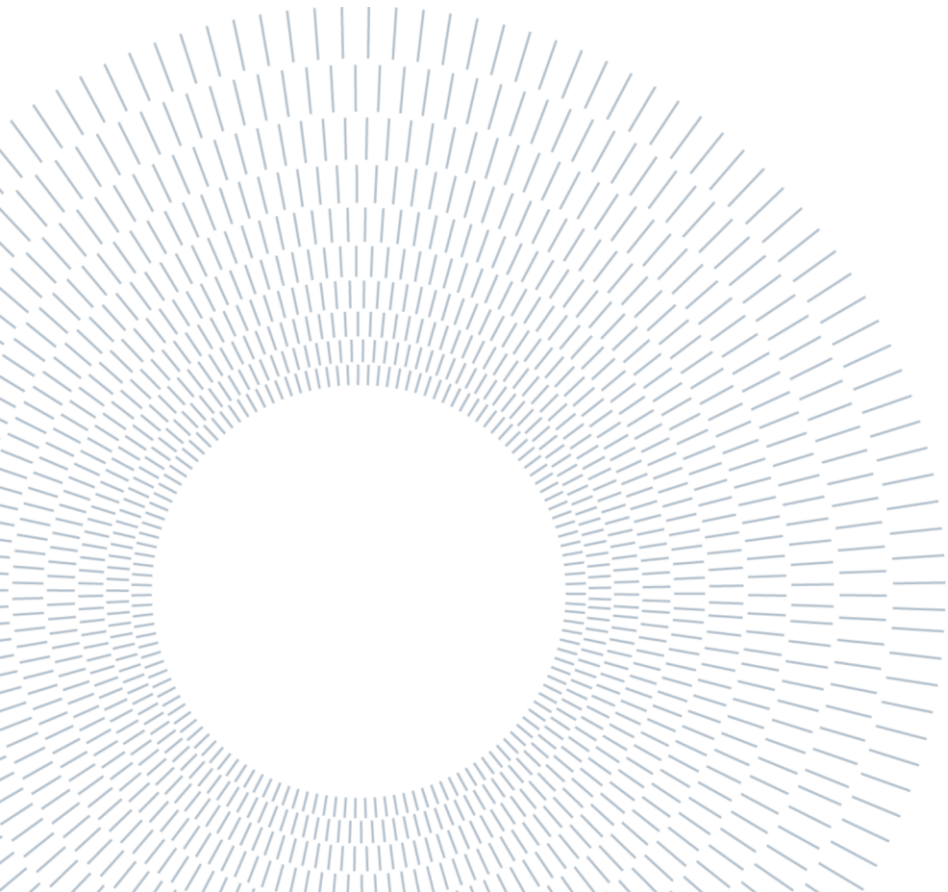

Abstract

In this thesis the turbulence in a turbulent channel flow was investigated to guarantee the fully developed channel flow condition. The experimental facility is the TU Wien Turbulent Water Channel, consisting of a closed water channel and the experiments are conducted at the 180,360 and 720 friction Reynolds. The velocity measurements are conducted employing two-dimensional Particle Image Velocimetry (PIV), optic technique able to obtain instantaneous velocity fields through the evaluation of particle displacements. Thus four window sizes and three time resolutions for the PIV measurements are investigated, resulting in twelve combinations for low and intermediate Reynolds numbers and four for high Reynolds number. To perform the assessment of fully developed channel condition for the TU channel, turbulence statistics are derived from the measurements: mean streamwise velocity profiles, streamwise and normal velocity fluctuations, Reynolds stresses, skewness and flatness profiles of the fluctuations were computed and compared to the current data available in the literature. The results show a good agreement with available DNS and experimental data: any statistic discrepancy related to the uncertainty of the measurement technique is then discussed in the thesis. In addition, three experiments for fiber laden flow were conducted at the same friction Reynolds and consequently a fiber reconstruction from acquired images was proposed for the case of Re_τ=200. The fibers are neutrally buoyant rods, with an aspect ratio of 120 and show a certain curvature. The reconstruction consists of two phases: a discrimination phase and a modeling phase. First the fibers were discriminated, i.e. they are detected in the recorded image despite the high density of tracers and other spurious elements in the channel through intensity and area thresholds. Consequently the fiber is reconstructed using a MATLAB in-house built code based on light intensity and orientation of the fiber.

Key-words: Turbulent water channel, microfibers, PIV

Abstract in lingua italiana

In questa tesi è stata studiata la turbolenza in un flusso di canale turbolento per garantire la condizione *fully developed channel flow*. Il canale analizzato è il TU Wien Turbulent Water Channel, costituito da un canale ad acqua chiuso. Gli esperimenti sono stati condotti ad un valore di *friction* Reynolds di 180,360 e 720. Le misurazioni di velocità sono state condotte utilizzando *Particle Image Velocimetry* (PIV) bidimensionale, tecnica ottica in grado di ottenere campi di velocità istantanei attraverso la valutazione degli spostamenti delle particelle. Dunque, sono state studiate quattro dimensioni per la finestra di interrogazione e tre risoluzioni temporali per le misurazioni PIV, risultando in dodici combinazioni per i numeri di Reynolds basso ed intermedio e quattro per il numero di Reynolds più alto. Per dimostrare la condizione di *fully developed channel flow* per il canale della TU, le statistiche turbolente sono state ottenute attraverso le misurazioni: i profili di velocità media, le fluttuazioni della velocità normale e assiale, le sollecitazioni di Reynolds, i profili di asimmetria e planarità delle fluttuazioni turbolente sono stati calcolati e confrontati con gli attuali dati disponibili in letteratura. I risultati mostrano una buona concordanza con i dati DNS e sperimentali disponibili attualmente: qualsiasi discrepanza delle statistiche correlata all'incertezza della tecnica di misurazione viene poi discussa nella tesi. Inoltre, sono stati condotti tre esperimenti per il caso di flusso turbolento in presenza di fibre a valori comparabili di *friction Reynolds* e poi è stata proposta una ricostruzione della fibra dalle immagini acquisite per il caso di Re_τ=200. Le fibre sono a galleggiabilità neutra, con un *aspect ratio* di 120 e mostrano una certa curvatura. La ricostruzione consiste in due fasi: una fase di discriminazione e una fase di modellazione. Prima le fibre sono state discriminate, cioè vengono rilevati nell'immagine registrata nonostante l'elevata densità di traccianti e altri elementi spuri nel canale attraverso soglie di intensità e area. Infine, la fibra viene ricostruita utilizzando un codice MATLAB in base all'intensità della luce e all'orientamento della fibra.

Parole chiave: Canale turbolento, microfibre, PIV

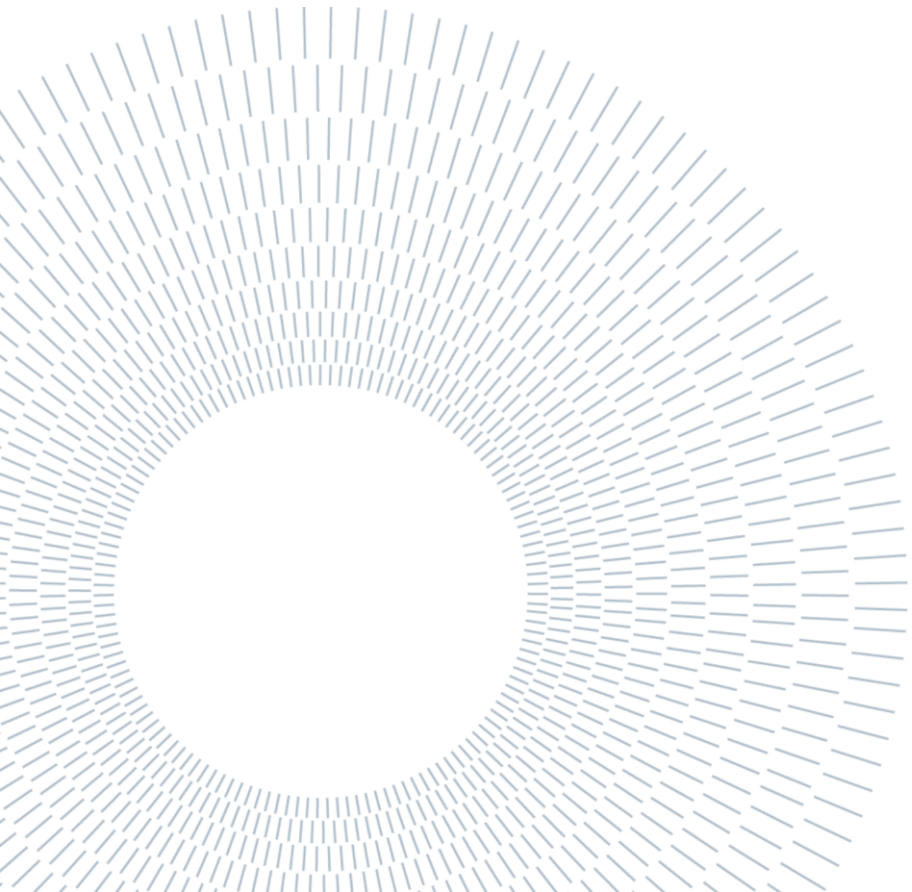

Contents

1 Introduction

Fully developed channel flow has been studied extensively for almost a century now to increase the understanding of the mechanics of wall bounded turbulent flows through either direct numerical simulations (DNS) and/or experimentally. Nikuradse (1929) and Reichardt (1938) were among the first to investigate this configuration of turbulence: Nikuradse's measurements were referred to the mean flow only, instead Reichardt reported velocity fluctuations in the streamwise and normal directions. Only in 1948 Laufer ((Laufer, 1948)) documented more detailed turbulence statistics. Despite the large amount of documentation being available and the relatively simple flow, up to nowadays there is still poor agreement among the reported measurements, even in low-order statistics as the turbulence intensities, especially in the vicinity of the wall. In addition, only a few statistical quantities or physical mechanism of turbulence in internal (pipes and channels) or external (boundary layers) flows are recognized as universal, such as: the spanwise scaling of the near-wall vortical structure (Kline et al. (1967)), the mean velocity scaling in the viscous buffer region ((Nickels & Marusic, 2001)) and the occurrence of the peak production of energy in the same region ((Klebanoff, 1955));so this means that a basic understanding of the entire flow field is not yet totally reached, which is needed in order to improve the engineering of vehicles and transport systems that society heavily depends upon at this point in time [(Monty & Chong, 2009)].

In addition to the study of wall bounded turbulence, this work is committed into the investigation of non-axisymmetric plastic fibers in a turbulent channel flow. The study of these anisotropic particles is of particular interest for both industrial and environmental applications. Industrial processes include pulp making and paper making [(Lundell, Söderberg, & Alfredsson, 2011)], pharmaceutical processing [(Erni, Cramer, Marti, Windhab, & Fischer, 2009)] and soot emission from combustion processes [(Moffet & Prather, 2009)]. Instead, environmental ones include dispersion of pollen species in the atmosphere [(Lilach & René, 2011)], the dynamics of icy clouds [(Heymsfield , 1977)], the cycle of plankton and marine snow in the oceans [(Pedley & Kessler, 1992)] and micro-fiber pollution in ocean.

Particular attention must be given to the latter which represent one of the main concerns in modern times. In fact, the pervasive distribution of microplastics (MPs)

has become a significant global concern since MPs were found even in the most remote reaches of the world [(Ross, Chastain, Vassilenko, & al, 2021)]. Of these, fibres represent a notable shape encountered in sediments and seawater samples and have become more and more prominent since the global fiber production, both synthetical and natural, has double in the past 20 years, reaching 107 million metric tons in 2018 [(Suaria, Achtypi, Perold, & al, 2020)]. Microplastics (i.e., any particle of synthetic plastic smaller than 5 mm) were detected in Arctic pack ice, seawater and seafloor sediments. In addition, ingestions of these particles have been documented across various habitats around the world and across all levels of the marine food web. Report of MPs in seafood have, in fact, raised concerns about the potential for human ingestion and possible health effects. On the other hand, the data related to microplastics' distribution and scale of contamination are scant and the information about the mechanisms of diffusion are limited. This is mainly due to the fact that with fibers forces and torques exchanged with the flow depend on each particle orientation. In addition, since fibers are characterized by being not axisymmetric, this could influence their orientation and rotational dynamics [(Voth & Soldati, 2017)].

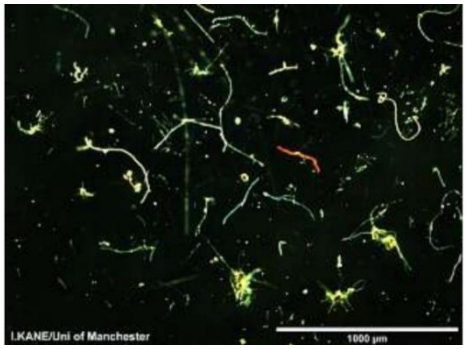

(a) Extracted in Marine sediments.

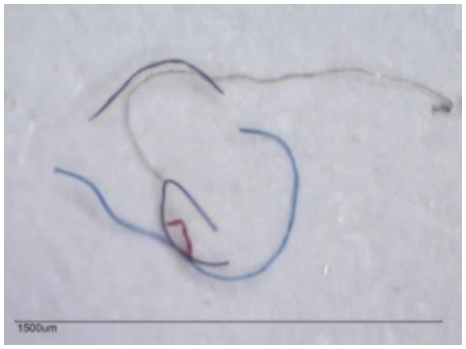

(b) Extracted from Water sample in Blue Hill Bay in the Gulf of Maine.

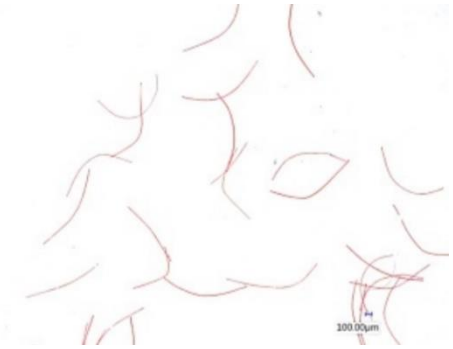

(c) Non-axisymmetric fibers used in this study.

Figure 1.1-1: Microscope photograph of microfibers.

So the fibers used in this study (Figure 1.1-1(c from (Alipour, De Paoli, Ghaemi, & Soldati, 2021)) share similarities in terms of asymmetry in shape with real microfibers obtained from marine sediments (Figure 1.1-1(a from (Kane & al, 2020)) and sea water (Figure 1.1-1(b from (www.theguardian.com)).

1.1 Scope and structure of the thesis

The aim of this thesis is therefore: (1)the investigation of turbulence in a turbulent channel flow configuration carried out in the TU Wien Turbulent Water Channel, which is a gravity driven, large aspect ratio facility, through turbulence statistics derived from 2D Particle Image Velocimetry measurements;(2)the study of the geometrical properties of the plastic microfibers in the water channel reconstructed by employing in-house built MATLAB codes by using images coming from acquisition system.

The database of this work then consist in a total of two sets of three experiments each, conducted at 180,360 and 720 friction Reynolds distinguishing among unladen and fiber laden flows.

The structure of this thesis is organised as follows:

- In 2 a scientific background is given: an overview on the turbulent channel flow configuration, together with the main formula employed and main turbulence statistic are presented. In addition in the chapter an outline on the principal models for anisotropic particles according to size, density and aspect ratio is given;
- In 3 the methodology used for the realization of this work is described: starting from a brief excursus on the principals of PIV, in which there are information on the physical recording, illumination devices and the mathematical backgrounds together with the uncertainty and resolution; a more in detail excursus on how the process of discretization and modeling of the fibers were conducted is presented;
- In 4 the experimental set-up is described: after a small window on the dry fiber imaging set-up and presentation on the studied fiber properties, the experimental facility, particles parameters, image acquisition system and PIV setting parameter are presented;
- In 5 the results regarding the reconstruction of the fibers in the fiber laden flow are given in terms of quality of the reconstruction (images will be shown) and properties of the fibers, as fiber length L_f and normalized curvature k*, will be derived from the reconstruction and shown in terms of probability density functions (PDF);
- In 6 the turbulence statistics are studied for each case of friction Reynolds number: starting from first order statistics, mean streamwise velocity and streamwise and normal velocity fluctuations, also the Reynolds stresses (second

order statistics) and skewness and flatness of the fluctuations (third and fourth order statistics respectively) will be discussed. Finally the still in doubt universality of these turbulence statistics will be checked comparing the result data from this thesis;

- In 7, conclusions and suggested future works of this study are discussed.

2 Scientific background

Before presenting the methodology followed for the realization of this thesis, it is of extreme importance an overview of the scientific background. Therefore, this chapter is going to commit into a brief presentation of the turbulence in channel flow theory and on a review on the different ways of modelling anisotropic particles, from simpler to more complex ones. Since the measurements were carried out in correspondence of the test section situated at 8.5 m downstream the entrance in a 10 m long channel, the condition of fully developed flow condition is assured, therefore the rather simpler case of fully developed channel flow is presented in the next subsection.

2.1 Channel flow

2.1.1 Description of the flow

Most turbulent flows are bounded by one or more solid surfaces and one of simpler flows is certainly the fully developed channel flow which is an internal flow. Considering a rectangular duct (see Figure 2.2-1) with length L, width b and large aspect ratio ($b/\delta >> 1$, where δ, as shown in Figure 2.2-1, is half of the channel's height), the mean flow is mainly in the axial direction (x in the figure), with the mean velocity varying in the cross-stream direction (y in the figure). The aspect ratio is large, therefore the flow can be considered, remote from the end walls, statistically independent of z. The velocities in the three coordinates are ($\boldsymbol{U}$,$\boldsymbol{V}$,$\boldsymbol{W}$) with associated fluctuations ($\boldsymbol{u}$,$\boldsymbol{v}$,$\boldsymbol{w}$), where the mean span-wise velocity ($\boldsymbol{W}$) is zero.

As stated, only the fully developed region is considered (large x), thus the flow is statistically stationary and one-dimensional, with velocity statistics depending only on the normal direction (y). In addition, the behaviour of the flow is statistically symmetric about the mid-plane.

The Reynold numbers considered to characterize the flow are given in (2.1) and (2.2):

$$\boldsymbol{Re} \equiv (2\delta)\overline{U}/\nu, \tag{2.1}$$

$$\boldsymbol{Re_0} \equiv U_0\delta/\nu, \tag{2.2}$$

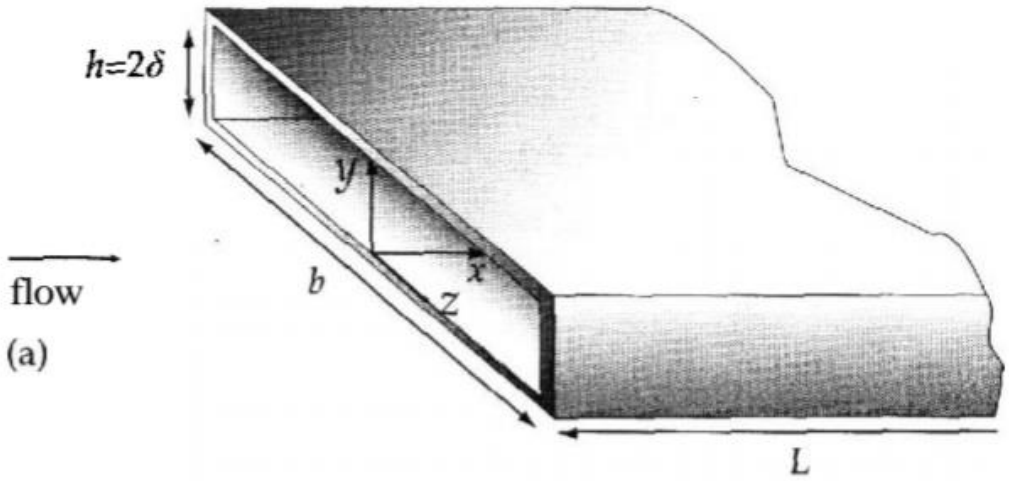

Figure 2.1-1: Sketch of channel flow (Pope, 2018).

Where ν is the kinematic viscosity, U_0 is the velocity in the centre of the channel and $\overline{U}$ is the bulk velocity, defined by Equation (2.3):

$$\overline{\boldsymbol{U}} \equiv \frac{1}{\delta}\int_0^{\delta}\langle U\rangle d\, y, \tag{2.3}$$

The flow is laminar for values of bulk Reynolds Re < 1350 and fully turbulent for Re > 1800, nevertheless transitional effects are evident up to Re = 3000.

Applying the mean continuity equation, the lateral (direction y) and axial mean-momentum equations (x) (see (Pope, 2018) for deep discussion on the calculations), a balance of forces in the channel is obtained that states that the axial normal stress gradient is balanced by the cross-stream shear-stress gradient (Equation (2.4)):

$$\frac{\boldsymbol{d\tau}}{\boldsymbol{dx}} = \frac{dp_w}{dy}, \tag{2.4}$$

Where p_w is the mean pressure on the bottom wall (i.e., $p_w=\langle p(x,0,0)\rangle$). Where the total shear stress $\tau(y)$ varying in the normal direction to the wall can be evaluated as shown in Equation (2.5):

$$\boldsymbol{\tau} = \rho\nu\frac{d\langle U\rangle}{dy} - \rho\langle uv\rangle, \tag{2.5}$$

So, $\tau(y)$ is the sum of the viscous stress (first term) and the Reynolds stress (second term). Since p_w and τ_w depend on x and y only respectively, from Equation (2.4) it is evident that both gradients are constant.

2.1.2 Near-wall region

The boundary conditions state that at the wall the streamwise velocity U(x,t)=0, then the wall shear stress τ_w is due to the viscous contribution only (i.e., $\rho\nu d\langle U\rangle/dy$). Considering that viscous stress dominates at the wall, the two parameters of viscosity ν and wall shear τ_w are relevant. So, from these quantities it appears necessary to construct viscous scales that are suitable velocity scales and lengthscales in the near-wall region:

$$\boldsymbol{u_\tau} \equiv \sqrt{\frac{\tau_w}{\rho}}, \tag{2.6}$$

$$\boldsymbol{\delta_\nu} \equiv \nu\sqrt{\frac{\rho}{\tau_w}} = \frac{\nu}{u_\tau}, \tag{2.7}$$

Equation (2.6) and Equation (2.7) define the *friction velocity* and *viscous lenghtscale* respectively.

The Reynolds number based on the viscous scales is identically unity, therefore the definition of a new parameter is necessary: the *friction Reynolds* number is defined in (2.8).

$$\boldsymbol{Re_\tau} \equiv \frac{u_\tau\delta}{\nu} = \frac{\delta}{\delta_\nu}, \tag{2.8}$$

To easily express the relative importance of viscous and turbulent processes, the distance from the wall measured in viscous lengths can be used (Equation (2.9)):

$$\boldsymbol{y^+} \equiv \frac{y}{\delta_\nu} = \frac{u_\tau y}{\nu}, \tag{2.9}$$

The wall units are of great relevance since different regions, or layers, in the channel can be defined on the basis of it: the viscous wall region for $y^+ < 50$, the outer layer for $y^+ > 50$ and the viscous sublayer for $y^+ < 5$. As the name suggests, in the viscous wall region the viscous contribution to the shear stress is significant, instead for the outer layer these direct effect of viscosity is negligible. In particular, for the sublayer the Reynolds shear stress is negligible when compared with viscous stress.

2.1.3 Mean velocity profiles

The mean velocity profile can be written as in Equation (2.10):

$$\langle \boldsymbol{U} \rangle = u_\tau F_0 \left(\frac{y}{\delta}, Re_\tau \right), \tag{2.10}$$

Where F_0 is a universal non-dimensional function to be determined.

In addition it is of relevant importance also the definition of a dynamically important quantity since both the viscous stress and turbulence production are determined by it: the velocity gradient. The latter, as visible from Equation (2.11), is dependent on two lengthscales δ and δ_ν, both representing the appropriate scales for viscous wall region and outer layer respectively.

$$\frac{\boldsymbol{d\langle U \rangle}}{\boldsymbol{dy}} = \frac{u_\tau}{y} \phi \left(\frac{y}{\delta}, \frac{y}{\delta_\nu} \right), \tag{2.11}$$

Where ϕ is a universal non-dimensional function.

In 1925 Prandtl postulated that at high Reynolds number, close to the wall ($y/\delta \ll 1$) there is an inner layer in with the mean velocity profile is determined by the viscous scales only. This implies that the function $\phi(y/\delta_\nu, y/\delta)$ in Equation (2.11) tends asymptotically to a function of y/δ_ν only, as the other scale tends to zero.

If now the adimensionalized velocity $u^+(y^+)$ is derived by integrating Equation (2.12) and dividing by the friction velocity u_τ, *the law of the wall* is obtained:

$$\boldsymbol{u^+} = f_w(y^+), \quad \text{for } y/\delta \ll 1 \tag{2.12}$$

Where f_w is was experimentally verified as universal for channel flow, pipe flow and boundary layers if Reynolds number is not too close to transition and can be determined for small and larger values of y^+.

It can be derived that in the sublayer ($y^+ < 5$) the mean velocity profile shows a linear behaviour (and this is particularly true until $y^+ < 12$), therefore is described by the following relation:

$$\boldsymbol{u}^+ = y^+, \tag{2.13}$$

As said, for large y^+ the viscous effect is little, hence in the Equation (2.11) other than the y/δ, also the dependence of ϕ on the viscosity (through δ_ν) vanishes and the function becomes a constant (denoted by 1/k, i.e., the von Kármán constant). Integrating and dividing again the *log law* can be obtained:

$$\boldsymbol{u}^+ = \frac{1}{k}\ln y^+ + B\,, \tag{2.14}$$

Where common values adopted for k and B are within 5% of respectively 0.41 and 5.2. The log law is particularly suitable for $y^+ > 30$. The transition region between viscosity-dominated region of the viscous sublayer and the turbulence dominated part of log-law region is called *buffer layer*. For the outer region ($y^+ > 50$) from Equation (2.11 only the dependence from the viscous effects vanishes and ϕ becomes only a function of y/δ. The various regions are summarized in Figure 2.1-2:

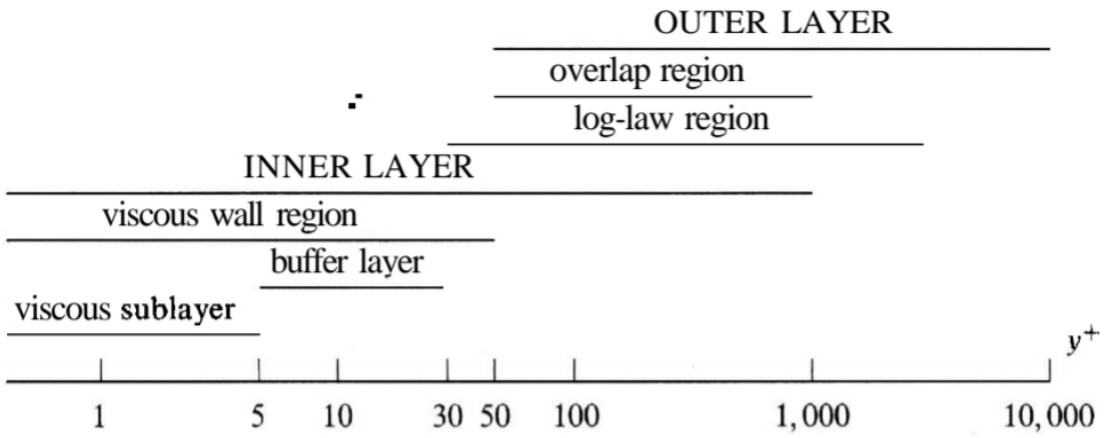

Figure 2.1-2: A sketch showing the various wall regions and layer for turbulent channel flow at high Reynolds number ($Re=10^4$) [41].

2.1.4 Reynolds stresses

A set of important statistics is represented by the Reynolds stresses. They are shown in Figure 2.1-3 dimensionalized by the friction velocity u_τ^2. As noticeable in the viscous wall region ($y^+ < 50$) the most vigorous turbulent activity is contained: indeed both the tangential and normal Reynolds stresses present an absolute peak (minimum for the tangential) for values of wall units lower than 50. So it is therefore interesting to examine more deeply their behaviour in this region.

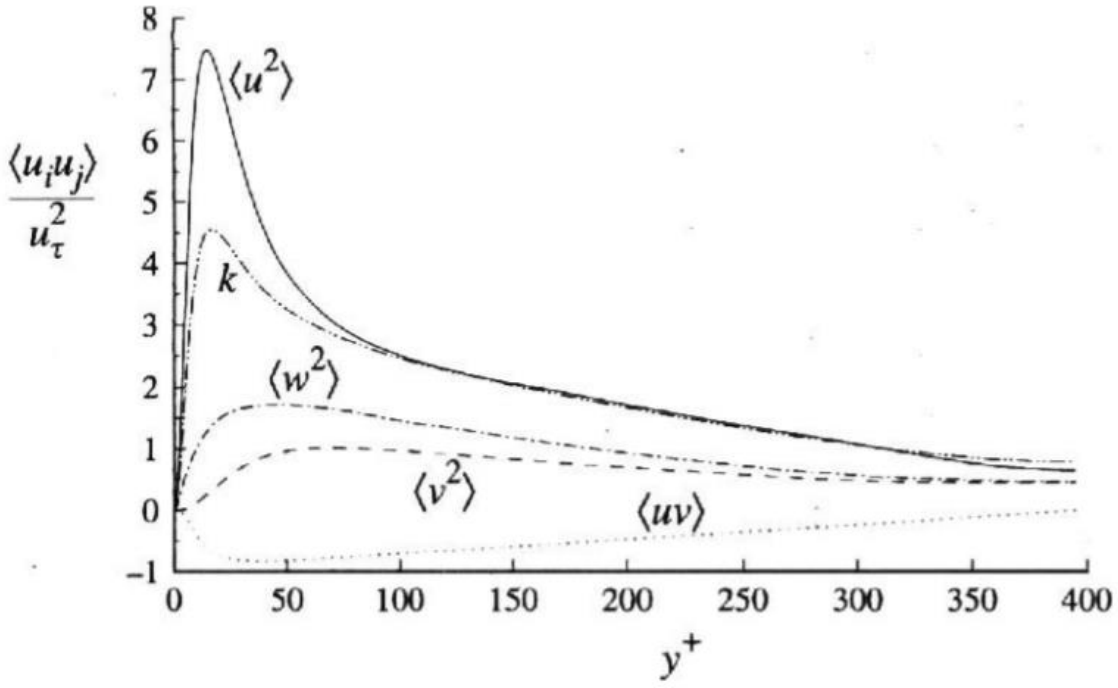

Figure 2.1-3: Reynolds stresses and kinetic energy normalized by u_τ from DNS of channel Bow at Re=13750 [Kim et al.1987].

The velocity fluctuations in a fully developed channel flow are statistically independent from x, z and t. For small y, for those zero-mean random variables the following expressions in Taylor series are valid:

$$\boldsymbol{u} = a_1 + b_1 y + c_1 y^2 + \cdots, \tag{2.15}$$

$$\boldsymbol{v} = a_2 + b_2 y + c_2 y^2 + \cdots, \tag{2.16}$$

$$\boldsymbol{w} = a_3 + b_3 y + c_3 y^2 + \cdots, \tag{2.17}$$

For the no-slip and the impermeability condition, the three coefficients a_1, a_3 and a_2 are null. Furthermore applying the continuity equation for the velocity fluctuations leads to b_2 being zero as well. This result is rather relevant since very close to the wall a *two-component flow* is obtained: this corresponds to a motion in planes parallel to the wall (i.e., u and w are not 0 as v and vary in the y direction)

The Reynolds stresses can be obtained from the Equations (2.15)-(2.17) by taking the means of the products of the series and by taking into account the zero coefficients:

$$\langle \boldsymbol{u^2} \rangle = \langle b_1^2 \rangle y^2 + \cdots, \tag{2.18}$$

$$\langle \boldsymbol{v^2} \rangle = \langle c_2^2 \rangle y^4 + \cdots, \tag{2.19}$$

$$\langle \boldsymbol{w^2} \rangle = \langle b_3^2 \rangle y^2 + \cdots, \tag{2.20}$$

$$\langle \boldsymbol{uv} \rangle = \langle b_1 c_2 \rangle y^3 + \cdots, \tag{2.21}$$

The result is that the normal stresses in the x and z directions increase from zero as y^2, instead the normal stress in the y direction and the shear as y^4 and y^3 respectively. For fully turbulent flow the statistic considered here (normalised by viscous scale) have only a weak dependence on Re number in the inner layer ($y/\delta < 0.1$). The latter assertion will be then discussed with the obtained data from the experiments and compared with the available results in the literature.

2.2 Anisotropic Particles in Turbulence

As said, the occurrence of anisotropic suspended particles in a turbulent flow is quite common in many industrial and natural processes. A better improvement of the design of the industrial equipment and understanding of these natural phenomena require the comprehension of turbulence and its interaction with particles in these complex flows. This interaction is dependent on the Stokes number St defined as the ratio between the characteristic response time of the particle, τ_p and the fluid, τ_f [(Eshghinejadfard, Hosseini, & Thévenin, 2019)].

In addition to the already complex turbulence of multiphase flow, anisotropy introduces with respect to spherical particles another complication: now forces and

torques exchanged with the fluid are dependent on the orientation of the particle [(Voth & Soldati, 2017)]. Nevertheless the experienced torque is due to the fluid strain field that is dominated by small scales which have a degree of universality.

There are different ways for which particles could be anisotropic: they could show anisotropy in their shape, in their rigidity and so on. One of the most common choices of non-spherical particles are the ellipsoidal particles because the fluid torques on them is mathematically tractable and the torques acting on small differently shaped particles are the same as their equivalent. An axisymmetric ellipsoid is also called spheroid and two categories based on the aspect ratio λ (i.e., the ratio of the dimension along the symmetry axis to a perpendicular dimension) can be introduced:

- $\lambda < 1$ corresponds to a prolate spheroid or fiber (in Figure 2.2-1a), useful to mimic the behavior of cylinders and rigid rods,
- $\lambda > 1$ corresponds to an oblate spheroid or disk (in Figure 2.2-1b), useful to mimic the behavior of rigid disks.

Intuitively, $\lambda=1$ indicates a sphere.

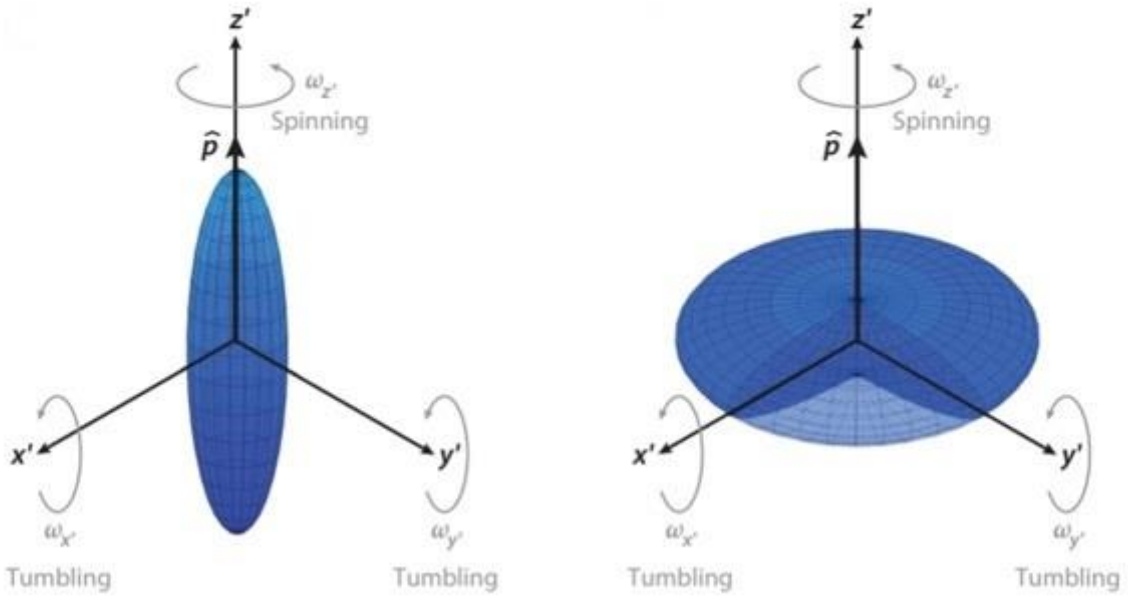

(a) Prolate ellipsoid (b) Oblate ellipsoid.

Figure 2.2-1: Spheroid shapes used to investigate the dynamics of anisotropic particles with **p** being the symmetric axis.

In the figure also a representation of the possible rotations is given, where spinning defines the component of rotation along the symmetry axis and tumbling is instead the components perpendicular to the symmetry axis.

2.2.1 Modeling of anisotropic particles

The parameters on which the choice of the model is based are the particle size, shape and particle to fluid density ratio. Some different models are summarized in Figure 2.2-2.

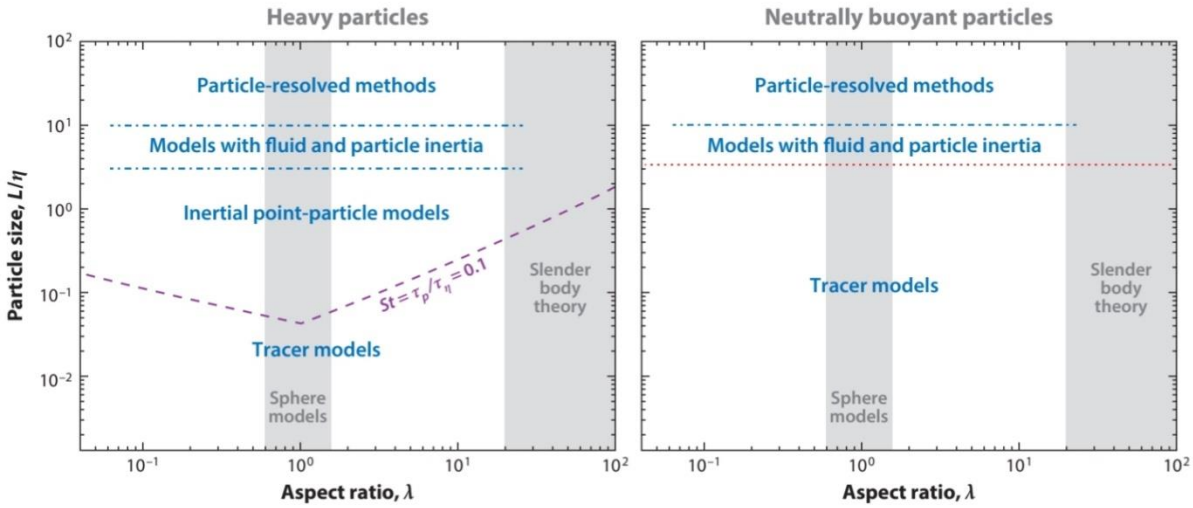

Figure 2.2-2: Conceptual scheme showing different models for anisotropic particles.

From the figure it's clear how the sphere models, which are so widely used, are appropriate for a limited range of aspect ratios. For high aspect ratios instead a class of models derived from slender body theory has been successful [(Khayat & Cox, 1989), (Shin & Koch, 2005)]. For the other aspect ratios instead the models' classification is based on the ratio between the particle size L (largest dimension of the particle) and the Kolmogorov length scale defined in Equation (2.22) and the particle density (defining a difference between heavy and neutrally buoyant particles).

$$\boldsymbol{\eta} = \left(\frac{\nu^3}{\epsilon}\right)^{\frac{1}{4}}, \tag{2.22}$$

In the Equation ν and ε indicate the kinematic viscosity and energy dissipation rate per unit mass respectively.

The models refer to different types of particles:

- Tracer particles: they are small enough to act as perfect flow tracers. Spherical particle rotates at the fluid rotation rate, which is half the local fluid vorticity, instead non-spherical ones translate with the fluid exactly like the spherical ones but their rotation depend on their orientation with respect to the velocity gradient tensor;
- Inertial Point-Particle Models, Stokes Drag: the particle Reynolds number[1], $Re_{p,}$ is small but there is a translation and rotational slip between the particle and the fluid;
- Inertial Point-Particle Models, with Fluid Inertia: particle have all small dimensions with respect to the Kolmogorov scale of the flow, but Re_P is too large to employ the previous model. For this model spherical particle case is instructive, instead analytical approaches are not yet available for non-spherical particles;
- Particle resolved Models: when particles have at least one dimension larger than η then they interact with the non-linear variation of velocity fi

[1] $Re_p = \frac{|u^{(p)} - u^{(f)}|L}{\nu}$ defined using the slip velocity relative to the fluid and the largest particle dimension,L.

3 Methodology

In the current chapter an overview of the techniques used for the realization of this work and consequently on the derivation of the results will be given. Starting from the description of the main features of the particle image velocimetry (PIV), then the speech will develop into an outline of method used for the detection and modeling of the fibers in the channel.

3.1 PIV

As already discussed, PIV was used to carry out the measurements for this thesis. The main reason is related to the main advantages of this technique:

- It is a not intrusive velocity measurement: in contrast with other techniques that use probes as hot wires or pressure tubes, PIV is an optical method. Therefore it is applicable even to high-speed flows with shocks or in laminar boundary layer close to the wall, where the flow may be disturbed by the presence of the probes;
- Instantaneous whole field technique: PIV allows to record images of large parts of the flow field in a variety of media and to extract the velocity information. The resulting vector field has typically 10^3-10^5 grid points and it can be used to compute quantities based on the velocity gradient (as vorticity and rate of strain) [(Caridi, 2018)];
- It is a flexible technique that can be applied across different flow regimes that ranges from laminar to turbulent in liquid and gaseous media and over a wide range of spatial scales;

For all these motives it is therefore clear why particle image velocimetry has become so relevant and powerful especially for the turbulence interpretation in terms of structural elements.

3.1.1 The working principle

In Raffel Particle Image Velocimetry book [(Raffel, et al., 2018)], PIV is defined as a measurement technique that allows capturing velocity fields in fraction of a second and this is done through the evaluation of the displacement of tracing particles between subsequent image frames recorded by an imaging system. An example of a typical PIV setup is given in the Figure 3.1-1. In order to capture the flow's behaviour, small seeding particles are inserted in the flow and transported by the fluid. Indeed, it can be easily assumed that the tracers faithfully follow the motion of the local fluid elements. In liquid flows one of the primary source of error (i.e., the influence of gravitational forces on the velocity of the tracers) is overcame by using neutrally buoyant particles (Raffel, et al., 2018), where this kind of particles are characterized by a density ρ which is identical to the one of the fluid. In addition, if the buoyancy cannot be assured and so a velocity lag is raising the diameter of the particles should be very small in order to ensure good tracking of the fluid motion.

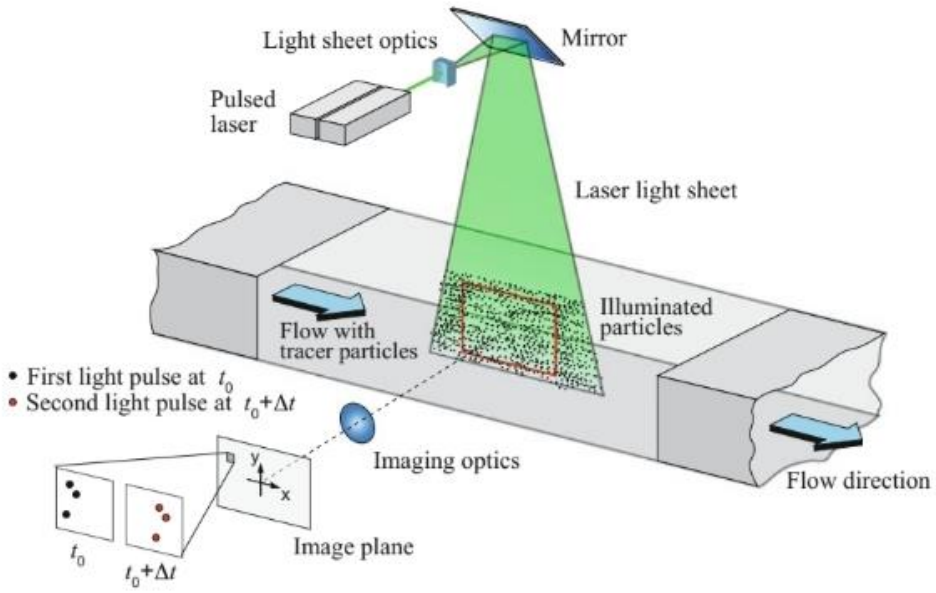

Figure 3.1-1: Set up of 2D PIV in a wind tunnel.

On the other hand the particles' size should be big enough so that the scattered light will also become very small: therefore a compromise must be found (Raffel, et al., 2018).

As visible still from the Figure 3.1-1, the illuminated particles belong to a thin light sheet which is generated by a pulsed light source in two consecutive instants t and t'.

The time delay between these two instants is to be chosen according to the flow velocity and magnification at imaging. The recording system is composed by cameras equipped with CCD or the most recent CMOS sensor. The images are divided into interrogation windows in which the light intensity can be used to detect and localize the particles. To better understand this concept, in Figure 3.1-2 a raw image is shown: the particles and fibers are here appearing as white peaks over a black background, where fibers can be recognized by their elongated shapes.

Finally the velocity of the particles is obtained by dividing their displacement by the time separation between the recordings and the optical magnification factor.

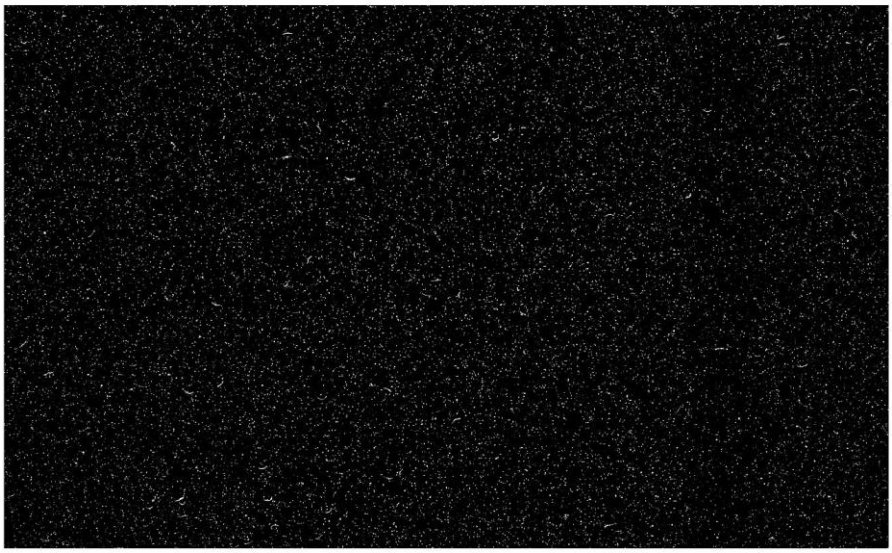

Figure 3.1-2: Single raw image of one of the experiment conducted.

In the following subsections a more in deep discussion on the recording techniques, the illumination devices and the mathematical background of statistical PIV evaluation will be given.

3.1.2 Recording techniques for PIV

The PIV recording modes can be classified into two main categories:

1) methods which takes the pictures of the illuminated particles at multiple times onto a single frame (called *single-frame/double -exposure* or *single-frame/multi -exposure* PIV);

2) methods which takes a single image of the illuminated particle distribution for each time of the illumination (i.e., *double-frame/single-exposure* or *multi-frame/single exposure* PIV).

The dual-frame configuration represents the most used recording arrangement in PIV experiment. Both modes can be observed in the Figure 3.1-3: the interval time between subsequent laser pulses is $\Delta t=t'-t$ and the duration of the light pulses is δ_t (i.e., pulse width). The first parameter is essential for the determination of the displacement of the particles between two subsequent images of a pair and it is chosen accordingly to the flow condition and the magnification of the imaging system: indeed it is selected in such a way that a particle image displacement is determined with sufficient resolution and it must be short enough to avoid too many particles with an out-of-plane velocity component leaving the light sheet between subsequent illuminations. Instead δ_t is chosen short enough to assure the "freezing" of the motion of the particles during the pulse exposure, so that they are pictured as dots (no blurring effects) [42].

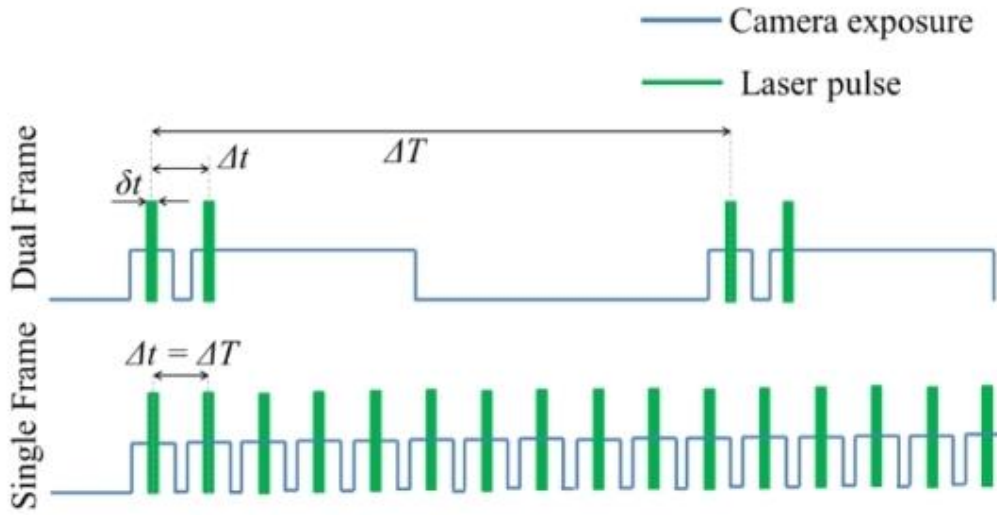

Figure 3.1-3: Timing diagram for laser and cameras in PIV experiments.

The images are captured through digital cameras based in CCD and CMOS sensors. On one hand, CCD cameras used for PIV offer two important advantages: (1) increased spatial resolution, (2) electronic architecture that permits two PIV recordings to be recorded by the same camera (separated by micro- or nanoseconds). Nevertheless, in the last decade, the CMOS sensors have become more frequent for the high-speed recordings due to their improved signal-to-noise ratio and resolution.

3.1.3 Illumination devices

PIV experiments require a source of illumination which can be easily shaped into a thin light sheet for planar measurements. For this reason, lasers are widely used in this technique because of their ability to produce a highly collimated monochromatic light beam that can be easily transmitted through mirrors and shaped into a sheet with arbitrary thickness with lenses. In addition, PIV lasers must emit light within a short pulse and a narrow wavelength range. Most of them operate around the green light (528 and 532 nm) [10]. The type of lasers performed in PIV are to be classified into two groups: (1) argon-ion lasers and (2) semiconductor lasers. The second group is mostly preferred for high-speed measurements because of their higher efficiency (total efficiency around 7% for Nd:YAG and Nd:YLF) resulting in higher average and peak power [36]. The Nd:YAG or Nd:YLF are the most popular among the semiconductor lasers.

Neodym-YAG lasers are the most important solid-state lasers for PIV in which the beam is obtained by Nd^{3+} ions. They assure high amplification and good mechanical and thermal properties. Finally they provide high energy pulses (50 to 500mJ) at a typical rate of 10Hz. Neodym-YLF lasers produce offers good level of energy (10 to 50 mJ) at high-repetition rate up to 10kHz [10].

As said, to obtain a thin light sheet the beam emitted by the laser must be shaped, diverged and focused and this is done through the use of cylindrical and spherical lenses. A graphical representation is given in the Figure 3.1-4.

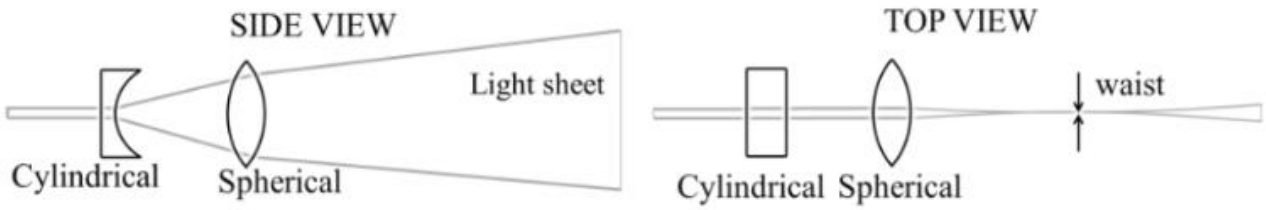

Figure 3.1-4: Cylindrical and spherical lenses shaping a light beam.

3.1.4 Mathematical background of statistical PIV

Before defining the mathematical background for PIV it is for sure useful the introduction of important parameters governing the process of imaging of the seeding particles. A simplified geometrical representation is given in Figure 3.1-5.

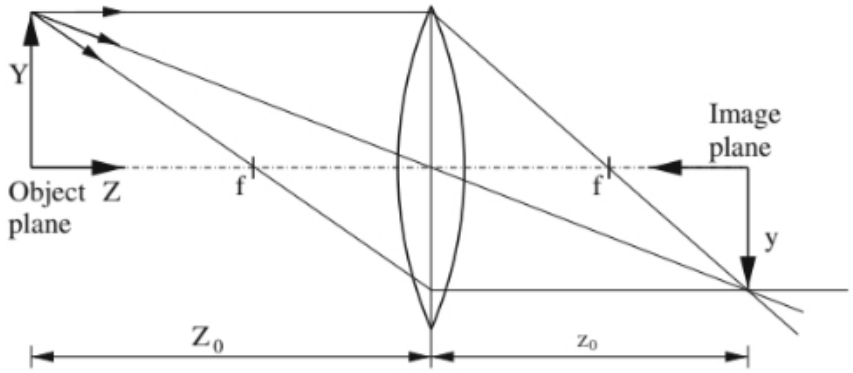

Figure 3.1-5: Optical arrangement of the PIV system

The magnification factor is defined as:

$$\boldsymbol{M} = \frac{z_0}{Z_0}, \tag{3.1}$$

where z_0 is the distance between the image plane and the lend and Z_0, similarly, is the distance between the lens and the objective plane. The focus criterion gives the definition for the focal length f of the objective:

$$\frac{\mathbf{1}}{\boldsymbol{f}} = \frac{1}{z_0} + \frac{1}{Z_0}, \tag{3.2}$$

So the particle image size, d_τ is determined by different contributions: d_p is due to the geometrical projection from the object plane to the image plane, which depends on the magnification factor M defined in Equation (3.1); instead d_{diff} is considering the effect of diffraction due to optical response of the lens.

$$\boldsymbol{d_g} = M d_p\,, \tag{3.3}$$

$$\boldsymbol{d_{diff}} = 2.44 f_{\#}(1+M)\lambda\,, \tag{3.4}$$

$$\boldsymbol{d_\tau} = \sqrt{(Md_p)^2 + d_{diff}^2}, \tag{3.5}$$

Where d_g is the geometrical diameter of the particles, $f_\#$ is the f-number of the lens (defined as the ratio pf the focal length f and the aperture diameter D_a) and λ is the wavelength of the light. Notice that when the size of the particle's geometric image Md_p is smaller than $d_{diff,}$ then the expression in Equation (3.5) is dominated by diffraction effects and reaches a constant value equal to d_{diff}. If instead the particles are larger (or the magnification is larger) the predominance of the geometric imaging becomes considerably larger than d_{diff} and $d_\tau \approx Md_p$. The particle image diameter obtained in Equation 3.5 can be used to estimate the depth of field:

$$\boldsymbol{\delta_z} = 4.88\left(\frac{1+M}{M}\right)^2 f_\#^2 \lambda, \tag{3.6}$$

So finally the mathematical background to retrieve two-dimensional vector fields from a two-frames recording is described. As said, the images are divided into interrogation windows (i.e., IW), which dimension define the spatial resolution of the measurement. In particular, the window size must assure a significant number of particles in it, for PIV this number N should be around 10 [42].

Considering two consecutive time instants t and t' (with the relation t'=t+Δt), the IWs are represented by two dimensional intensity function: $I_t(\mathbf{x})$ and $I_{t'}(\mathbf{x})$, where $\mathbf{x}=(x,y)$. The average particle image displacement $\Delta\mathbf{x}$ can be evaluated by maximizing the statistical operator of cross-correlation R between I_t and $I_{t'}$, defined as follow:

$$\boldsymbol{R(\Delta x)} = \int I_t(\mathbf{x}) I_{t'}(\mathbf{x} + \Delta\mathbf{x})\, d\boldsymbol{x}, \tag{3.7}$$

The process just presented can be visualized in the Figure 3.1-6 and is valid for the case in which there are many particles in the IW, referred to as the high image density limit. It is a desirable condition because it guarantees that at every interrogation spot on the image plane there is a high probability of obtaining a velocity vector that represent the average motion of the particles in that spot (Adrian, 1997).

To assure the quality of the cross-correlation, and consequently of the average displacement, it is possible to estimate the signal-to-noise ratio (SNR) by computing the ratio between the highest peak and the second tallest one. The measurement is valid if SNR is in a range between 1.2 and 1.5.

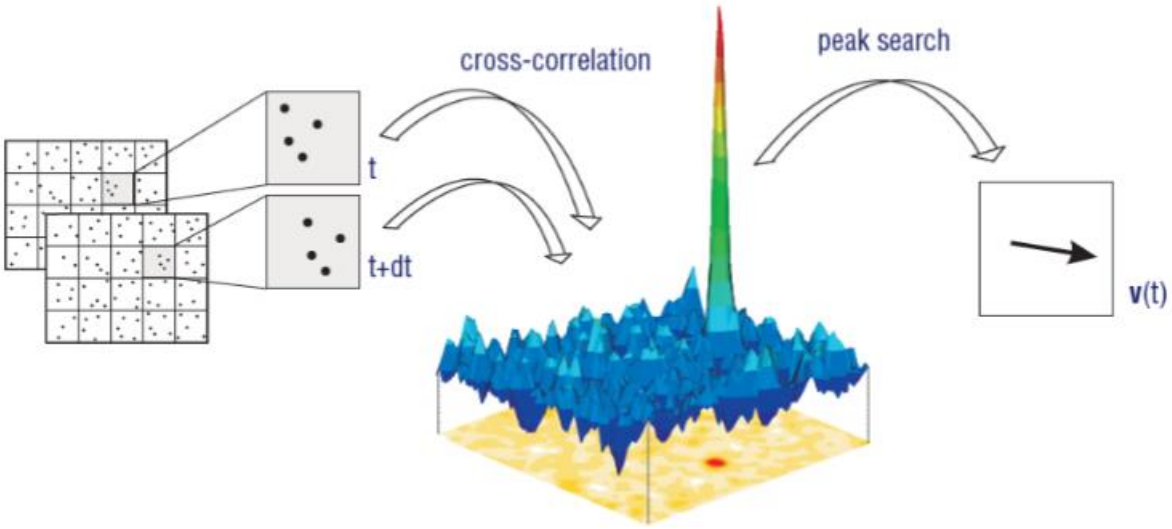

Figure 3.1-6: Cross-correlation technique used in PIV.

3.1.5 Spatial resolution and dynamic ranges

The result from previous subsection is a finite number of vectors inside the field of view where the distance between adjacent independent vectors defines the spatial resolution of the PIV measurement. The spatial resolution of PIV quantifies the ability to resolve small-scale velocity fluctuations embedded in larger scale motion, as occurs in various fluid mechanical phenomena as boundary layers and turbulence. Range of scales that can be resolved given the size of the interrogation window could be quantified using the dynamic spatial range which is defined by the following ratio:

$$\boldsymbol{DSR} = \frac{I_x}{D_I} = \frac{L_x/M}{D_I}, \tag{3.8}$$

Where D_I is the dimension of the IW (i.e., the minimum resolvable scale) and I_x is the length of the field of view and L_x is the sensor size in pixel. Simply DSR can be seen as the number of independent (i.e., not overlapping) velocity vectors along the linear dimension of the field-of-view [4].

Similarly a dynamic velocity range can be introduced. It is given by the largest and smallest detectable displacement:

$$\boldsymbol{DVR} = \frac{\Delta x_{max}}{\sigma_{\Delta x}}, \tag{3.9}$$

Notice that x in the subscription at the denominator denotes the position in the fluid and X denotes the position in the image plane. With careful design, values for the DVR may range in the order of 100 or higher.

Although it can be derived that:

$$(\boldsymbol{DSR})(\boldsymbol{DVR}) = \frac{L_x}{c_\tau d_\tau}, \tag{3.10}$$

So to maximize both parameters it is necessary to maximize dimensionless constant on the right-hand side of the Equation (3.10) which represent a characteristic of the system: L_x is a measure of the capability to hold information (since it is the physical size of the recording system), d_τ is a measure of the performance of the optical imaging and recording systems and finally c_τ is a measure of the ability of the interrogation algorithm to measure displacement accurately, typically 1-10% of the image diameter [4].

3.1.6 Error sources of PIV

It has become clear from the past subsections that the overall measurement error in PIV is given by a variety of aspects coming from the set-up and recording process to the mathematical evaluations of the velocity field. Different source of errors must be therefore considered and solved:

- errors related to alignment and installation;
- errors caused by the system components;
- error due to flow itself;
- errors introduced by the evaluation techniques.

Among this errors causing uncertainty in PIV measurements the ones that are mostly interesting for the aim of this thesis are the last two, since the first two types include optical distortions, misalignments of the laser sheet, other type of image noise and systematic errors like timing and synchronization offsets involving the hardware components that cannot be extracted and quantified by analysing the recorded images.

Therefore it is even more important to take care of those checking and optimizing the experimental setup and conditions beforehand.

In particular the third type will be discussed more in detail in Chapter 6 where the turbulence statistics are evaluated and analysed. Indeed the third type of error depicted above is caused by the large flow gradients and/or strong velocity fluctuations that take place in turbulent flows. Furthermore Reynolds or temperature, viscosity or density of the fluid changes during the experiment runtime may cause measurements errors. The first step related to the last source of uncertainty in the bullet list is surely related to the interrogation window's size choice. As already anticipated in the last subsections, IW's size should assure an adequate effective number of particles that can be estimated knowing the number of particles N_I within the window, the in-plane loss of pairs F_I and the out-of-plane loss of pairs F_o (valid for 3D PIV):

$$\boldsymbol{N} = N_I \cdot F_I \cdot F_O, \tag{3.11}$$

N should be greater than 5 on average to limit the amount of spurious measurements to a few percent. If this value is not reached, then the spurious vector will contribute to the measurements of the velocity field and may influence the interpretation of the results if not properly filtered out.

Lower outlier probability can be achieved by reducing the time interval between the illumination (i.e., Δt), increasing the size of the interrogation windows or raising the seeding concentration. On the other hand these strategies could also raise measurement uncertainty, for instance decreasing Δt leads to a reduction of the DRV (defined in Equation (3.9)) resulting in a larger relative measurement uncertainty.

3.2 Fiber detection and modeling

The process of recognizing and modeling the fibers in order to extract information on dry and wet conditions was conducted through in-house built MATLAB codes. In the next subsections deep explanations will be given on these two processes.

3.2.1 Detection process

The main difficulty and main target of the code for the case of the fiber laden flow was to distinguish the fibers from the tracers and other possible spurious objects. As a first step the images recorded during the experiments were pre-processed using the commercial software Lavision GmbH: Davis 10.2. The pre-processing consisted in a minimum intensity subtraction applied to all the images in order to remove outlier

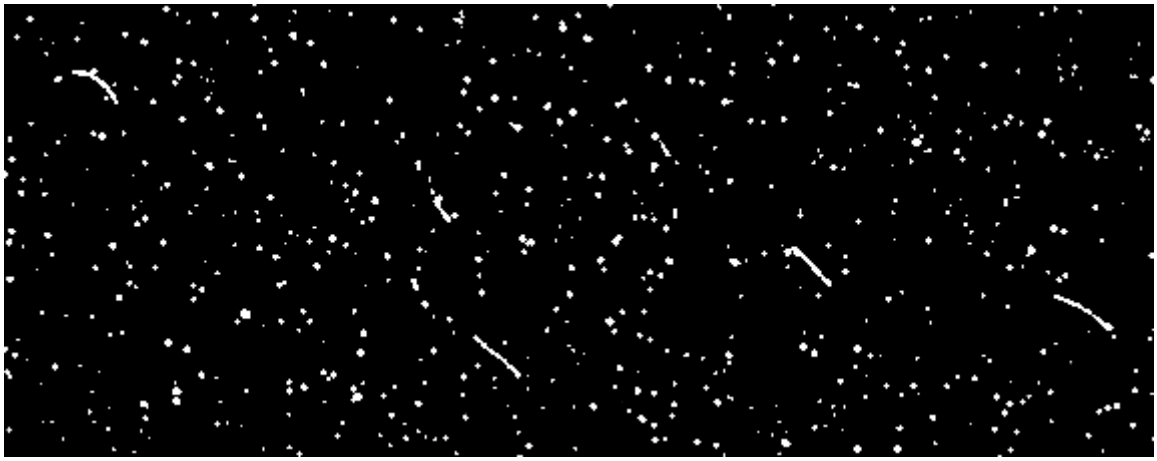

Figure 3.2-1: Group of fibers in a zoomed high contrast raw image.

noise. In such a way background noise was reduced. In addition, to avoid the problem of reflection of the glass near the wall region the images where cutted at an adequate height so that the relevant information near the wall were not eliminated. Finally these images were flipped left to right to assure positive values of velocity components (due to the set-up of the experiment described in Chapter 4). So initially the images were as the one shown in Figure 3.1-2, in addition here in Figure 3.2-1 a zoomed region in which fibers are clearly recognizable is displayed (notice that the contrast was artificially increased to show the reader the difference in shape and dimensions).

From the figure it appears clear how the fibers are well recognizable from their elongated shape and an additional information (not available from the picture above) is that being them larger in size with respect to the tracers leads to scatter more light, implying that the intensities reached by the fibers are higher. An example of discrimination process on a frame is shown in Figure 3.2-2. The code was built based on the concepts depicted above: therefore intensity (Figure 3.2-2b) and area (Figure 3.2-2c) thresholds were applied to the raw images which values were decided arbitrary by the observation of the available raw images coming from the experiments.

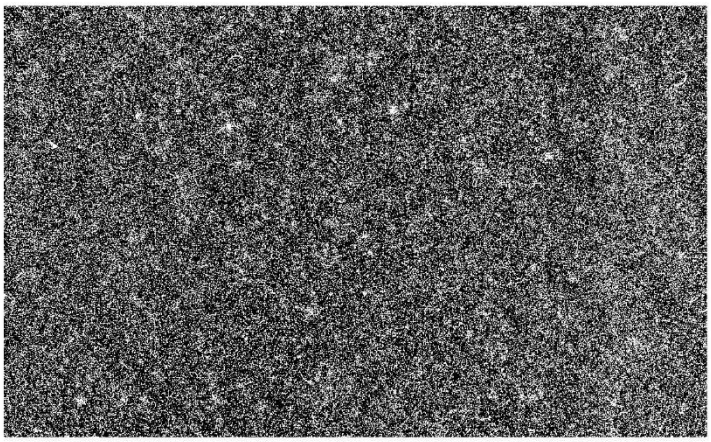

(a) Raw image.

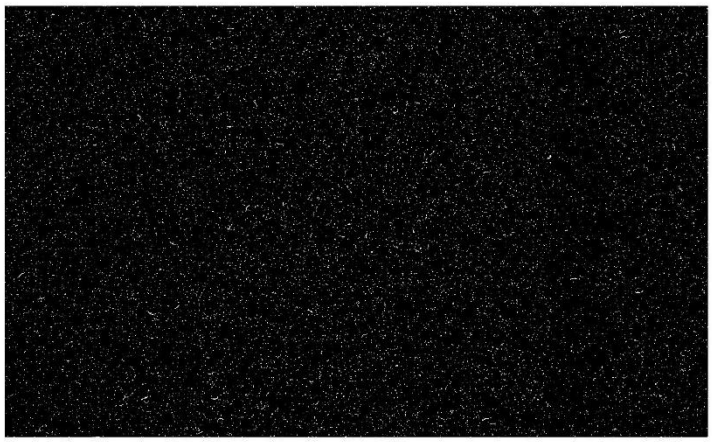

(b) Raw image after application of intensity threshold.

(c) Raw image after application of intensity and area thresholds

Figure 3.2-2: Steps of the process of fibers discrimination.

3.2.2 Modeling process

In order to model the fibers and be able to derive the curvature and length and detect their movement for a future tracking in the channel, after the discrimination each fiber has to be associated with the representing coordinates in the two-dimensional space. What was stated as an initial hypothesis is that the non-axisymmetric fibers are bent, but not twisted. Using the built-in command *regionprops* on MATLAB, it was possible to obtain for each particle image identified as a fiber a set of information as area, centroid, major and minor axes length and orientation.

In addition to the initial hypothesis, from observations of the fibers in dry conditions and from common model's choice used in the literature [(Alipour M. , 2021)] it was possible to conclude that the function that best fits in a least-square sense the single fiber is a 2nd order polynomial. According to the last property of the above-mentioned command that indicates the orientation (i.e., the angle between the x-axis and the major axis of the ellipse that has the same second-moments as the region, returned as a scalar) three methods were proposed for the definition of the coordinates of the polynomial. The results for two fibers differently oriented are given in Figure 3.2-3a-b. In particular in Figure 3.2-3a a 45° oriented fiber is displayed: on the left the raw image of the fiber and on the right the three curves coming from the three methods approximating the fiber's shape. In Figure 3.2-3b the fiber is 90° oriented.

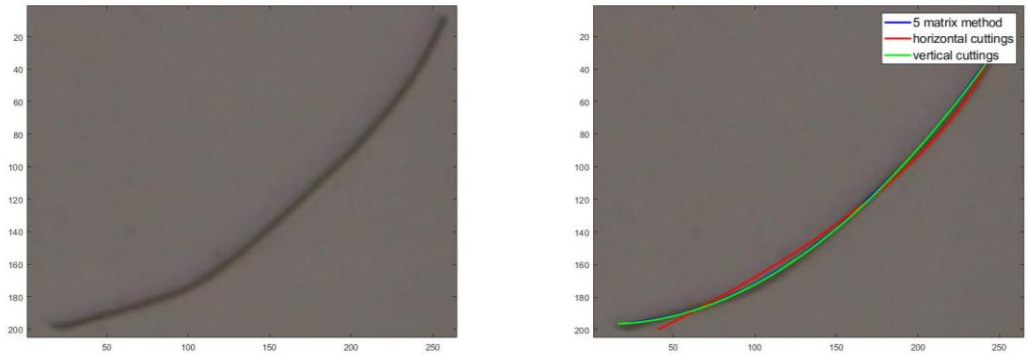

(a) Case of a 45° oriented fiber.

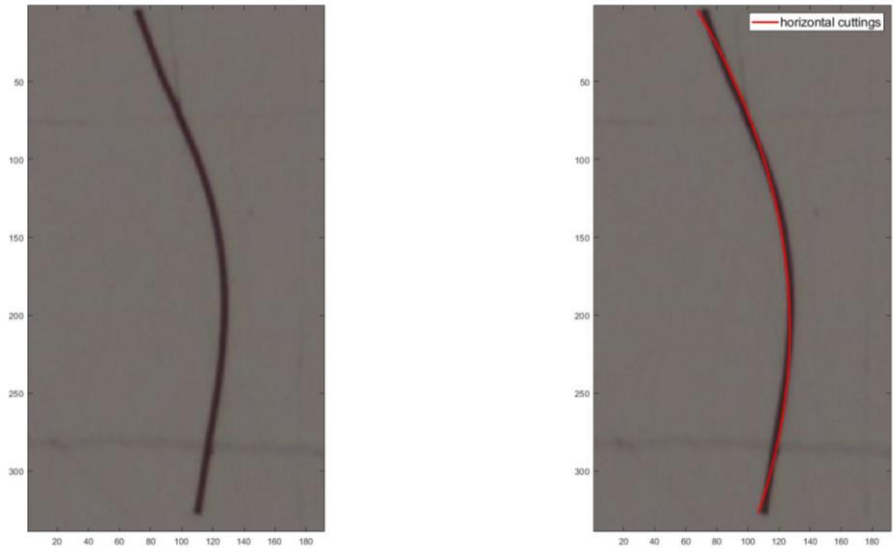

(b) Case of a 90° oriented fiber.

Figure 3.2-3: The three methods for approximating the 2nd order polynomial.

Before applying the methods for the approximation of the best fitting polynomial, the application of a 2D Gaussian smoothing filter with a suitable kernel was necessary to allow a more accurate research of the adequate set of points for the approximation.

When the orientation of the fiber is lower than 45° (targeted as a horizontal fiber) than the model searches for the intensity peaks along the first dimension (i.e., along the columns, so vertical direction) which are expected to be at the centres of the fiber. On the contrary, for fibers with orientation major than 45° intensity peaks are searched on the second dimension (i.e., along the rows). As visible in Figure 3.2-3a also a third way was investigated, in which the maximum intensity was searched in a "moving" 5x5 matrix. Nevertheless, this strategy was then overcome since it gave the same results as the simpler model of vertical cuts (i.e., model for orientation lower than 45°), that was then preferred for its simplicity in the computation.

4 Experimental setup

In the current chapter the experimental facility, tracers and fibers properties and image acquisition systems are described. Focus is given to an exact presentation of the optic parameters for the image acquisitions and the input parameters for the PIV performed for the realization of this work.

4.1 Geometrical properties of fibers: imaging set up

The fibers employed for this experiment in the water channel were Polyamide 6.6 (PA6.6) Precision Cut Flock (Flockan). The technical details are summarized in Table 4.1.

Fib name	**colour**	**length (L_f)**	**diameter (d_f)**	**aspect ratio (λ)**	**linear density (ρ_l)**
[-]	**[-]**	**[mm]**	**[mm]**	**[-]**	**[decitex]**
5793C	Red	1.2	0.010	120	0.9

Table 4.1: Technical details of fibres.

The density and cutting length are $\rho=1.15x10^3$ kg m^{-3} and L_f. The diameter $d_f = (4\rho_l / \rho\pi)^(1/2)$ is around 10 μm. In Figure 4.1-1a a microscopic view of the fibers considered in this study is given [image taken from (https://www.schuster-beflockung.de/beflockungstechnik-blog/woher-kommt-der-name-flock-where-does-the-name-flock, s.d.)]. In particular the observation of the shape of the fibres in Figure 4.1-1b was necessary at this point since from it we could have been able to assume the initial hypothesis stated at the beginning of the model process already depicted in Chapter 3.2.2

(a) Microscopic view of a cluster of fibers.

(b) Close-up view of dry fibers.

Figure 4.1-1: Fibre samples.

The dry fibers were squeezed between two polished plexiglass glasses and gently separated through a wooden stick in order for them to not overlap. The plexiglass glasses were then closed together through 4 screws and then clamped to a slider that allowed an easy and flexible set-up. The images were collected with a Canon EOS 77D (CMOS Camera with sensor size 22.3 x 14.9 mm [(Canon EOS 77D- caratteristiche, n.d.)]).Camera lenses (Tokina AT-x pro Macro 100mm) [(https://tokinalens.com/product/at_x_m100_pro_d/, s.d.)] were also employed for all the acquisitions. The optic parameters for this set up are given in the Table 4.2.

f# number	ISO	Exposure	Environmental lights	M
32	100	1/100s	ON	0.7

Table 4.2: Optic parameters of the dry fiber imaging set up.

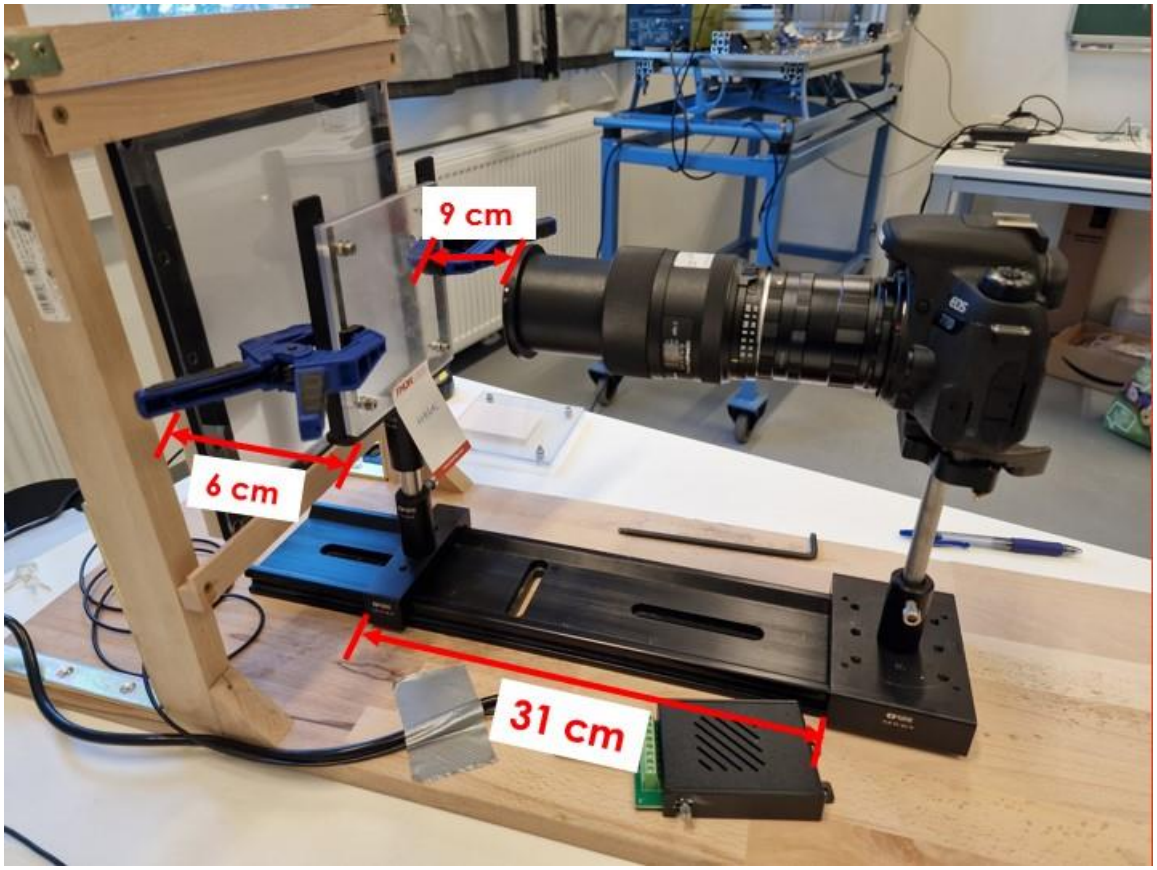

Figure 4.1-2: Picture of the dry fibers imaging set-up.

A picture of the dry fibers imaging set-up is given in Figure 4.1-2. The illumination device employed for this set up was a LED plate that was located behind the fibers in order to improve the brightness and improve the resolution of the images.

4.2 Experiments' set-ups in the channel

4.2.1 Flow apparatus and equipment

The experimental facility for both the unladen and laden flow experiments is the TU Wien Turbulent Water Channel, consisting of a 10m long water channel, constructed by combining five sections of 2 metres each, with cross-sectional dimensions of 80 cm x 8 cm (w x 2δ, where δ indicates the half-channel height). Each of the five sections is equipped with de-airing valves, which allows the removal of the bubbles trapped close to the top wall of the channel. In particular, the channel is manufactured using polymethyl methacrylate with a thickness of 1.5 cm, which is fully transparent. The channel is sketched in Figure 4.2-1 [(Alipour, De Paoli, Ghaemi, & Soldati, 2021)].The

upper cover of the channel is removable in all sections and in both open and closed channel configurations experiments can be performed. For the aim of this thesis only the closed configuration must be considered with no free surface. The flow is circulated from the downstream to the upstream reservoir by a pump and the flow is subsequently driven by gravity. A centrifugal volute pump (maximum flow rate of 147 $m^3 h^{-1}$) and a Proline Promag 10D electromagnetic flowmeter are used. To eliminate all vibrations, possibly created by either the pump or the laser's chiller, both equipment are placed on vibration isolators.

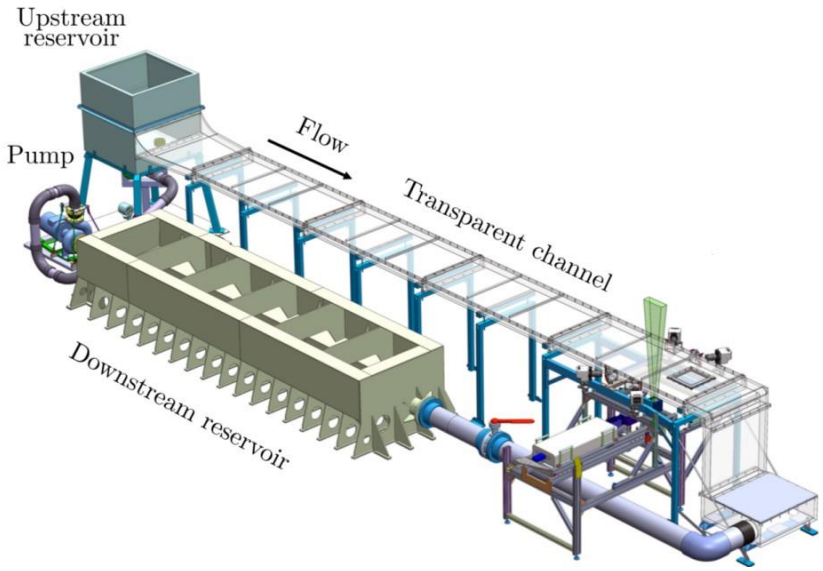

Figure 4.2-1: Schematic of the TU Wien Turbulent Water Channel.

The measurements were conducted in correspondence of the test section, located 8.5 m downstream of the channel entrance (see Figure 4.2-2b), to ensure the fully developed flow condition. The measurement volume is located mid-span of the channel (as visible in Figure 4.2-1). The illumination device consists in a thick laser sheet (532 nm, double head, 6 mJ per pulse at 10kHz, with a maximum power of 120 W, Litron LD60-532 PIV [(Lasers for PIV, 2022)]. A picture of the head of the laser is given in Figure 4.2-2c. The images were recorded using one high speed camera (Phantom VEO 340 L with CMOS sensor) with sensor size of 2560 x 1600 pixels at 0.8 kHz and each pixel size is 10x10 μm^2 [(VEO-E 340L, 2012)]. In order to avoid any possible vibration coming from the channel frame, the camera holder is equipped with a damper. The camera was placed so to have the objective lens with an angle of 90° with respect to the lateral walls of the channel and parallel to the spanwise direction (a close up is shown in Figure 4.2-2.a).The objective lens has a focal length f=100 mm.

(a) Close up on the camera set up.

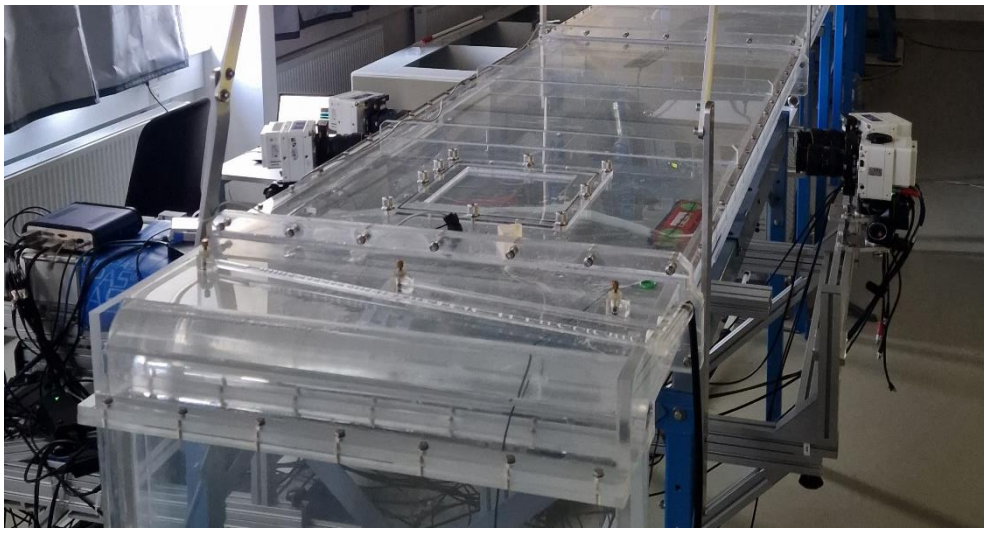

(b) Camera set-up.

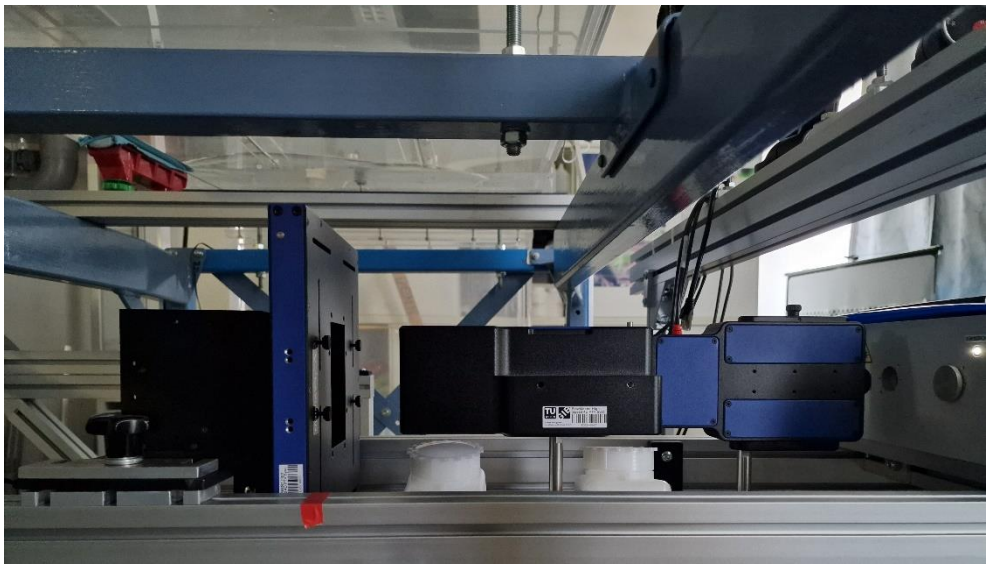

(c) Laser head.

Figure 4.2-2: Picture of the channel flow experimental set-up.

As a first step for all the experiments calibration was necessary: therefore a three-dimensional calibration target (a picture of the calibration plate is displayed in Figure 4.2-3) with size of 58x58 mm [(3D Calibration)] was used in order to compute the scale factor necessary for the conversion of pixel into metric scale of the derived quantities of the PIV. In addition, calibration is also necessary to check for the possibility of misalignment of the lens.

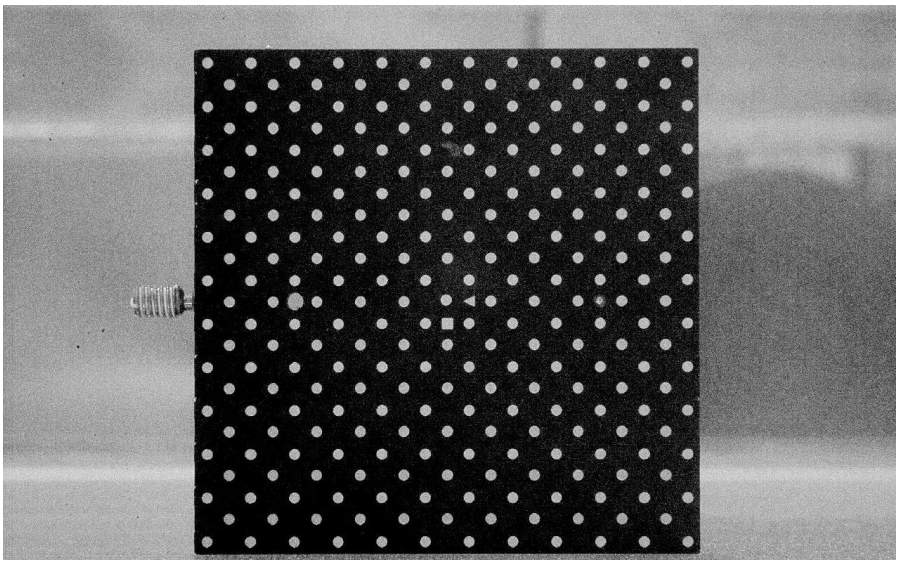

Figure 4.2-3: 3D Calibration target from LaVision.

In addition, temperature was checked before, during and after the experiments through a temperature sensor situated downstream of the channel. Data acquisition has been performed using single frame method with different frequencies of acquisition differentiating between unladen and fibers laden flows and changing according to the friction Reynolds number Re_τ. Prior the application of the PIV, the images were pre-processed by subtracting the minimum intensity value of the dataset from each image to reduce background noise using the software DaVis.

Particle image velocimetry was then employed for the unladen flow case using MATLAB additional tool 'PIVlab': the chosen algorithm was FFT window deformation since in most applications it delivers the best results. By selecting this algorithm, the data are analysed in several passes: The first pass uses relatively large interrogation areas to calculate the displacement with major reliability. The larger the interrogation areas, the better the signal-to-noise ratio, and the more robust is the cross correlation. On the other hand bigger sized interrogation areas also only give a very low vector resolution ("vectors per frame"). That is why the size of the IW is decreased in the following passes. The displacement information of the first pass is used to offset the interrogation areas in the second pass and so on. This procedure yields a high vector

resolution, a high signal-to-noise ratio, and a high dynamic velocity range. The interrogation areas of later passes are not only displaced, but they are also deformed ((Thielicke, 2021)).

In the next subsections the data on the acquisition system and parameters in input of the planar particle image velocimetry will be given.

4.3 Unladen Flow

As already depicted in Chapter 3, the way in which PIV compute the instantaneous velocity field is through an undirect measurement: obtaining the velocity of the fluid via the tracer particles velocity. Therefore, the interaction of the particles and the surrounding fluid must be examined in order to avoid significant discrepancies between the fluid and particle motion [(Raffel, et al., 2018)].

For the unladen flow case the channel was therefore seeded with neutrally buoyant tracers with a diameter of 20 μm. In the following table the quantities measured during the experiment and the camera recording parameters are summarized.

Re_τ	Initial T	Final T	Initial Q	Final Q	Digital resolution	Acquisition Frequency	f#	M
[-]	[°C]	[°C]	[l/min]	[l/min]	[mm/px]	[KHz]	[-]	[-]
187	24.04	24.25	254.49	259.61	0.0407	1	8	0.25
368	23.68	23.99	561.62	559.70	0.0407	1	8	0.25
726	23.28	23.97	1222.03	1215.34	0.0407	1	8	0.25

Table 4.3: Camera recording parameters adopted and relevant measured quantities during the experiment.

Where Q and f# stands respectively for flow rate and f-number: the latter in particular refers to the ratio of a lens's focal length to its aperture's diameter and indicates the amount of light coming through the lens [(n.d.)] . The Reynolds numbers specified in Table 4.3 are the averages in time during the experiments. Flowrate was maintained constant through the exeriments, nevertheless flucutations may occur due to: noises coming from the flow rate sensor and fluctuations introduec by turbulence itself. Only a slight increase was observed in the flow rate profile in the case of Re_τ=720, and this was due to a major increase of the temperature compared with intermediate and lower cases.

The initial images had a size of 1600 x 2560 pixels, then they were cutted and reduced to 1563x512 pixels. This choice was necessary to eliminate the noise due to the reflection of the glass (the images were cutted exactly at the wall) and redundant information on the x direction. Consequently with the reduction of the size of the image, the computational effort is very much lowered for the determination of the velocity field through PIV.

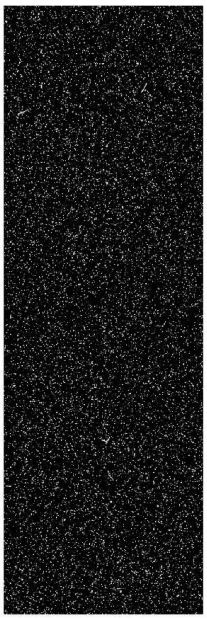

Figure 4.3-1: Cutted raw image (Case Reτ=180 is depicted here).

Image sequencing style	**Time resolutions**	**IW size**
[-]	**[ms]**	**[pixels]**
Pairwise	4	8x8
Pairwise	4	16x16
Pairwise	4	24x24
Pairwise	4	32x32
Pairwise	6	8x8

Pairwise	6	16x16
Pairwise	6	24x24
Pairwise	6	32x32
Pairwise	8	8x8
Pairwise	8	16x16
Pairwise	8	24x24
Pairwise	8	32x32

(a) For Re_τ=187.

Image sequencing style	**Time resolutions**	**IW size**
[-]	**[ms]**	**[pixels]**
Pairwise	2	8x8
Pairwise	2	16x16
Pairwise	2	24x24
Pairwise	2	32x32
Pairwise	3	8x8
Pairwise	3	16x16
Pairwise	3	24x24
Pairwise	3	32x32
Pairwise	4	8x8
Pairwise	4	16x16
Pairwise	4	24x24
Pairwise	4	32x32

(b) For Re_τ=368.

Image sequencing style	Time resolutions	IW size
[-]	[ms]	[pixels]
Pairwise	1	8x8
Pairwise	1	16x16
Pairwise	1	24x24
Pairwise	1	32x32

c) For Re_τ=726.

Table 4.4: PIV setting parameters.

After the experiments PIV measurements were conducted using PIVlab from MATLAB. The window sizes and time resolutions chosen are given in the Table 4.4a-c for the three cases for friction Reynolds number.

Where imaging sequencing style determines the way in which correlation between frames must be evaluated: for all the images, the correlation function (depicted in Chapter 3.1.4) is calculated between consecutive frames (i.e., first frame with the second, third with the fourth and so on). Different time resolutions were obtained through image shifting technique that consists in skipping an arbitrary number of frames with the aim of obtaining larger particles' displacements and reduce the uncertainty of PIV measurements. Finally the investigation window choice is rather important since a larger size choice leads to a larger spatial resolution and major probability of detecting the same particle in subsequent frames, on the other hand application of bigger sized IW leads to loss of information near the wall. These concept will be discussed in the next subsection.

The instantaneous velocity fields will be then analysed and used to study turbulence statistics in Chapter 6.

4.4 Uncertainty in PIV measurements

Compared to the most common techniques for the study of turbulence in channel flow (i.e., hot wire anemometry and Laser doppler velocimetry), PIV is known to suffer from higher measurement uncertainties [(Wilson & Smith, 2013) (Timmins & Wilson, 2012)].

Nevertheless to guarantee accurate turbulence measurements we need a measurement system with an uncertainty which is adequately below the velocity fluctuations of interest. In addition, the measurement area in which each velocity vector is estimated must be small compared to the smallest size of turbulent structure. Moreover, the number of samples N must be sufficiently large to ensure that the average velocity is fully converged [(Scharnowski & Kähler, 2019)].

Re_τ	T	η	τ_η
[-]	**[°C]**	**[μm]**	**[ms]**
187	24.15	792.6	690.3
368	23.8	480	251.1
726	24	272.7	81.5

Table 4.5: Kolmogorov scales for unladen flow experiments.

[pixels]	8	16	24	32
[μm]	325.6	651.2	976.8	1302.5

Table 4.6: Window's dimensions in metric scale.

In Table 4.5 the values for the Kolmogorov length and time scales for the unladen flow experiments are given through the Equations. For a better readability and comparison, in Table 4.6 the dimensions in pixels of the interrogation windows employed in the PIV measurements are given in μm using a scaling factor equal to 0.0407 mm/pixel (obtained from the calibration). From the comparison between tables it is quite clear that the dimensions of the squared IWs are lower than the smallest of the turbulence structure sizes, except for one case: 8x8 window applied on the experiment with Re_τ=726.

To assure an adequate number of samples and reliable results it was decided to record 4816, 5036 and 6000 images for Re_τ=187, 368 and 726 respectively. The adequacy of the

samples will be then discussed in chapter 6 with the comparison between the turbulence statistics and the data from literature.

4.4.1 Effect of dt and window size

As said in previous subchapters, the measurements were conducted using nine different dt between 4 ms and 8 ms and 2 ms and 6 ms (performing image shifting) for Re_τ=187 and 368.5 respectively, corresponding to a maximum particle image displacement between 8 and 16 pixels in the middle of the channel. The results for the variation of the particle image shift (i.e., changing dt) and different interrogation window size are illustrated in Figure 4.4-1 taking as an example the rms of the normal fluctuation of velocity component v' for Re_τ=187. It was chosen to show the most interesting the region in which the contour of the velocity field is going from almost zero at the wall to non-zero values far from the wall.

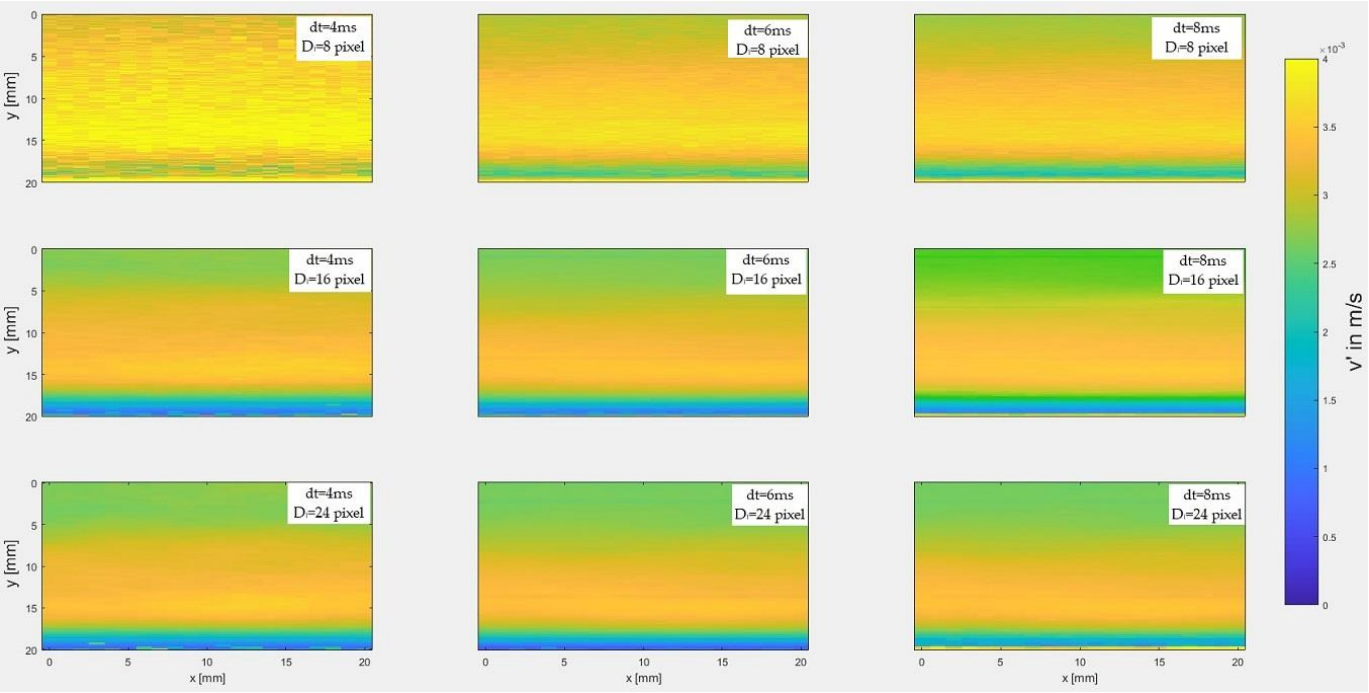

Figure 4.4-1: Contours of v' for Re_τ=187 at different dt and D_I.

The worst result is the one depicted in the top left of figure and obtained with both lowest window size and dt (i.e., lower displacement of the image particle): the noise is much more amplified then in the other 8 configurations. For increasing particle displacement (i.e., increasing dt going from left to right configurations in the Figure 4.4-1) as for increasing window size D_I the velocity field is much smoother and

therefore much better suited for turbulence estimations. Due to the enlargement of D_I, the absolute uncertainty of the particle image displacement $\sigma_{\Delta x}$ decreases and so does the uncertainty of the estimated velocity. Or it could be due to a decreased relative shift vector uncertainty due to enlarged mean displacement $\langle \Delta x \rangle$. On the other hand, as also said in past chapters, increasing dt or the IW's size could lead to too smoothed results which might filter out small-scale turbulence structures [(Scharnowski & Kähler, 2019)].

4.4.2 Peak locking

One important systematic error source that must be considered for PIV is peak locking. According to Raffel [36], the continuous intensity distribution of very small particle images is insufficiently sampled by the discrete digital camera sensor. Thus the estimated displacements are shifted toward the closest integer pixel positions and, as a results, the velocity coming from PIV measurements is over- or underestimated depending on the sub-pixel length of the shift vector in the image plane [(Christensen, 2004)].To examine the presence of peak-locking it is possible to inspect the probability density function of the displacement (in pixels) of the particle. This was done for all the time and spatial resolutions, but here for the sake of briefness only one window size (i.e., 16 pixels) for each Reynolds number is shown. Moreover, for an easy comparison, in Figure 4.4-2 it was decided to show (image taken from Christensen reference [11]) the case in which peak locking highly affects the measurement in a fully developed channel flow. From Figure 4.4-3 and Figure 6.4-2(a-(c it is clear that peak-locking is not affecting much or none the images since the PDF seems well distributed for all the values, also in between the integers (the bin sizes for the determination of the probability density function was 0.1 pixel).

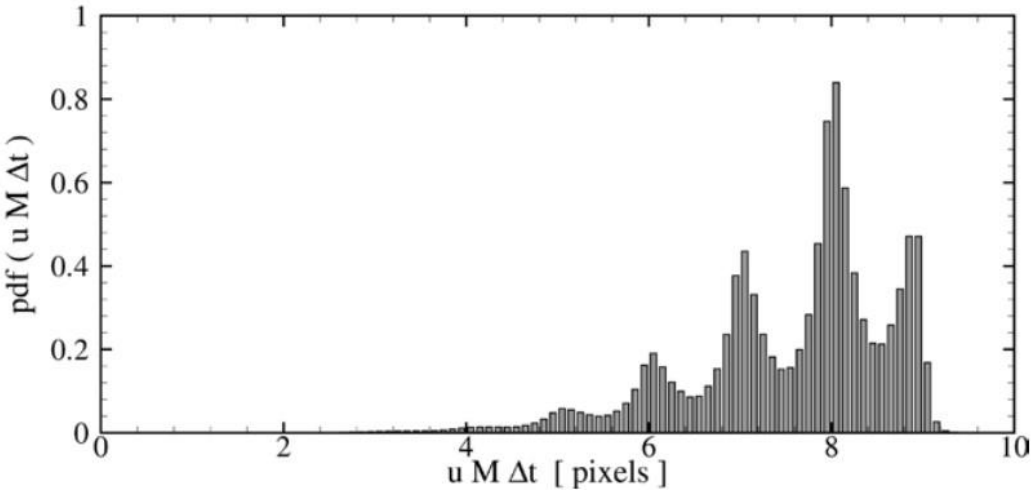

Figure 4.4-2: PDF of particle-image displacement illustrating pixel locking effects.

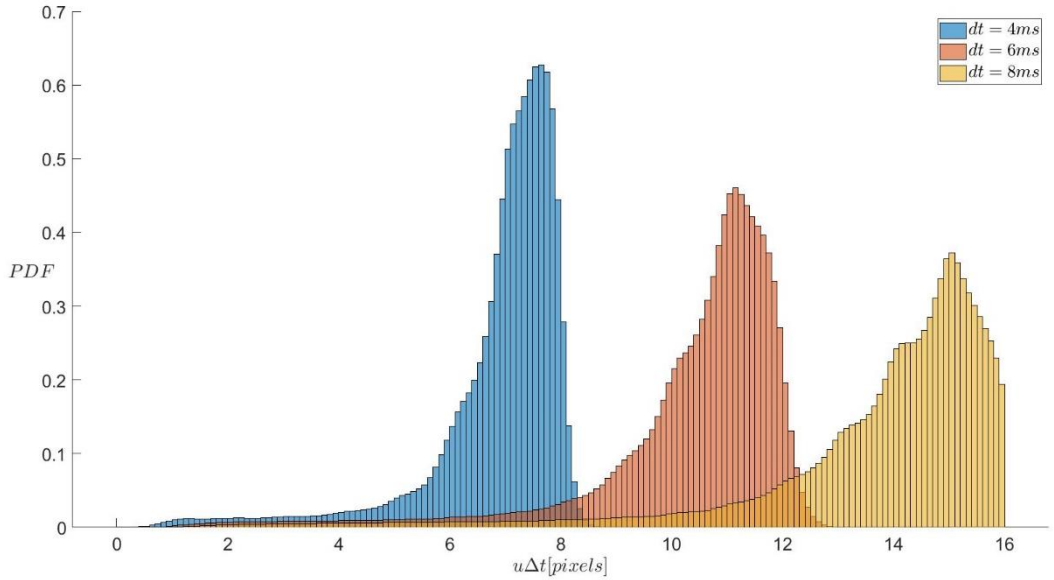

(a) For Re_τ=187.

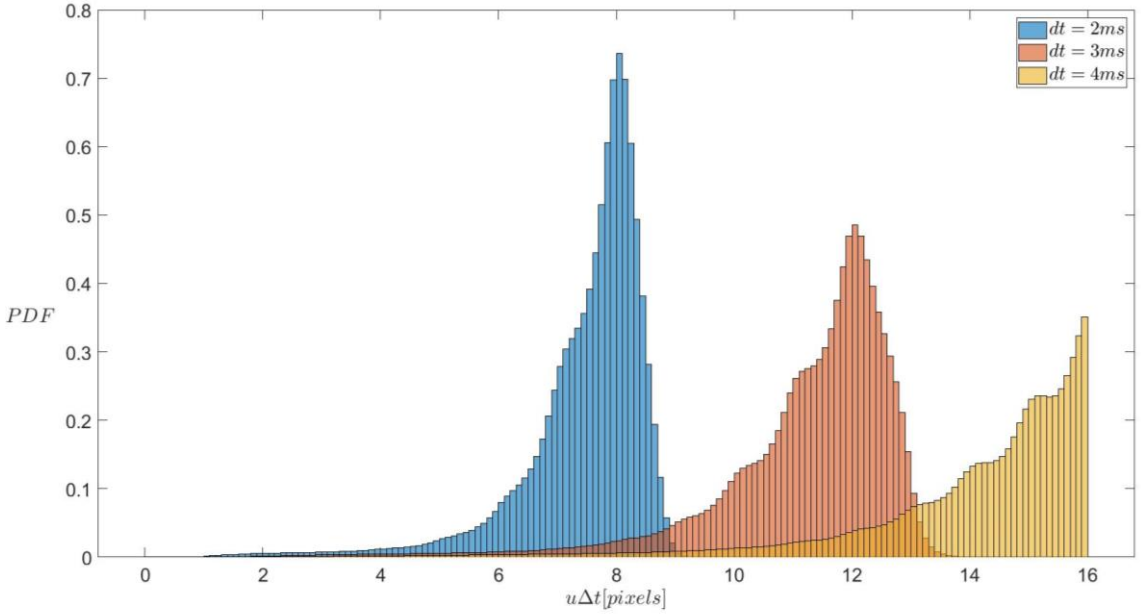

(b) For Re_τ=368.

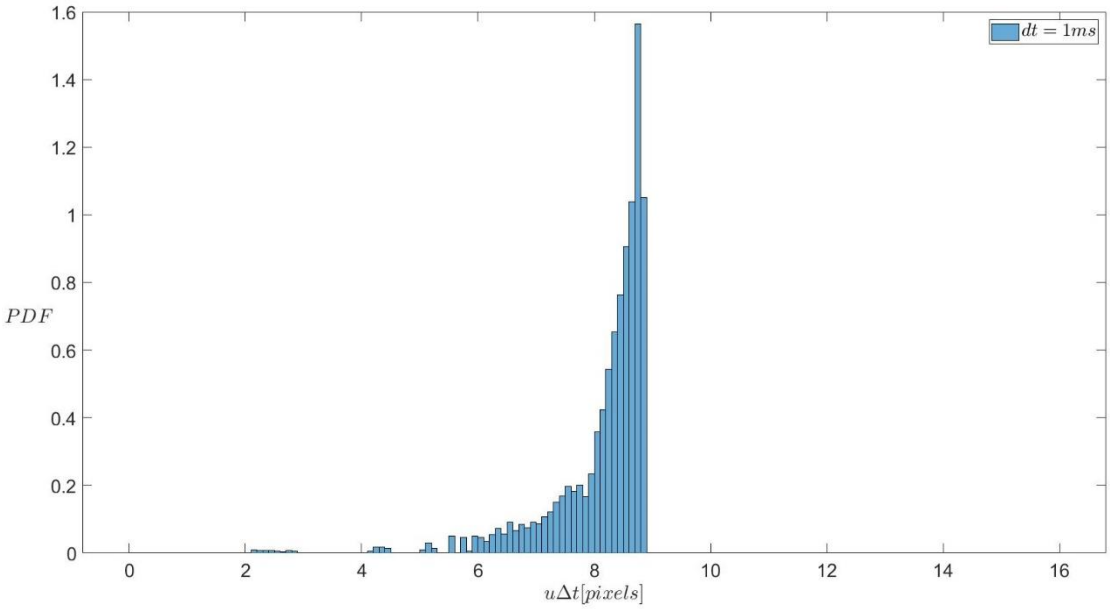

(c) For Re_τ=726.

Figure 4.4-3: Probability density function of particle displacement.

4.5 Fiber laden flow

Similarly to what was done for unladen flow was performed for fiber laden experiments. In this case not only tracers were seeded in the flow, but also the fibers which properties are given in the previous subsection 4.1. Again the quantities measured during the experiment and the camera recording parameters are summarized in Table 4.7.

Re_τ	**Initial T**	**Final T**	**Digital resolution**	**Acquisition Frequency**	**f#**	**M**
[-]	**[°C]**	**[°C]**	**[mm/px]**	**[KHz]**	**[-]**	**[-]**
200	22.95	22.70	0.0404	0.4	16	0.25

340	23.15	23.07	0.0404	0.8	16	0.25
650	23.39	23.28	0.0404	1.3	16	0.25

Table 4.7: Camera recording parameters adopted and relevant measured quantities during the experiment.

4.5.1 Reconstruction process

Among all the experiments, it was decided to perform the reconstruction of the fibers only for the case of Re_τ=200. The friction velocity of the unladen flow is u_τ=4.7 mm/s, calculated using the kinematic viscosity ν of water at 22.7°, the average temperature of the experiment. Viscous time and viscous length of the flow are τ≈42.5 ms and δ_ν≈200μm respectively. Kolmogorov time and length scales of the flow at the centre of the channel are τ_η≈583 ms and η≈741 μm evaluated with Equation (4.1) and (4.2):

$$\boldsymbol{\tau_\eta} = \left(\frac{\tau^2}{\epsilon_d^+}\right)^{\frac{1}{2}}, \tag{4.1}$$

$$\boldsymbol{\eta} = \left(\frac{\delta^4}{\epsilon_d^+}\right)^{\frac{1}{4}}, \tag{4.2}$$

Where ε_d^+ is the turbulent dissipation in wall unit obtained from the DNS database [(Kim John, 1987)]. Relative length and diameter of the fibers to the length scales of the flow, L_f/η, L_f/δ_ν, d_f/η and d_f/δ_ν are equal to 1.62,6,0.013 and 0.05 respectively. In the present study the relaxation time of the fiber is τ_f =37 μm which is obtained with Equation (4.3) (Voth & Soldati, 2017), therefore Stokes number (defined in chapter 2.2) is St=0.00087.

$$\boldsymbol{\tau_f} = \frac{\rho_f d_f^2}{18\mu} \frac{\lambda \ln(\lambda + \sqrt{\lambda^2 - 1})}{\sqrt{\lambda^2 - 1}}, \tag{4.3}$$

In the centre of the channel, the Kolmogorov time scale should be used to estimate the Stokes number rather than the viscous time scale of the flow, therefore at the centre of the channel St=6.35x10^{-5}. In both cases the Stokes number is small enough to neglect any possible inertial effect.

The initial images had a size of 1600 x 2560 pixels, then they were cutted and reduced to 1570x2560 pixels. This choice was necessary to eliminate the noise due to the reflection of the glass (the images were cutted exactly at the wall).

From these images it was possible to perform PIV measurements again using PIVlab from MATLAB. The window size and time resolution chosen are given in the for lowest Reynolds number case Re_τ=180.

Image sequencing style	**Time resolutions**	**IW size 1st pass**	**IW size 2nd pass**	**IW size 3rd pass**	**IW size 4th pass**
[-]	[ms]	[pixels]	[pixels]	[pixels]	[pixels]
Pairwise	2.5	64x64	32x32	32x32	32x32

Table 4.8: PIV setting parameters for Re_τ=180.

In addition, to these images the processes of discrimination and modeling of the fibers depicted respectively in chapters 3.2.1 and 3.2.2 were applied. The thresholds for intensity and Area, together with the standard deviation for the Gaussian smoothing filter ('Sigma' in the table) applied during these processes are listed in Table 4.9.

Intensity Threshold	**Lower Area Threshold**	**Upper Area Threshold**	**Sigma**
[-]	[pixels]	[pixels]	[-]
300	50	200	1.5

Table 4.9: Discrimination setting parameters for Re_τ=180.

The thresholds and parameters depicted above came from the observation of the available data and the results of the discrimination process afterwards (an example of the applied discrimination process on a single frame is given in Figure 3.2-2).

The results of the discrimination and modeling of the fibers will be given in Chapter 5. In detail, probability density functions of the length of the fibers and of the curvature

coming from the reconstruction will be shown. Alipour M. in his thesis (Alipour M. , 2021) worked with the same type of fibers and the results regarding the PDFs after the reconstruction are given in Figure 4.5-1: the peaks of the PDFs indicates that the most probable fiber length and normalised curvature are respectively L_f=1.26 mm and k^*=0.31. Therefore the results obtained in this thesis will be discussed in comparison to the available data here reported.

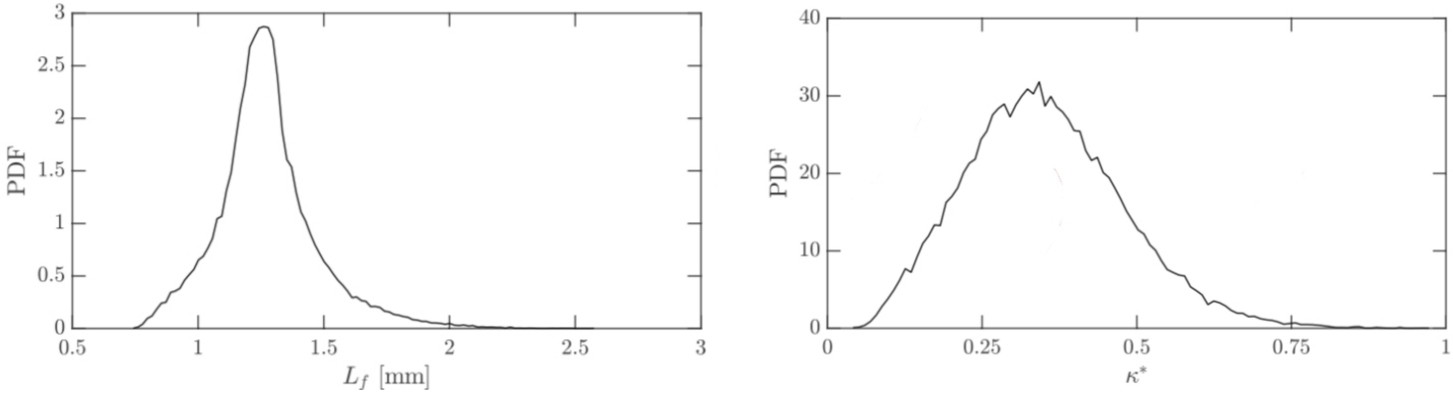

(a) PDF of the fiber's length.

(b) PDF of the normalized curvatures.

Figure 4.5-1: PDFs results from Alipour M. (2021).

5 Fibers

In the present chapter the results regarding the fibers detection and modeling processes will be presented. Firstly, the quality of the reconstruction of the fibers will be discussed, focusing on the most common errors encountered during the process of reconstruction. Although an overview of the quantities that can be derived by the reconstruction and their calculation will be given. Finally an image with reconstructed fibers in the channel will be shown at the end of the chapter.

5.1 Reconstruction quality

After applying the thresholds and filter, from the results it was possible to check the quality of the reconstruction process, in order to validate the method employed and recognize the most common errors that could occur. Firstly, well reconstructed fibers are shown. From Figure 5.1-1 it clearly appears that modeling was successful: despite the presence of a very close particle to the fiber, the process was able to discriminate it from the tracer. This was due the use of the Gauss smoothing filter (application on raw image is shown in Figure 5.1-1(c, since the particle was not eliminated from area nor intensity thresholds (otherwise it would have not appeared in Figure 5.1-1b.

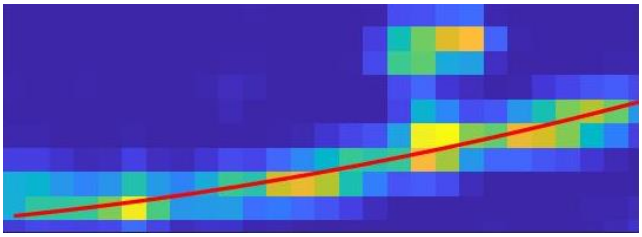

(a) Reconstructed fiber (in red) on raw image.

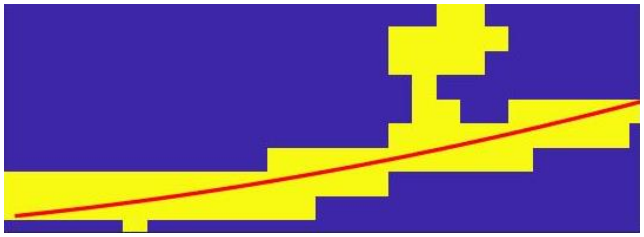

(b) Reconstructed fiber (in red) on binarized image.

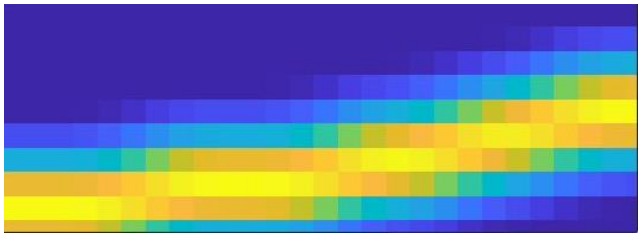

(c) Gauss filter applied on the raw image.

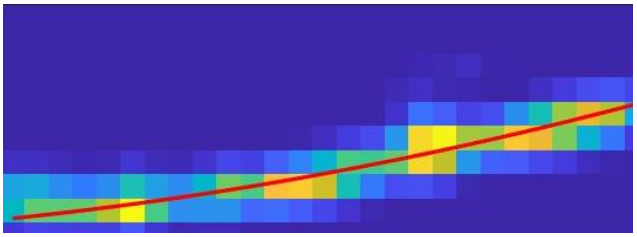

(d) Reconstructed fiber (in red) on discretized image.

Figure 5.1-1: Gauss smoothing filter effect.

In the case depicted in Figure 5.1-2 instead the elimination of the particle (the circular object on the right in the figure) is due to area threshold because the particle has an intensity in the core which is comparable to the one of the fiber and therefore it could not have been eliminated by the set intensity threshold. This leads to a good reconstruction of the fiber.

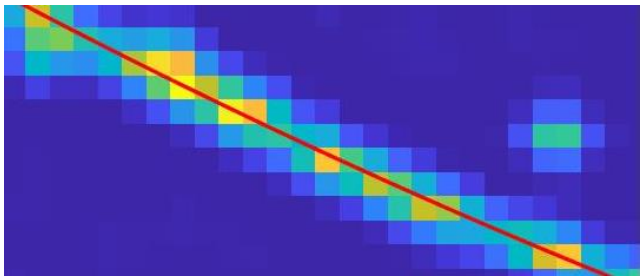

(a) Reconstructed fiber (in red) on raw image.

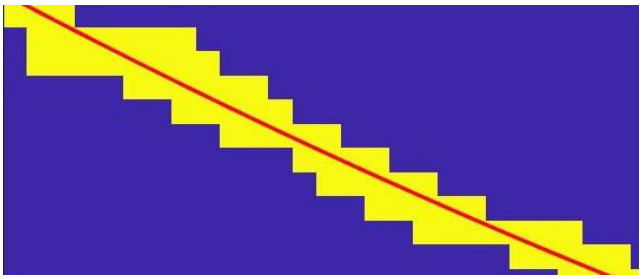

(b) Reconstructed fiber (in red) on binarized image.

Figure 5.1-2: Area thresholds effect.

Nevertheless, errors could occur. In Figure 5.1-3 a group of very close tracers were mistaken by the code as a singular fiber. This error is quite common and it's due to the

high density of tracers in the flow. For future works it is suggested the application of an adequate and more stringent area threshold or a new way of seeding particles to the flow (in the case of this set of experiments, the seeding was performed manually).

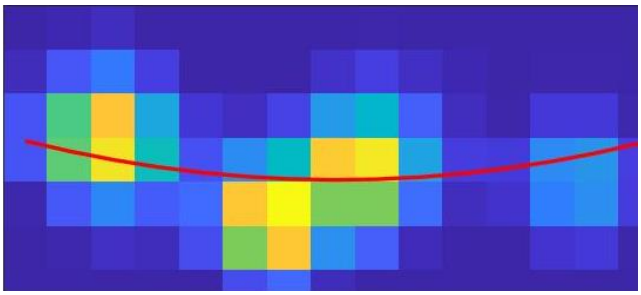

(a) Reconstructed fiber (in red) on raw image.

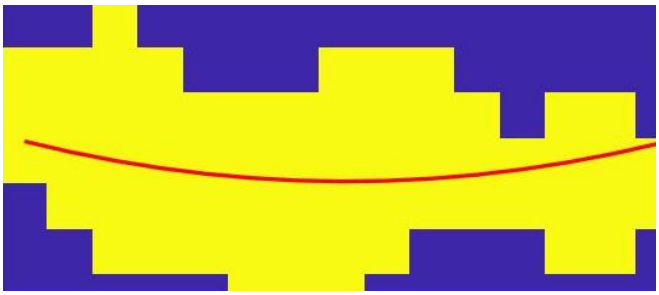

(b) Reconstructed fiber (in red) on binarized image.

Figure 5.1-3: Cluster of particles mistaken for a fiber.

Finally, in Figure 5.1-4 the particle close to the fiber was not eliminated by the thresholds nor from the filter. Consequently, the fiber is not well reconstructed and the derived curvature and lengths will erroneously modify the results. For future works it is suggested the application of a set of different parameters for thresholds and sigma for the Gauss smoothing filter in the discrimination phase with the objective of finding the most suitable combination of parameters to obtain the best results in the reconstruction.

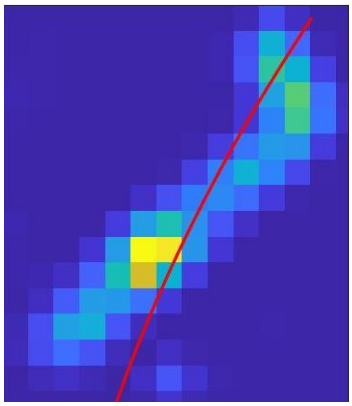

(a) Reconstructed fiber (in red) on raw image.

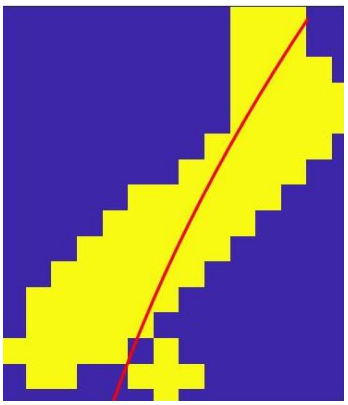

(b) Reconstructed fiber (in red) on binarized image.

Figure 5.1-4: Error in the reconstruction.

5.2 Curvature and effective length

The fibers used in this study can be considered as slender body particles having high length-to-diameter ratio. As specified in Table 4.1 in chapter 4.1 they are characterized by a manufactured nominal length L_f=1.2 mm.

From the reconstruction of the fibers, it was possible to derive other properties such as: length L_f, effective length L_{eff} and curvature k. Where L_{eff} is defined as the distance between the two ends of the fiber, where in case of straight fibers coincide with L_f, which can be calculated as the length of an arc [(Arc length, n.d.)]:

$$\mathbf{L_f} = \int_a^b \sqrt{1 + \left(\frac{dy}{dx}\right)^2}\, dx\,, \tag{5.1}$$

Where a and b define respectively the x coordinates of the starting and end point of the fiber and y the coordinates of the 2nd order polynomial used to approximate the fiber. To evaluate the curvature k first the local curvature k_l must be defined [(Curvature, n.d.)]:

$$\boldsymbol{k_l} = \frac{|y''|}{(1+y'^2)^{3/2}}\,, \tag{5.2}$$

Finally, the curvature k can be obtained as:

$$\boldsymbol{k} = \frac{1}{L_f}\int_a^b |k_l|dx\,, \tag{5.3}$$

The length of the reconstructed fibers can be calculated by computing the Probability density function (PDF in Figure 5.2-1a) of the length of all the fibers reconstructed in the experiment (Chapter 4.5). The representative length is chosen to be the peak of the PDF that corresponds to L_f=1.15 mm which is slightly lower than the one nominal one.

The mean curvature is k is normalized by k_0 ($k^*=k/k_0$), which is calculated as the curvature of an arc of half circle with length equal to the mean length of the fibers (i.e., $k_0=\pi/\bar{L}_f$). Therefore, a classification of the fiber according to their curvature can be given using the normalized quantity k^*:

- If k*=0 then the fiber can be considered straight;
- If k*=1 then the fiber is semi circumference shaped.

The PDF of the normalized curvature k* is reported in Figure 5.2-1b. From the comparison between the results of this thesis and Alipour M. shown in Figure 4.5-1a-b it appears clear how the errors introduced in the discrimination phase have erroneously modified the expected results of the fibers properties. Indeed the PDF in Figure 5.2-1a shows a peak at lower lengths which is not present in Alipour's results, despite of that the value of the most probable fiber length (L_f=1.15 mm) is not that far from the one specified in the manufacturing sheet. On the other hand the probability density function of the normalised curvature gives a very different result: the most probable k^* in the reconstruction depicted in this work is of the order of 0.05, practically straight fibers. It was observed how this very low value was due to the presence of the two types of errors presented above: either the reconstruction was not able to detect the real curvature of the fiber due to the presence of close particles or a cluster of particles was mistaken as a single fiber (latter in particular gives commonly straighter configurations). It is however interesting to see how k*=0.35 (same value resulted from Alipour analysis) is however still a local maximum for the PDF obtained from the current study.

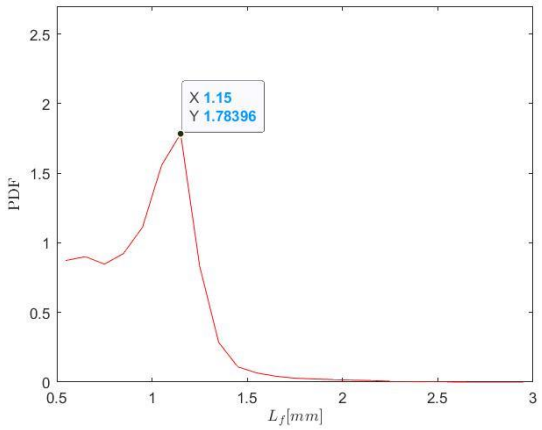

(a) PDF of the fiber's length.

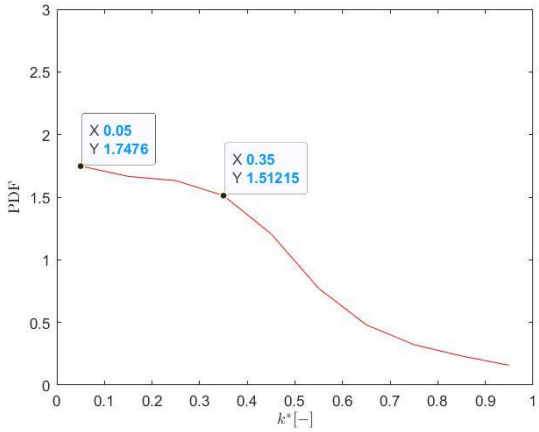

(b) PDF of the normalized curvatures.

Figure 5.2-1: PDFs for fiber laden flow at Re_τ =200.

Finally, assuming that the fiber is part of a circumference, the effective length can be calculated analytically by knowing the curvature of the fiber k using the following correlation:

$$\boldsymbol{L_{eff}} = \frac{\sqrt{(2 - 2\,cos(kL_f))}}{k}, \tag{5.4}$$

At this point it was interesting to show the distribution of normalised curvatures and effective lengths of the fibers available in this study (Figure 5.2-2). After the analytical

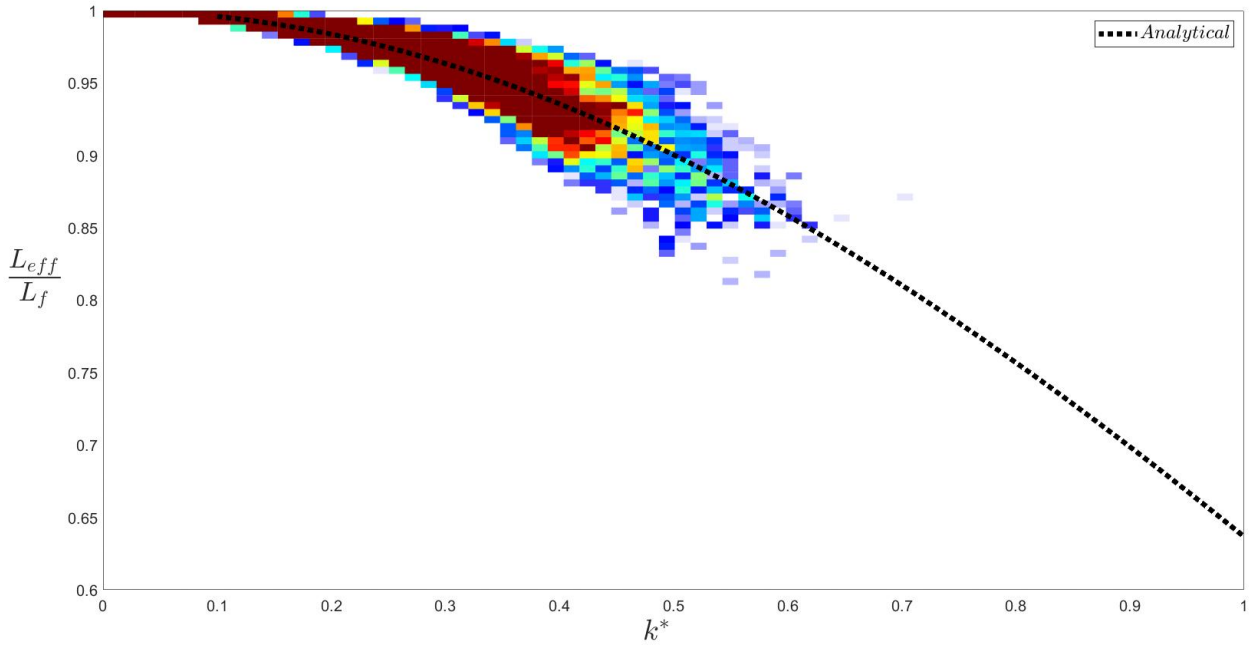

Figure 5.2-2: Joint PDF of effective length normalised by the fiber length with curvature distribution of the fibers.

prediction (black dashed curve in Figure 5.2-2) was plotted: the curve was obtained substituting $k=k_0 \cdot k^* = \pi/\bar{L}_f k^*$ in Equation (5.4).

From the figure it can be observed that the distribution is quite symmetric with respect to the analytical predictions and mostly the fibers examined in this thesis are concentrated at the top and left part of the length and curvature ranges respectively.

5.3 Final discussion

The main target of the reconstruction process presented in this work, including not only the discrimination of the raw images but also the following modeling of the fibers, was to obtain a reliable and efficient tool to use for future tracking of the fibers in turbulent channel flow with the main objective of studying their dynamic. In the optic of that, the results from Chapter 5 regarding the reconstruction the fibers and its validation can now be discussed.

The main difficulty encountered in the full processes of reconstruction was the choice of the initial thresholds for the discrimination process and this is due to large variability in terms of intensity ranges and area available in the raw images and, therefore, of a large multiplicity of possible choices and combinations. In addition, the tracers density in the flow is very high and, as a consequence, this may lead to the formation of clusters of particles and therefore modify erroneously the results on the properties of the fibers (as it happened for the probability density function of the normalized curvatures k* presented in Figure 5.2-1b). On the other hand, too stringent thresholds could lead to the detection of a much smaller number of fibers with respect to the ones present effectively in the channel and as specified in the beginning of the discussion, this would end up in a large lack of information for the tracking of the fibers. Therefore a compromise must be performed.

For future works and projects it is suggested an optimization of the setting parameters for the discrimination phase of the reconstruction together with a better seeding of the particles and fibers in the channel. As seen, indeed, seeding was performed manually for this work, thus a better injection method could lead to less particles being sticked together in the channel.

6 Unladen Flow

Once that the experiments for the three values of friction Reynolds chosen and already depicted in the previous chapters (Re_τ=187,368,726) were conducted, the results on the turbulence statistics can be obtained. After the experiments, the resulting images were pre-processed and cutted and from those PIV measurements were performed with additional package PIVlab on Matlab. After obtaining the statistics derived from available velocity field data coming from PIV, the experimental results were compared with direct numerical simulations and experimental data coming from the literature.

Primarily the reason why turbulence statistics are so relevant for the aim of this work is that they provide an important research tool in studying basic physics of turbulence. In addition to that, turbulence statistics are also decisive for the successful assessment of the flow's quality and, specifically the objective of this thesis, the assessment of the Water Channel present at the TU department. Finally they provide a validation of the PIV set-up parameters (defined in chapter 4.3 and recalled in the following subchapters).

According to the common notion, turbulence in the near-wall layer is approximately universal, when quantities are scaled in wall units (i.e., the friction velocity u_τ and the viscous length-scale δ_v). Nevertheless the universality has been put into question by a series of studies which highlighted a series of divergences from the universal structure when Re_τ changes [(Bernardini, Pirozzoli, & Orlandi, 2014)].

So firstly, for each of the three Reynolds numbers the first and second order statistics were studied. Starting from the mean properties (first order statistic), the profiles of the mean velocity non-dimensionalized by the wall-shear velocity were obtained. In addition, the rms of the normalized fluctuations of the streamwise and normal velocities were compared afterwards. For the second order statistics, the Reynolds stresses' behaviour were then evaluated. In particular, higher order moments (i.e., skewness and flatness) of velocity fluctuations were used to discuss and quantify the non-Gaussian and intermittent behaviour of the turbulence structures. Finally the universality of near wall turbulence in the channel will be then examined in the limits

of the available data comparing the best combinations of time and spatial resolutions found in previous subchapters for the three studied cases.

6.1 Re_τ=187

The lowest of the friction Reynolds numbers chosen was Re_τ=180 and the fluid used for the experiment is water at the average temperature of 24.15°C, corresponding to dynamic viscosity μ=0.9107x10^{-3} Pa·s. The whole data set for this Reynold consists of N=4816 images. The details of flow and imaging parameters for the considered experiment is reported in Table 6.1.

Re_τ	$Re_{\tau,eff}$	Phase	resolution	f	u_τ	τ	δ_v
[-]	[-]	[-]	[px]	[Hz]	[m/s]	[s]	[mm]
180	187	water	1563x512	1000	0.0043	0.0503	0.214

Table 6.1: Summary of the wall scales and imaging parameters adopted.

6.1.1 Mean velocity profiles

So, the profile of the mean streamwise velocity non-dimensionalized by the wall-shear velocity u_τ is shown in Figure 6.1-1. Additionally to the experimental data, results coming from Direct Numerical Simulation of Moser for Re_τ=180 [(Moser, Kim, & Mansour, 1999)] is depicted in grey and in black the theoretical laws of the wall and the log wall are represented. The different time and space resolutions chosen as inputs for the PIV measurements for the current case are summarized in Table 6.2. In addition, in the same figure also an error is evaluated: error is meant as the difference between the points coming from the numerical simulation results of Kim, Moser et al. (that perfectly fits the theoretical lines) and the obtained experimental points at a given wall unit y^+. Consequently a negative error indicates the overestimation of the mean velocity with respect to the one predicted by the numerical simulations, instead a positive value indicates an underestimation.

The experimental points calculated in this work follow the DNS and theoretical lines whatever is the choice of space and time resolutions: from the figure it can be observed that the best results are obtained for low time resolutions and intermediate window size choice as 16 and 24 (i.e., dt=4ms represented as a red curve in the figure). On one

hand the results of this work well follow the theoretical line in the logarithmic region (with a small error at the end of the curve at almost half height of the channel), however a small discrepancy appears in the buffer and wall region where the mean velocity is overestimated. Nevertheless in the latter regions the error is restrained in a range from 0 to -1.5, which is quite low and acceptable considering that turbulence near the wall presents a major variability due to a major presence of fluctuations for values of $y^+ < 20$ (as it will be shown in next subsections).

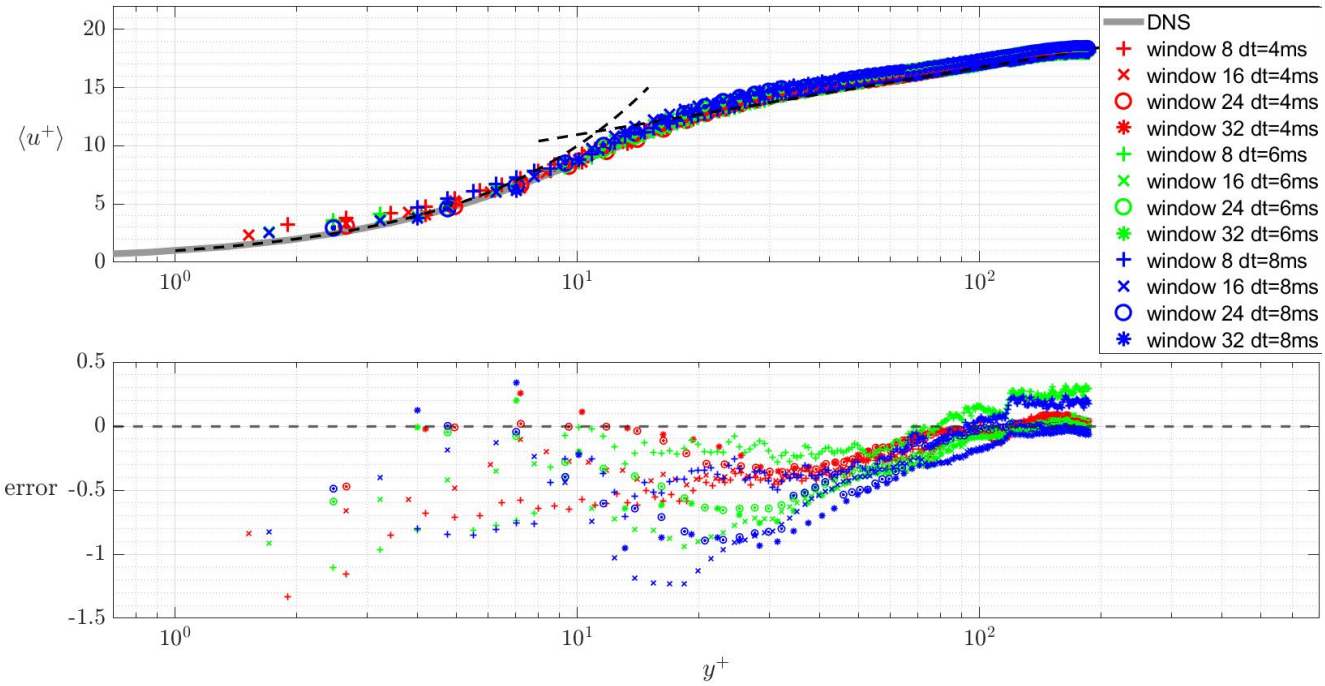

Figure 6.1-1: Mean velocity profiles normalized by u_τ and associated error.

Acquisition time dt	**Colour**	**D_I**			
[ms]	**[-]**	**[px]**			
4	red	8	16	24	32
6	green	8	16	24	32
8	blue	8	16	24	32

Table 6.2: Summary of the PIV input parameters of case Re_τ=180.

As expected, bigger window's size choices will give less data in the vicinity of the wall but appear to be more accurate (24 and 32 in the Figure 6.1-1) and this can be observed for every choice of time resolution. The major availability of data for smaller IW dimensions is due to an increase of the spatial resolution (parameter introduced in chapter 3.1.5): indeed for the current recording system set-up the DSR is 390,194,127 and 96 for 8,16,24 and 32 IW sizes respectively. On the other hand, increasing the size gives some improvements: indeed it leads to a significant reduction of the number of spurious velocity vectors, due to an increase of the number of particles for each window [(Lavoie, Avallone, & al., 2007)].

Since overall the error is quite small, for the case of Re_τ=187 the difference in the acquisition time is not of great relevance, even though it appears very clear from the figure that the greatest acquisition time is the one which is mostly affected by error (blue markers in the picture): indeed the mean velocity is mostly overestimated, especially in the log law region.

So, from the observation of the results, one of the best set up among all the choices, with respect to the error, is most probably a window of 24x24 size with the smallest time resolution (i.e., dt=4 ms). Despite the sublayer, also the choice of a window's size of 8x8 with a dt=6ms is well fitting the DNS result, especially in the buffer and log-law region (starting from $y^+ \approx 10$). For dt=6ms again the 24 window's size is interesting since it well reproduce the results in the vicinity of the wall. It's certain that a good agreement is obtained with the greater sized window (i.e., 32) at least for smaller time acquisitions, but the first experimental data is available at much larger number of wall units compared to smaller window's sizes: in fact, for 32x32 the first available data is obtained for y^+ =4.2, for the other choices they are available in a range of wall units from 1.6 and 2.6. Therefore a smaller sized window appears to be more efficient for the investigations on the near-to-wall behaviour of the flow.

6.1.2 Turbulence intensities

At this point it was considered interesting the introduction of a set of flow velocity statistics that were analysed in order to shed light on the turbulent behaviour of the flow. Therefore the turbulence intensities were calculated, normalized by the wall-shear velocity and shown in wall units and in global coordinates (where δ is the mid height of the channel). From previous discussion it was decided to show only three choices of window's sizes (i.e., 8, 16 and 24) also with the objective to have a more readable graph.

So in the Figure 6.1-2a the results for root-mean-square of the velocity fluctuations coming from the numerical simulation of Kim for Re_τ =187 are represented in a solid

grey line and in grey circles the data from hot-film anemometer measurements [(Kreplin & Eckelmann, 1979)] for Re_τ=194 are shown. Instead, in the Figure 6.1-2b the results from Kim are shown for the global coordinates. The symmetry of the

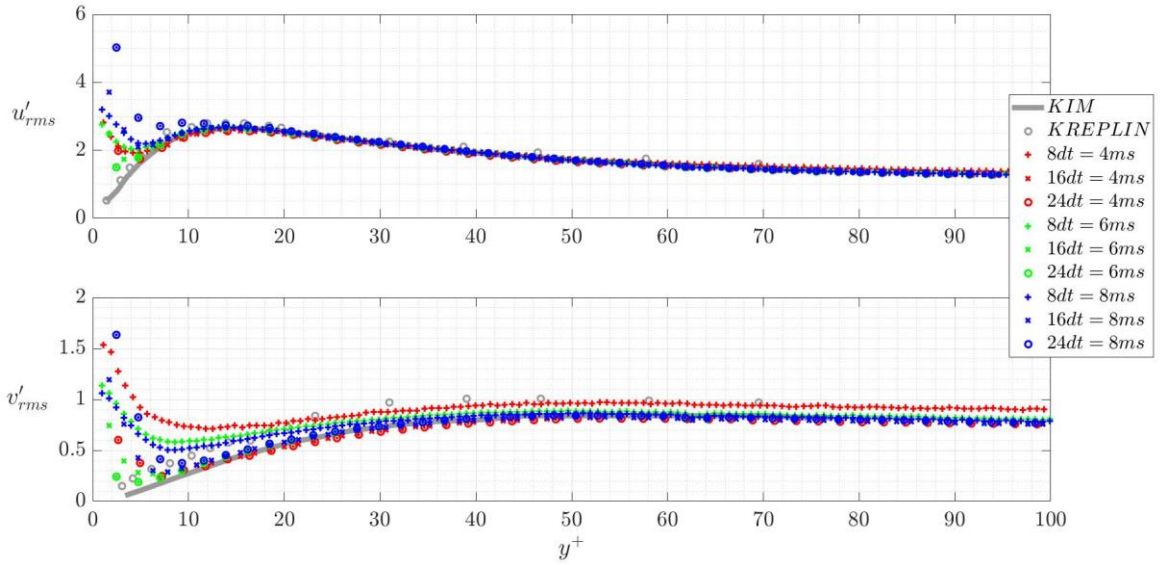

a) In wall units.

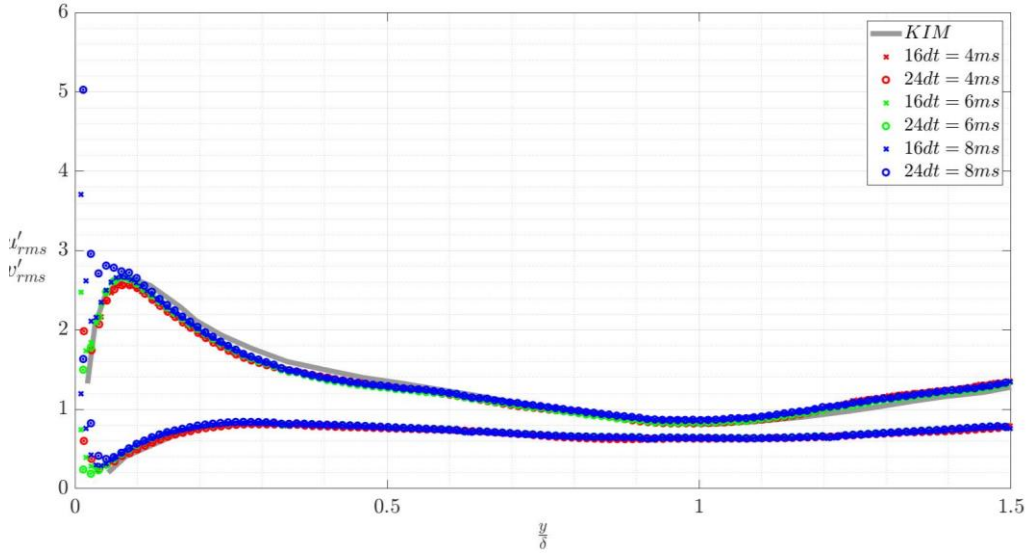

b) In global coordinates.

Figure 6.1-2: Root-mean square velocity fluctuations normalized by u_τ.

profiles in global coordinates about the centreline indicates the adequacy of the sample taken for the root mean square [24]. More than in the mean velocity profiles now it's clear how the biggest time resolution (i.e.; dt=8 ms) is not able to detect the near wall turbulent behaviour neither of the streamwise nor of the normal component of velocity. In addition, the 8 pixels sized window shows the largest discrepancies with the data coming from literature at every time resolution.

From the graphs shown in Figure 6.1-2 it can be noticed how turbulent channel flow is characterized by higher fluctuation for the streamwise component of velocity at wall unit $y^+<20$, presenting a peak at around $y^+\approx12$. Finally it must be noticed that the normal component of the velocity fluctuations shows values of an order of magnitude lower than the one of the streamwise component: therefore v' is also much more affected by spatial and time resolutions.

6.1.3 Reynolds stresses

Upon the consideration done for previous statistics, for Reynolds stresses it was decided to show only the results for the window's dimension 16 and 24 (see Figure 6.1-3). Also in this case the error should be evaluated to indicate the most suitable PIV set up: for the Reynolds stresses it was introduced only the discrepancy for the normal stress in the x direction. This choice arose from the observation that the other components (i.e., R_{vv} and R_{uv}) show almost zero discrepancy with respect to numerical data at all time and space resolutions. In addition, for this case it was purposely chosen to not include the higher time resolution results, since they show a very large error in the vicinity of the wall for the normal component resulting on an overestimation of it.

The best fitting of the numerical lines (grey in the figure) is obtained for dt=6 ms. For dt=4 ms the trends of the experimental data are different from numerical ones in the vicinity of the wall, in particular in the figure it's clear the underestimation of the peak of the R_{uu} for the case of dt=4ms. Finally it is noticeable that for dt=6ms the two windows well follow the numerical results from Moser. The error appears to be higher in the vicinity of the wall and tends to 0 for the outer region starting from $y^+ > 60$.

So, as it happened for the mean streamwise velocity, also for the Reynolds stresses the trends are in accordance with the literature and the best configuration for the smallest Reynolds number available is given by a window of 16 or 24 with a time resolution of dt=6 ms.

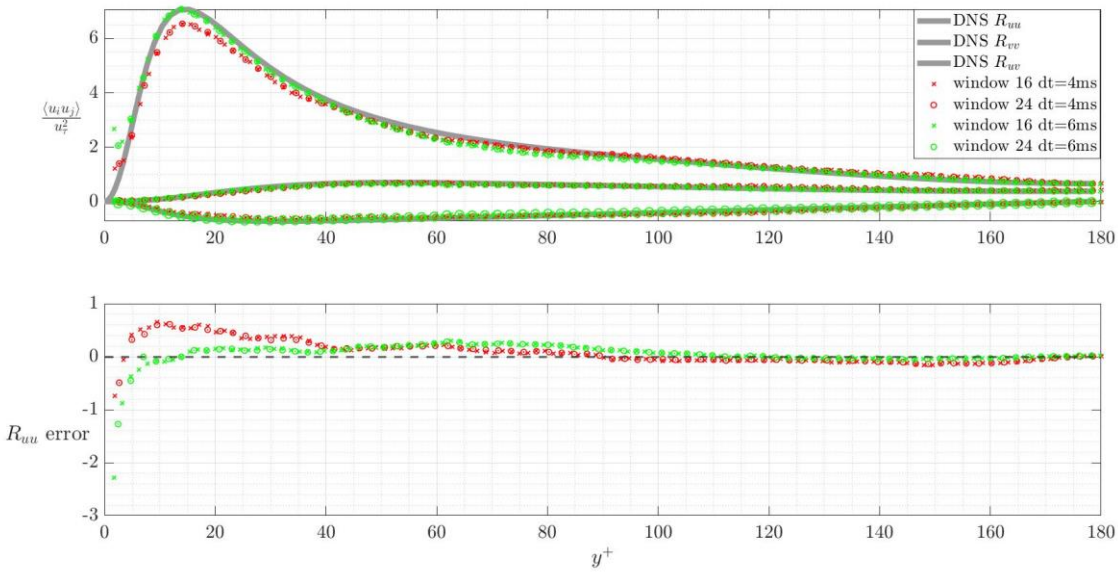

Figure 6.1-3: Reynolds stresses normalized by u_τ and associated error.

6.1.4 Skewness and flatness of fluctuations

The non-Gaussianity of turbulence can be quantified by the value of third- and higher-order moments of variables: so the so-called skewness and flatness, that for a given generic quantity q are given by the Equation (6.1) and (6.2):

$$\boldsymbol{S(q)} \equiv \frac{\langle q'^3 \rangle}{\langle q'^3 \rangle^{\frac{3}{2}}}, \tag{6.1}$$

$$\boldsymbol{F(q)} \equiv \frac{\langle q'^4 \rangle}{\langle q'^2 \rangle^2}, \tag{6.2}$$

If the probability distribution of the generic quantity q is Gaussian then the values are 0 and 3 for the skewness and flatness respectively.

For the current case it was chosen to show only one of the three time resolutions for best readability of the results: for $Re_\tau = 187$ it was chosen the intermediate resolution. The results were compared with data coming from DNS of (Kim John, 1987) and (Vreman W., 2014), hot-film anemometry measurements (Kreplin & Eckelmann, 1979) and LDV (i.e., laser-Doppler velocimeter) measurements by (Barlow & Johnston, 1985).

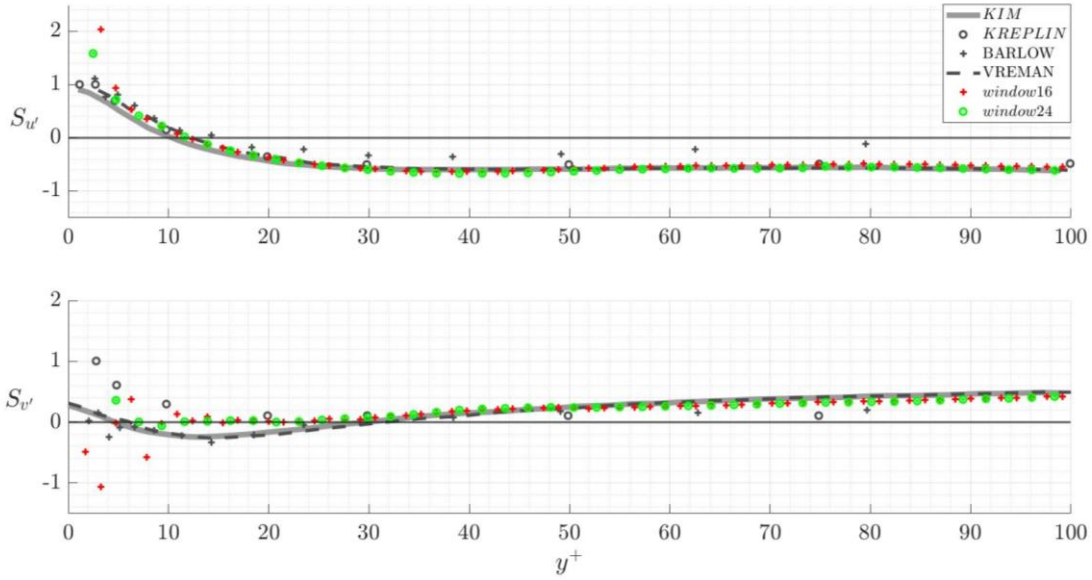

(a) Skewness profiles.

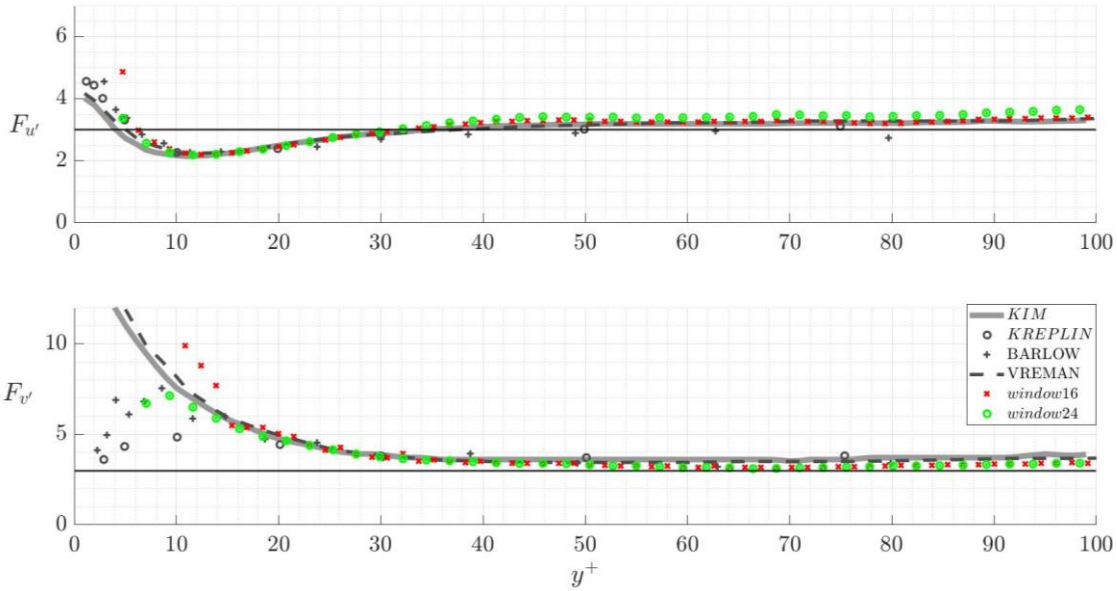

(b) Flatness profiles.

Figure 6.1-4: Higher order statistics of velocity fluctuations.

As visible from Figure 6.1-4.a-b the skewness and flatness of the velocity fluctuations u′ and v′ are significantly different from the values of a Gaussian distribution (discrepancies from 0 and 3 horizontal black lines) and these discrepancies increase as the wall is approached. On the other hand there is a good agreement with literature: especially Vreman data are well followed for skewness and flatness of the u′ component. The biggest discrepancies with literature data are seen for the skewness of v′, detecting, differently from the literature, a more Gaussian behaviour (0 valued skewness). This could be since being v′ a magnitude of order lower than u′, major errors are expected and these are enhanced in the vicinity of the wall. Indeed, especially for flatness profile of v′ it was decided to cut off some of the experimental data in the proximity of the wall, since F(v′) converged to values around 100, which is not supported by any values in the literature (where F(v′) converges to values around 22 and 29.2 for Vreman).

So the negative skewness profile of u′ indicates that for $y^+>10$ the regions with u′ display stronger peaks than regions with positive u′ [(Vreman W., 2014)]. According to the profile of skewness of v′, there exist a positive v′ motion from $y^+\approx30$ and slight negative motion or nearly 0 motions for lower values of wall units.

As said flatness measures the intermittency of a quantity: so it's clear that the maximum intermittency occurs near the wall for both the components of fluctuations. A strongly intermittent signal at some point is dormant most of the time. This result is supported by Vreman et al.: indeed from the observation of v′ snapshots (see (Vreman W., 2014)) in planes parallel to the wall in the viscous sublayer (i.e., $y^+\approx3$) show scarce presence of regions with noticeable normal velocity fluctuation compared to the centre of the channel. This was explained considering that structure with relatively large normal velocity fluctuation can hardly penetrate into the viscous sublayer, but occasionally a vortex is pushed down toward the wall, but these are typically streamwise vortices.

6.2 Re_τ=368

The same experiment was conducted for the shear Reynold number Re_τ=368. The water at the average temperature of 23.8 °C, corresponding again to dynamic viscosity $\mu=0.9107\text{x}10^{-3}$ Pa·s. The whole data set for this Reynold consists of N=5036 images. The details of flow and imaging parameters for the considered experiment is reported in the table.

Re_τ	$Re_{\tau,eff}$	Phase	Resolution	f	u_τ	τ	δ_v
[-]	[-]	[-]	[px]	[Hz]	[m/s]	[s]	[mm]
360	368	water	1563x512	1000	0.0084	0.0128	0.108

Table 6.3: Summary of the wall scales and imaging parameters adopted.

6.2.1 Mean velocity profiles

So, the profile of the mean streamline velocity non-dimensionalized by the wall-shear velocity u_τ is shown in the Figure 6.2-1 together with the associated error per unit wall. Similarly to previous chapter, added to the experimental data, in grey the result coming from Direct Numerical Simulation of Moser now for Re_τ=395 (Moser, Kim, & Mansour, 1999) is depicted and in black the theoretical laws of the wall and the log wall are represented. Due to the increased Reynolds number (larger fluctuations) and consequently increased uncertainty in the measurements, a larger error range is expected in this case with respect to the one depicted in previous sub-chapter. Again the different resolutions represented are summarized in the Table 6.4. To make the error graph readable, in addition, the error range was purposely reduced: so the very large discrepancy of the first available value for the dt=4ms and window 8 acquisition (i.e., the "+" blue marker in Figure 6.2-1) is not shown.

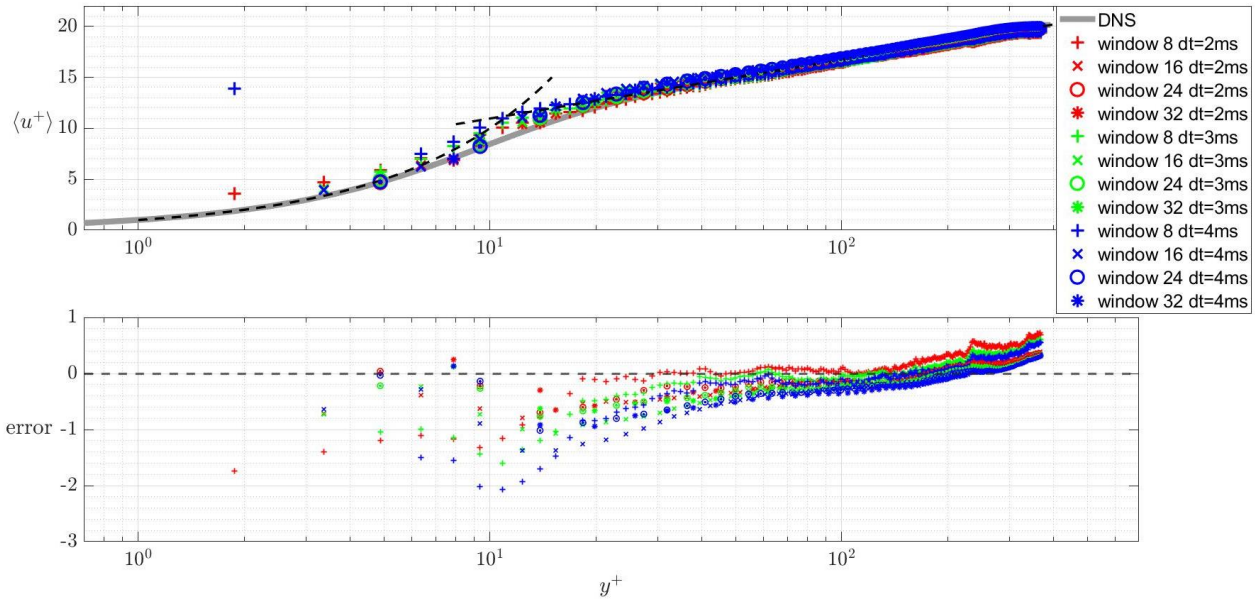

Figure 6.2-1: Mean-velocity profiles normalized by u_τ and associated error.

Similarly to previous case, the error tends to decrease from the linear region to the log law at higher wall unit, but in this case the discrepancies now show a similar trend given a certain dt. It must be noticed that on an average, the biggest time resolution (i.e., dt=4 ms in this case) gives a greater overestimation of the experimental results with respect to the others. Therefore a more interesting choice is represented by smaller time resolutions. As expected again, small sized windows give not so accurate results in the sublayer and in general for $y^+ < 10$, thus again bigger sized ones seem more interesting, even though the first available data is at higher number of wall units. As said, the reason why bigger sized window seems to have a smaller error is due to the inability of small dimensions windows to successful detect the higher displacements of the particles (that are now moving faster compared to previous case).

Acquisition time dt	**Colour**	**D_I**			
[ms]		**[px]**			
2	red	8	16	24	32
3	green	8	16	24	32
4	blue	8	16	24	32

Table 6.4: Summary of the PIV input parameters of the case Re_τ=360.

6.2.2 Turbulence intensities

Also in this case it is interesting to show the turbulence intensities. Nevertheless, both the graphs are shown in Figure 6.2-2b, where in the wall units graph the results from DNS of Kim et al. [(Moser, Kim, & Mansour, 1999)] for Re_τ=395 are shown.

Similar conclusions to lower Re_τ case can be given for the current graph. The main difference is that even with smaller time resolutions the turbulence behaviour of both fluctuation's components is not well represented near the wall and the discrepancy of the v' component is becoming more relevant than previous case.

From Figure 6.2-2b it can be again assured that the sample taken for the calculations of the root mean square is adequate because the profiles are symmetric [24].

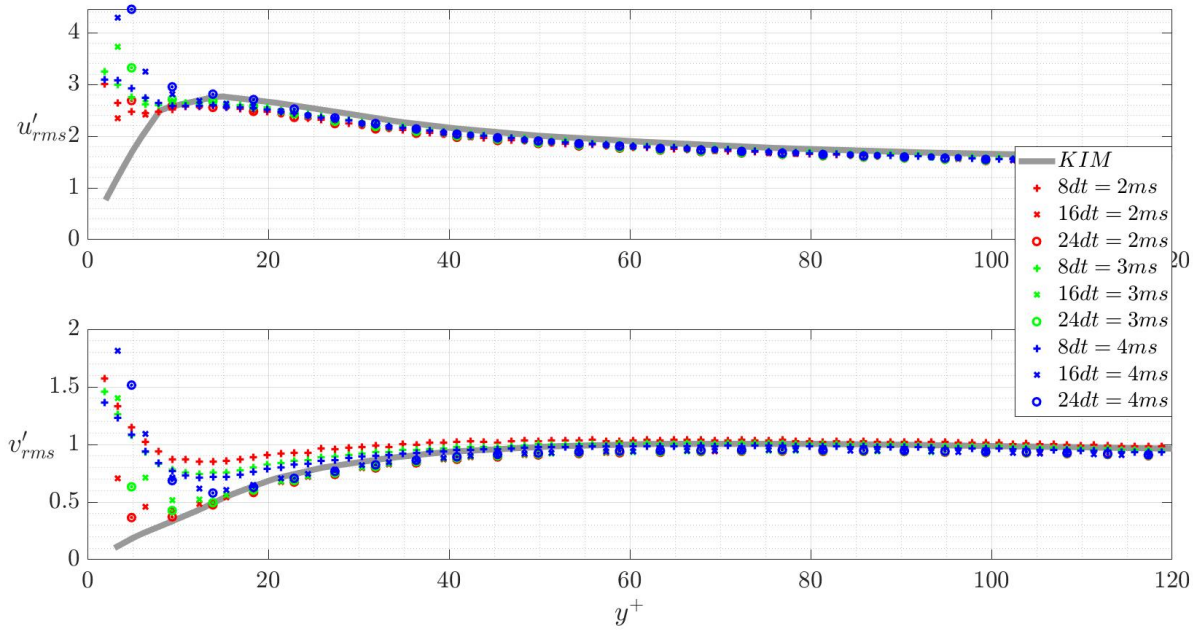

a) In wall units.

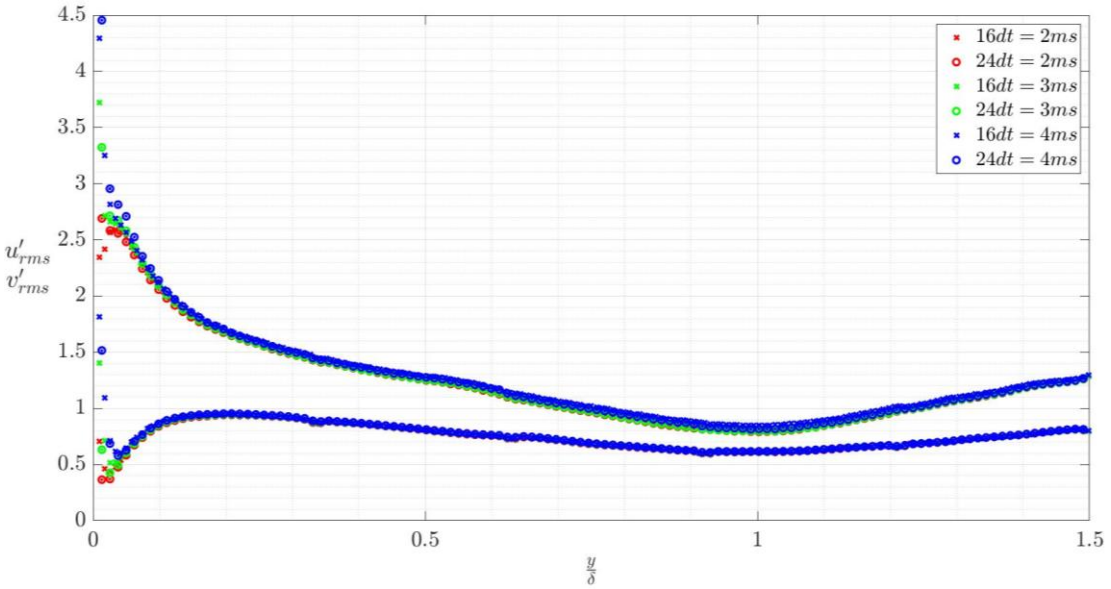

b) In global coordinates.

Figure 6.2-2: Root-mean square of velocity fluctuations normalized by u_τ.

6.2.3 Reynolds stresses

For what was discussed for the mean velocity profiles, the Reynolds stresses for this case are shown only for the window's dimension 16 and 24 (see Figure 6.2-3).The same discussion made for the error in the mean profile shown must be repeated for the second order statistics: indeed also in this case the error range is expected to be larger due to increased Reynolds number. Also the biggest time resolution available was not used for the evaluation of Reynolds stresses since it gives, whatever is the window's size choice, to a high overestimation of the normal stress R_{uu} in the vicinity of the wall, as a consequence of the overestimation of the u'.

The best fitting of the numerical lines for $y^+ > 6.$ is obtained for dt=2 ms. A notice must be now mentioned: as previously said the available data for the choice of dt=3 ms were of particular interest too, especially near the wall. But for the Reynolds stresses, especially for R_{uu} component, this choice underestimates the actual peak for both window dimensions. Nevertheless, in the vicinity of the wall the time results coming from dt=3 ms show a similar trend to the DNS results, unlike the smaller time resolution.

So as visible from the figure, the two window's sizes well follow the numerical results from Moser for the R_{vv} and R_{uv} components. Instead a shifting downward and leftward of the remaining component of the experimental data with respect to the numerical ones is present. This discrepancy could be due to the difference between the numerical and experimental Re_τ (395 and 368 respectively); nevertheless Kim in his research [24] points out that this gap is not sufficient enough to cause the difference shown in the figure for the mean profiles of velocity, but with major probability this effect of the lower Re_τ could be more significant in Reynolds stresses field.

Other than that, the Reynolds stresses present trends that are in accordance with the literature.

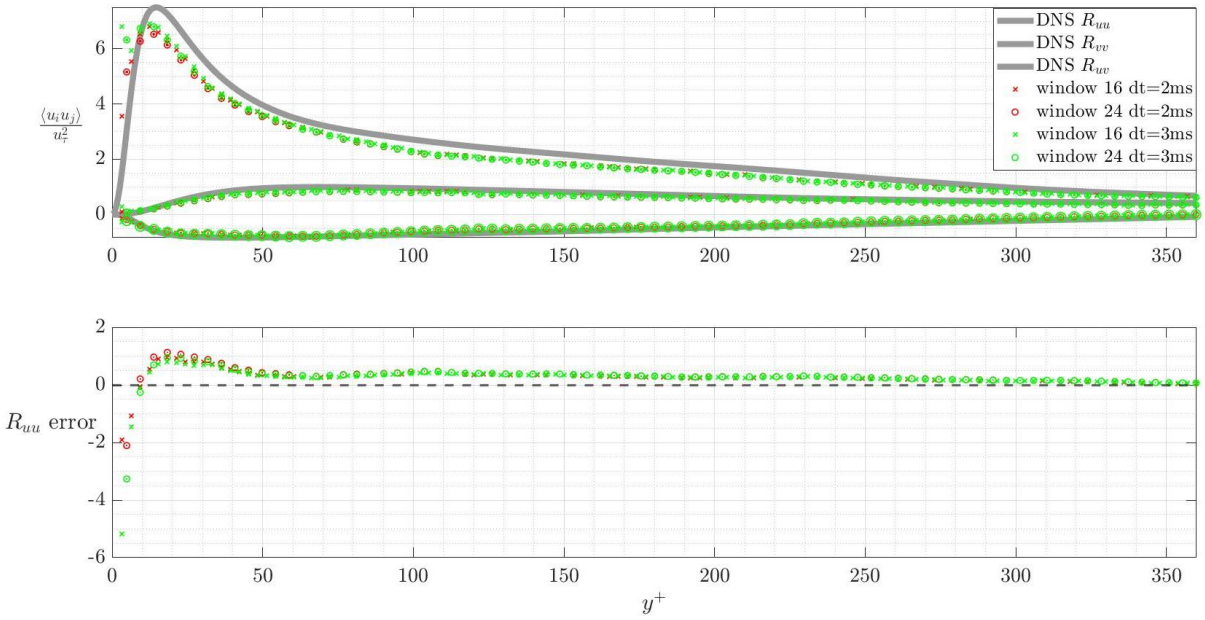

Figure 6.2-3: Reynolds stresses normalized by u_τ and associated error.

6.2.4 Skewness and flatness of fluctuations

Also for the intermediate case the higher order statistics were analysed: for the intermediate case there is a lack of data in the literature for these statistics. Nevertheless it was still decided to show the obtained results with the objective of providing a comparison with previous case in terms of magnitude and behaviour of these profiles. Also in this case it was chosen to choose one time resolution for a better readability of the graphs (i.e., dt=3ms).

The skewness of the u' component of fluctuation show a similar trend as the one depicted in previous case; a first positive region followed by a negative one: the main difference is that this happens for lower values of y^+ (around 20 here). Since the order of the statistic is higher for flatness, thus more error is expected, for u' it is quite different the vicinity of the wall (instead it converges for high wall units): especially higher IW size introduce a positive peak which is not supported by any data in the literature.

For the normal component velocity fluctuations the trends for both statistics are expected to worsen when comparing to previous ones for the reasons depicted above: even though in the vicinity of the wall the trend appears similar to the one depicted for the low Re case (especially for 24 sized interrogation window), the skewness of v'

presents a major oscillatory behaviour which is probably due to an not adequate number of sampling data used for the its calculation [24]. The flatness profile on the other hand (since many points for low valued y^+ with magnitudes of the order of 50-100 were cut off) appears instead quite similar: as a consequence intermittency here seems decreased in magnitude, therefore a larger region of normal velocity fluctuations is expected near the wall for higher Reynolds number.

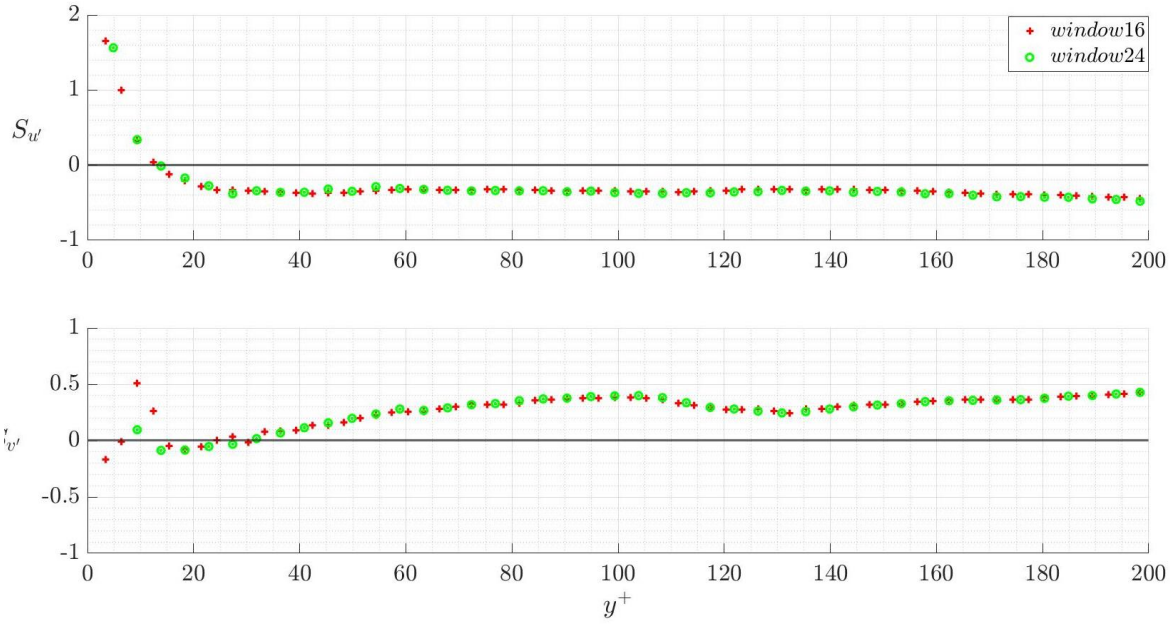

(a) Skewness profiles.

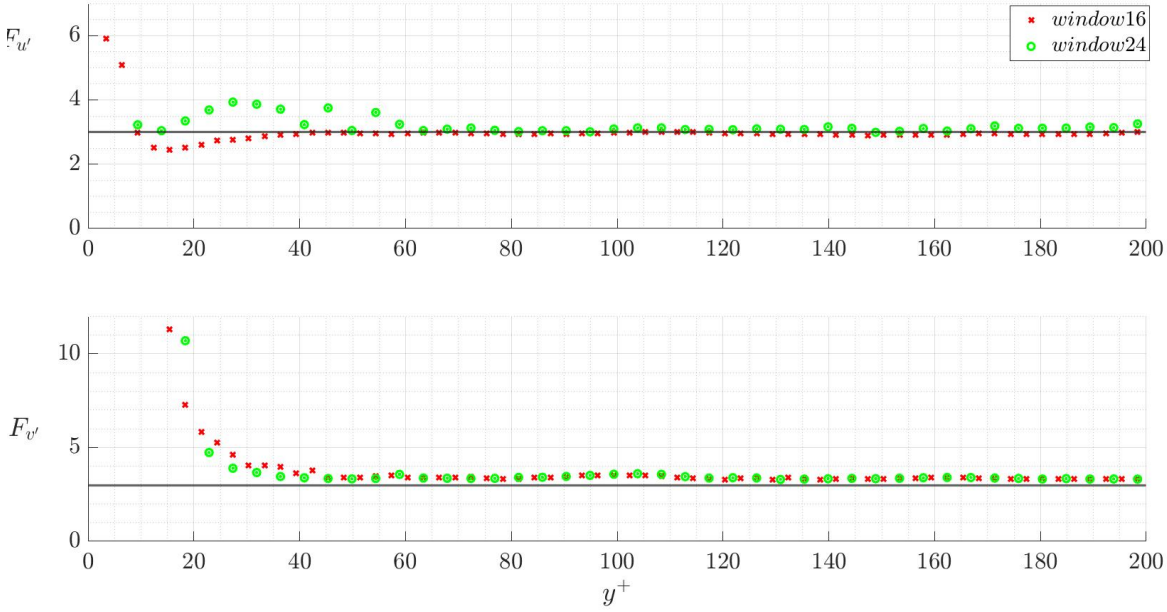

(b) Flatness profiles.

Figure 6.2-4: Higher order statistics of velocity fluctuations.

6.3 Re_τ=726

Finally the experiment was repeated for the highest Re_τ in data set available (i.e., Re_τ=726). The water for the experiment was at a temperature of 24 °C. The whole data set for this Reynold consists of N=6000 images. The details of flow and imaging parameters for the considered experiment is reported in the table.

Re_τ	**$Re_{\tau,eff}$**	**Phase**	**Resolution**	**f**	**u_τ**	**τ**	**δ_v**
[-]	**[-]**	**[-]**	**[px]**	**[Hz]**	**[m/s]**	**[s]**	**[mm]**
720	726	water	1563x512	1000	0.0165	0.0033	0.0551

Table 6.5: Summary of the wall scales and imaging parameters adopted.

6.3.1 Mean velocity profiles

So as previous chapter, the profile of the mean streamline velocity non-dimensionalized by the wall-shear velocity u_τ is shown in the Figure 6.3-1 together with the associated error. In this case since the Reynolds number is higher and image shifting was not employed, in the figure only one time resolution is present. Again, added to the experimental data, in grey the result coming from Direct Numerical Simulation of Moser now for Re_τ=590 [(Moser, Kim, & Mansour, 1999)] is depicted and in black the theoretical laws of the wall and the log wall are represented. The different cases represented are summarized in the Table 6.6. Since now Reynolds number is higher than previous cases, also 32 sized window was employed for the PIV measurements.

The 8x8 window, as expected from chapter 3.1.6, overestimates the curve at low y^+: this overestimation only affects that window and disappears for larger window's choices. The least affected by error is surely the 32x32 window, but all the sublayer region is not covered and all the information related to that area are lost. So a compromise must be performed: intermediate sizes are preferred as for the other Re_τ for the study of higher order statistics.

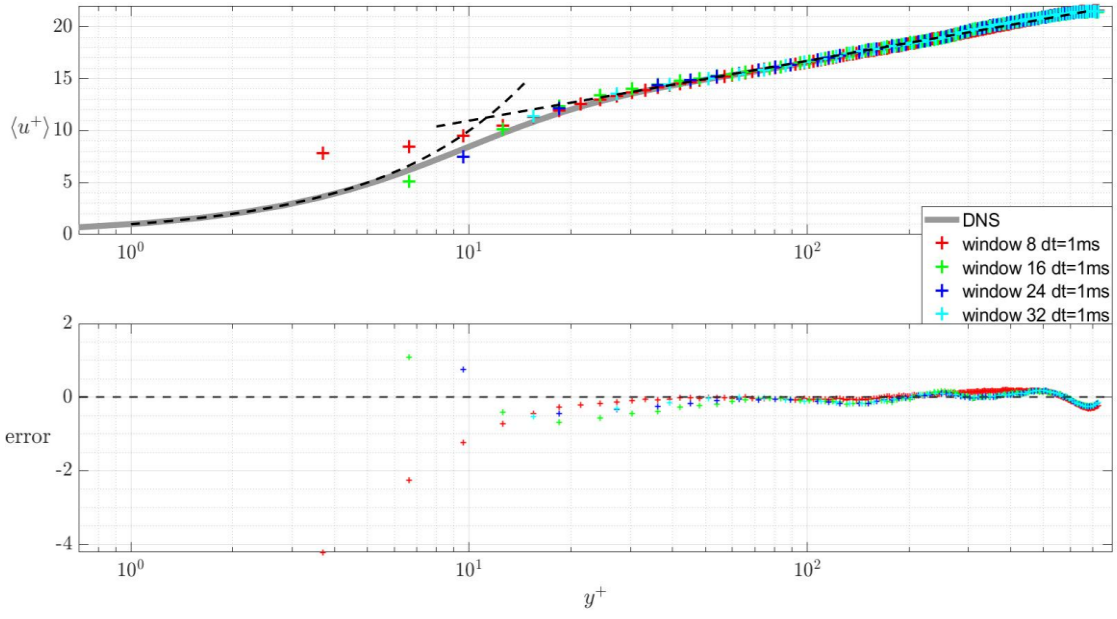

Figure 6.3-1: Mean-velocity profiles normalized by u_τ and associated error.

Acquisition time dt	**Colour**	**D_I**			
[ms]		**[px]**			
1	red	8	-	-	-
1	green	-	16	-	-
1	blue	-	-	24	-
1	cyan	-	-	-	32

Table 6.6: Summary of the PIV input parameters of the case Re_τ=720.

An important notice must be made: for higher Reynolds values data near the wall are unavailable and this is due to the viscous lenghtscale that decreases when Re_τ increases (i.e., δ_v in Table 6.5). Consequently, in fact, the first value of wall unit y^+ is higher with respect to other low and intermediate friction Reynolds.

6.3.2 Turbulence intensities

As done previously, also for Re_τ=726 the fluctuations are calculated. In particular the data set used for the comparison with the literature in this case, represented in grey in Figure 6.3-2a-b is from a numerical simulations of the turbulent incompressible flow in plane channels at Re_τ=550 [(del Alamo & Jimenez, 2003)].

As expected, the current case is the worst among all the cases considered in this thesis and the experimental results near the wall are highly overestimated due to the presence of erroneous velocity vectors near the wall.

Even though the difference is very low, at high wall units (i.e., y^+>100), especially for the normal component of fluctuations, 24 pixels sized window best suits the data coming from literature. For this case for future measurements it's suggested the use of bigger interrogation windows as 32 or 64 with the objective of giving best data in the vicinity of the wall (even though much of the information for viscous sublayer would be lost).

Also in this case, from the observation of the symmetry of data with respect to the mid height of the channel in Figure 6.3-2b it can be assured that the number of samples used for the statistics was adequate.

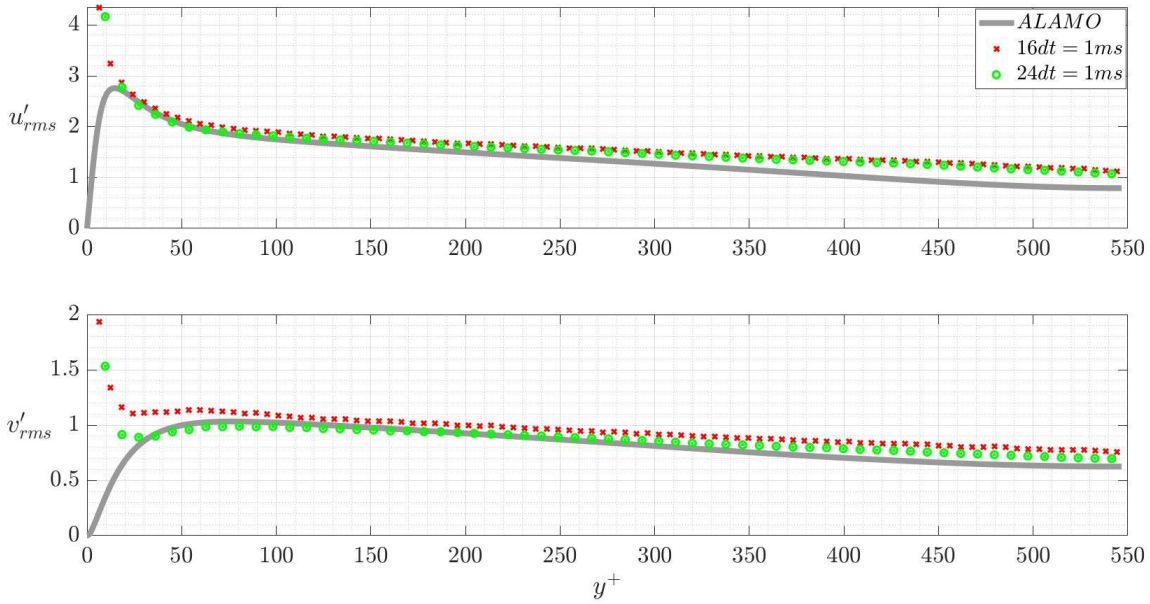

(a) In wall units.

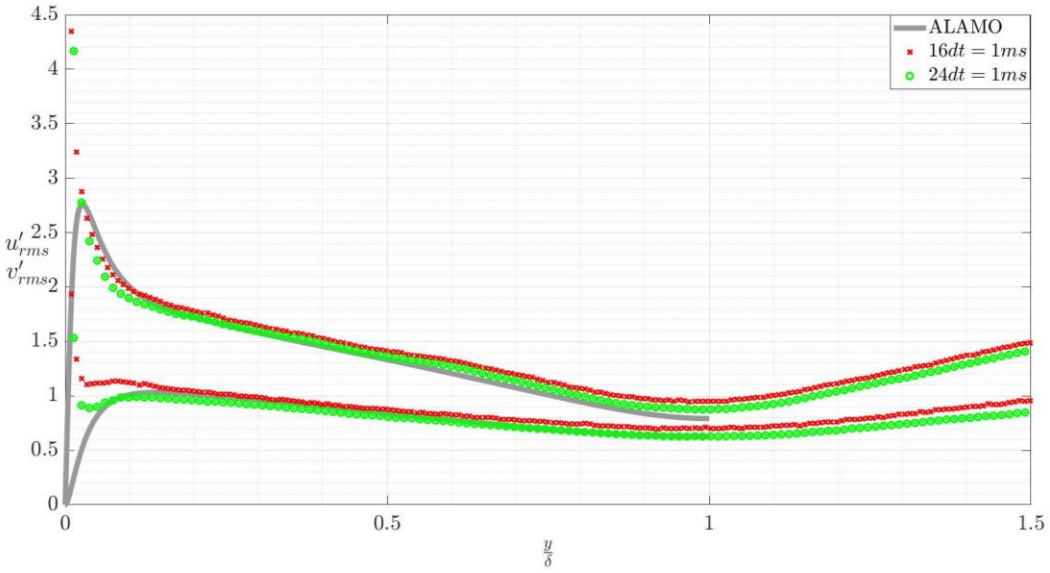

(b) In global coordinates.

Figure 6.3-2: Root-mean square velocity fluctuations normalized by u_τ.

6.3.3 Reynolds stresses

So, again, the Reynolds stresses are shown only for the window's dimension 16 and 24 (see Figure 6.3-3). Also in this case it was chosen to show only the error associated with the normal stress R_{uu}.

Similarly to the intermediate case (Re_τ=360), the two windows well follow the numerical results from Moser only for the R_{vv} and R_{uv} components. It is certain that the lack of data in the vicinity of the wall is explainable with the same discussion done for the mean velocity.

Despite R_{uu} in the sublayer region and in general for $y^+ < 10$, as it happened for the mean streamwise velocity, also for the Reynolds stresses the trends are in accordance with the available literature.

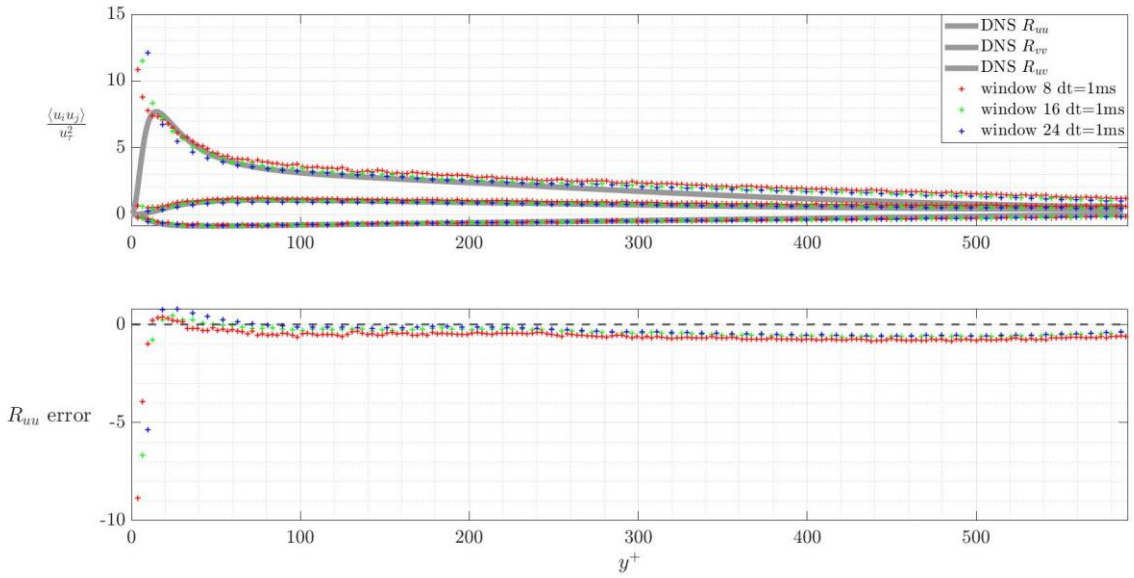

Figure 6.3-3: Reynolds stresses normalized by u_τ and associated error.

6.3.4 Skewness and flatness of fluctuations

Finally higher order statistics are studied for the high Reynolds case: same discussion could be done as for the intermediate case. More noisy profiles are expected for v' due to its relatively small magnitude (where relatively is related to the streamwise component of fluctuations).

Even though the profiles appear noisier than the ones in previous case, for the 24 sized IW choice the Skewness and Flatness of u' component show a similar trend to Re_τ=187: again the change in sign in the skewness profile is given for lower values of wall units (y^+ around 20) as it happened for the intermediate case.

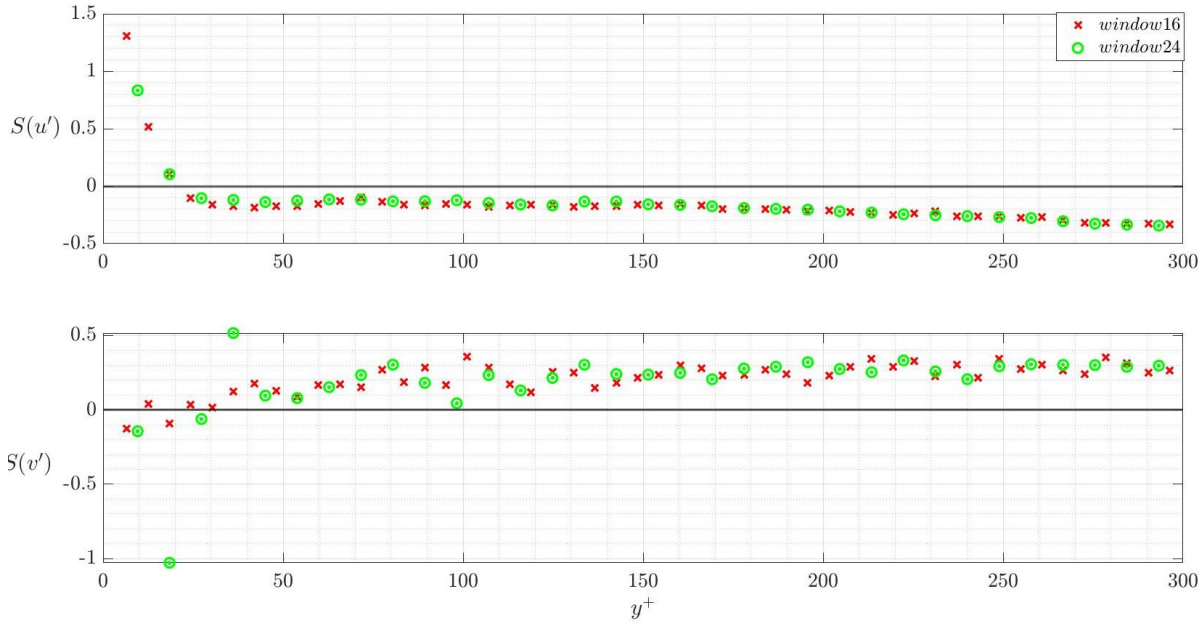

(a) Skewness profiles.

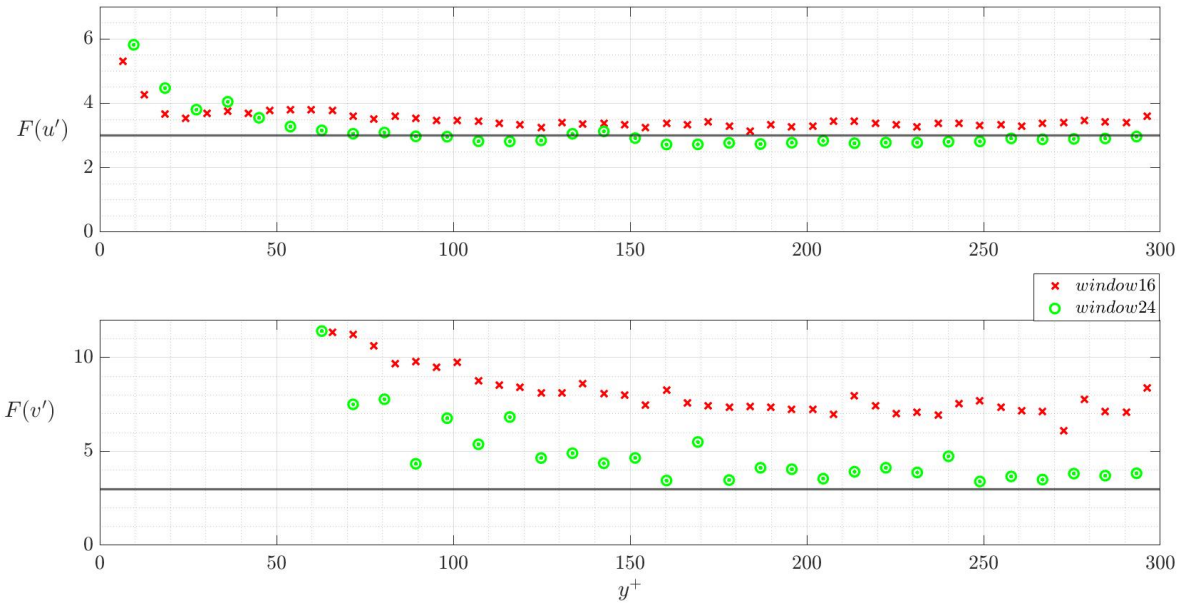

(b) Flatness profiles.

Figure 6.3-4: Higher order statistics of velocity fluctuations.

As said the profiles for v' especially appear more scattered: the small region of negatived skewness in the vicinity of the wall is lost for this case, despite of that the values are converging similarly to previous Reynolds number profiles for high y^+. Finally flatness profile for v' is worsening but still the trend is followed for 24 sizes window.

6.4 Universality of turbulence

Modern turbulent-boundary layer calculation methods must use turbulence models because direct numerical simulation of the Navier-Stokes equation is beyond the reach of the present-day computers for very high Reynolds numbers. Therefore new models must be constructed on the experimental database, but due to the expenses of large-scale facilities and the difficulty in accurately measuring high-Reynolds-number flows, most of the available data in the literature is for low and intermediate Reynolds numbers. Because the majority of the applications of engineering interest are at much higher Reynolds number, it is critical to understand the dependence of the flow on Reynolds number [(DeGraaf & Eaton, 2000)].

6.4.1 Mean velocity profiles

According to DeGraaf and Eaton the log law has proved to be an effective universal curve for the mean velocity profile in the inner region and only around twenty years ago the doubts about its validity begun to arise. In Figure 6.4-1 the three profiles were compared: notice that the for time and space resolution for the data displayed the best combinations was chosen for the three cases (i.e., window size 24 and dt=6ms, dt=3ms and dt=1ms for Re_τ=187,368 and 726 respectively).

Good agreement in the linear law region (law defined in (2.13) is achieved for values of around $10 < y^+ < 12$: for lower values the available data show a small discrepancy among the Reynolds. Unfortunately due to the low spatial resolution it was not possible to detect at lower values of wall units y^+ for the intermediate and high cases, therefore the law of the wall (law defined in Equation (2.12) cannot be validated from this work.

In the buffer area instead data from the three cases collapse into one curve until $y^+ \approx 30$ (i.e., the log law region) is reached. From this point on there is a relevant difference among the cases and this trend is very similar to the one presented by Klewicki et al. [(Klewicki & Falco, 1989)]: while the intermediate and the high Reynolds numbers seem to overlap, the low Reynolds case is higher.

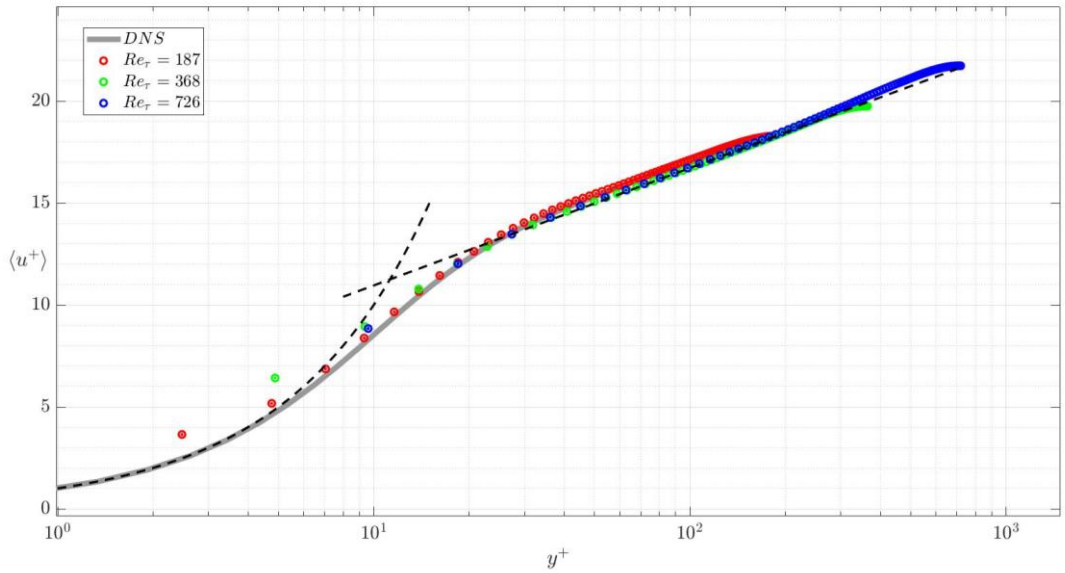

Figure 6.4-1: Mean velocity profiles normalized by u_τ for the three Reynolds number.

6.4.2 Turbulence intensity

While the mean streamwise velocity profile was widely accepted as universal and still mostly is (despite the discrepancies detected at very high Reynolds), a series of studies have highlighted how the most evident of the universal structure violations is represented by the near-wall peak of the streamwise turbulence intensity [(Bernardini, Pirozzoli, & Orlandi, 2014)].

In Figure 6.4-2 a close up on the data regarding the streamwise fluctuations for the three Reynolds numbers is given. In particular in Table 6.7 the values regarding the peak of the rms of the fluctuation and the coordinates of the peaks are displayed: (1) for the case of Re_τ=368 the third point was taken as the real peak value (and this choice is motivated by the observation of the comparison with the direct numerical simulation done in previous subchapter 6.2.2: see the green circle markers in Figure

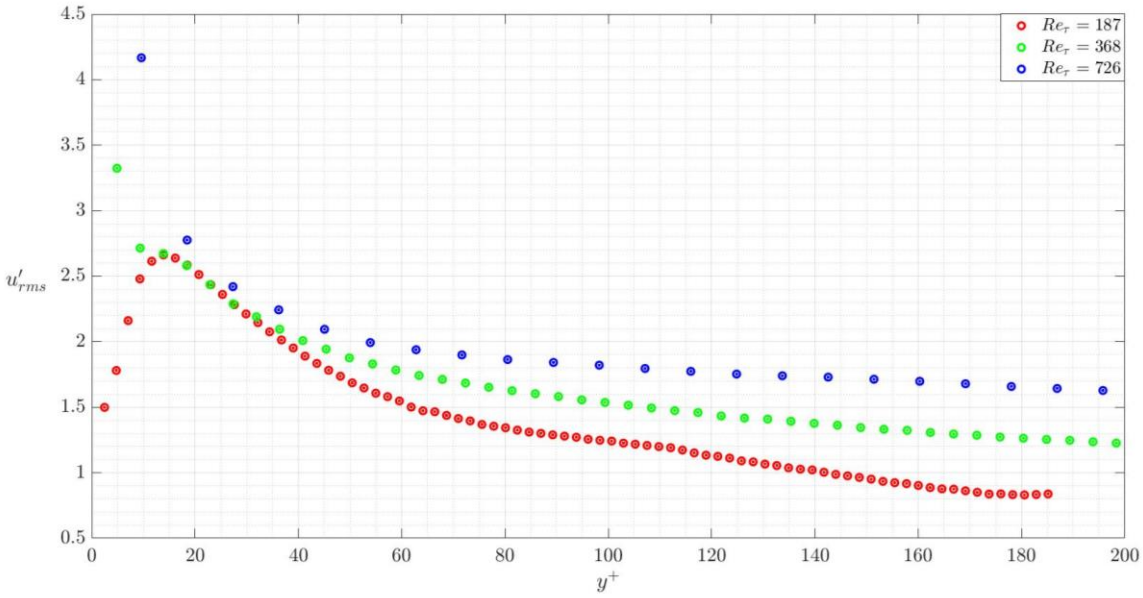

Figure 6.4-2: Streamwise fluctuation profiles for the three Reynolds number.

6.2-2)); (2) for the case of Re_τ=726 the values in the table were obtained from the observation of del Alamo results (results seen in subchapter 6.3.2).

What can be observed is that as pointed out in much literature ((Bernardini, Pirozzoli, & Orlandi, 2014), (DeGraaf & Eaton, 2000), (Klewicki & Falco, 1989), (Marusic & Kunkel, 2003)) , the maximum peak of the rms of the fluctuating streamwise velocity component dimensionalized with the inner scale (i.e., u_τ) is increasing with increasing Re_τ and therefore the true peak value of the rms of u'/ u_τ is

Re_τ	**Peak value of u'_{rms}**	**Coordinate of the peak y^+**
180	2.6622	13.8905
360	2.6728	13.8737
720	2.7886	14.2680

Table 6.7: Peak and coordinate of for u'_{rms} for the three cases.

Reynolds-number dependent. In the current study the increase of the peak is very low but this is only due to the closeness of the Reynolds numbers analysed (indeed in the

literature values of friction Reynolds up to 10^4-10^6 were explored in order to probe high-Reynolds-number effects).

6.4.3 Reynolds stresses

Finally the streamwise normal Reynolds stress was studied. It is generally assumed a priori that if the mean flow near the wall scales on inner coordinates, then so too must the Reynolds stresses [(Townsend, 1956)]. Thus also the Reynolds stresses are almost always normalized by inner scales, u_τ and δ_v. Unfortunately, the collapse of the Reynolds stresses in inner scaling is generally not supported by measurements [(DeGraaf & Eaton, 2000)]. So in the figure the close up on the adimensionalized streamwise normal stress R_{uu} is given. Also for this statistic the values regarding the peak and the associated wall unit are displayed: (1) for the case of Re_τ=726 the values in the table were obtained from the observation of the Moser results (results seen in subchapter 6.3.3).

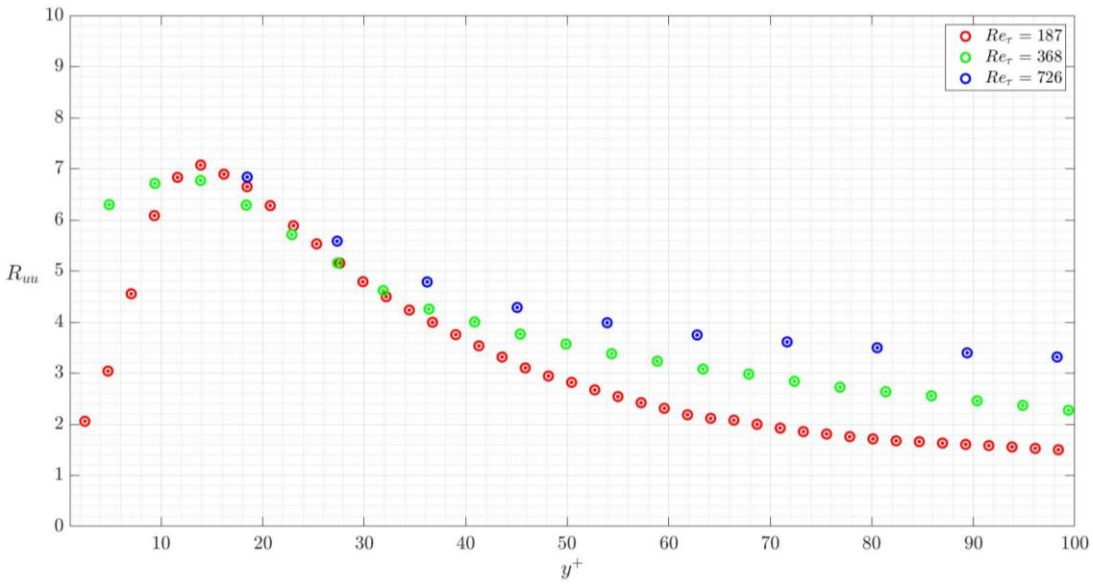

Figure 6.4-3: Streamwise normal stress profiles for the three Reynolds number.

In this study the peak doesn't seem very much affected by the Reynolds number and it can be discussed how also the location of the peak in wall units doesn't seem to be affected by it: in our case there is a very slight drop of the peak between low and intermediate case, but since it's a minor deviance and the statistic is of the second order (so it is expected much more noisy results near the wall at higher Re_τ), it can be

assured that that drop is not Re-dependant. Up to these days on this doubt also the literature is stills divided: the flat-plate data from Purtel, Klebanoff and Buckley show an increase of the peak up to Re_θ = 1340 followed by a slowly decreasing peak for Reynolds numbers up to 5100, instead from the ten experiments performed by Sreenivasan it was concluded that both y^+ location and peak of $\langle u^{2^+} \rangle$ are sensibly independent of Reynolds number. Finally in Fernholz et al. work it was stated a weak Reynolds number dependence in the peak of the stress as well as a possible rise in the location of the peak from y^+=12 to 16 with increasing Re. Finally, as it happens also for the experiments analysed for this work, further from the wall all the profiles show a consistent increase in the magntude of $\langle u^{2^+} \rangle$ with increasing Re.

Re_τ	**Peak value of $\langle u^{2^+} \rangle$**	**Coordinate of the peak y^+**
180	7.0732	13.8905
360	6.7705	13.8737
720	8.1293	14.2680

Table 6.8: Peak and coordinate of for $\langle u^{2^+} \rangle$ for the three cases.

7 Conclusions

Two-dimensional Particle Image Velocimetry measurements were conducted in a turbulent channel flow at three different Reynolds numbers in case of unladen and fiber laden flows. From measurements of the instantaneous velocity fields (in the streamwise and normal directions) coming from unladen flow configuration it was possible to assure the flow quality of TU Wien Turbulent Water Channel with the study of turbulence statistics so to guarantee for future studies to work in statistically fully developed channel flow. Other than that it was possible to perform a data supported discussion on the uncertainty of the PIV measurements in developing these analysis by comparing the obtained results with the direct numerical simulations and experimental data from literature. Latter is much relevant considering that future projects will be conducted in the studied water channel at same Reynolds numbers using PIV technique: therefore this thesis is proposed as a starting database and lays the groundwork for future works employing PIV technique in TU Wien Turbulent Water Channel.

It was observed how these planar measurements were able to successfully detect the velocity fields from low to high Reynolds numbers (180 to 720), although the resolution was high enough to also perform the calculation of turbulence fluctuations that were expected to be only a few percentage of the mean flow velocity (order of 3%-4%). In addition, the turbulence statistics derived from those fields in general followed the trends available in the literature: for the right combination of time resolution dt and window size D_I , especially at low and moderate Re_τ, the results are good also for higher order moments as skewness and flatness of fluctuations, for which scarce or none experimental data is available in the literature at the moment. Finally the still uncertain universality of turbulence near the wall was investigated in the limitation of the data obtained in this work: for the mean velocity the trends appear similar to the literature, instead not much can be concluded on higher order statistics.

Despite the very small discrepancies for which different explanations were given in the thesis, the configuration was assured to be statistically a fully developed channel flow, although the measurements demonstrate that PIV is an efficient tool to study

turbulence near and far from the wall. It was indeed able to arrive at very small y^+ (microscales) compared to the experimental data in the literature, despite the presence of reflections of the glass and other sources of error that occur near the wall.

In addition to that, also a method for the reconstruction of microplastics fibers in the water channel from planar PIV measurements was proposed. Indeed, in the optic of future study on the dynamic of fibers through PIV technique, a preliminary reconstruction of the fibers from the images is needed in order to detect their position and therefore their motions and rotations during the experiments. Through the reconstruction, also properties as the length and the curvature were derived representing a step forward for the characterization of complex objects in turbulent channel flows. There are various topics of interest that could be tackled in the future based on the methodology used in this thesis for the reconstruction of the fibers: 3D PIV measurements of microplastic fibers in turbulence water channel, PTV measurements in water channel and so on. In fact the methodology proposed in this thesis has the flexibility to be implemented in different flow boundary conditions and fiber properties.

Bibliography

[1] (n.d.). Retrieved from https://tokinalens.com/product/at_x_m100_pro_d/.

[2] Heymsfield , A. J. (1977). Precipitation Development in Stratiform Ice Clouds: A Microphysical and Dynamical Study. *Journal of Atmospheric Sciences, 34*, 367-381. doi:10.1175/1520-0469(1977)034<0367:PDISIC>2.0.CO;2

[3] *3D Calibration.* (n.d.). Retrieved 7 2022, from lavision: https://www.lavision.de/en/download.php?id=3678

[4] Adrian, R. J. (1997). Dynamic ranges of velocity and spatial resolution of particle image velocimetry. *Measurement Science and Technology, 8*, 1393. doi:10.1088/0957-0233/8/12/003

[5] Alipour, M. (2021). *Orientation and rotation rates of non-axisymmetric fibers in turbulent channel flow.* Doctoral thesis, Technische Universität Wien, Institute of Fluid Mechanics and Heat Transfer.

[6] Alipour, M., De Paoli, M., Ghaemi, S., & Soldati, A. (2021). Long non-axisymmetric fibres in turbulent channel flow. *Journal of Fluid Mechanics, 916*. doi:https://doi.org/10.1017/jfm.2021.185

[7] *Arc length*. (n.d.). Retrieved from wikipedia: https://en.wikipedia.org/wiki/Arc_length

[8] Barlow, R., & Johnston, J. (1985). Structure of Turbulent Boundary Layers on a Concave Surface. *Journal of Fluid Mechanics, 65*, 439-459.

[9] Bernardini, M., Pirozzoli, S., & Orlandi, P. (2014). Velocity statistics in turbulent channel flow. *Journal of Fluid Mechanics, 742*, 171-191. doi:10.1017/jfm.2013.674

[10] *Canon EOS 77D- caratteristiche*. (n.d.). Retrieved 11 15, 2022, from canon: https://www.canon.it/

[11] Caridi, G. (2018). *Development and application of helium-filled soap bubbles : For large-scale PIV experiments in aereodynamics.* Dissertation, Delft University of Technology, Aerodynamics. doi:10.4233/uuid:effc65f6-34df-4eac-8ad9-3fdb22a294dc

[12] Christensen, K. T. (2004). The influence of peak-locking errors on turbulence statistics computed from PIV ensembles. *Experiments in Fluids, 36*, 484-497. doi:10.1007/s00348-003-0754-2

[13] *Curvature*. (n.d.). Retrieved from Wikipedia: https://en.wikipedia.org/wiki/Curvature

[14] DeGraaf, D. B., & Eaton, J. K. (2000). Reynolds-number scaling of the flat-plate turbulent boundary layer. *Journal of Fluid Mechanics, 422*, 319-346. doi:10.1017/S0022112000001713

[15] del Alamo , J. C., & Jimenez, J. (2003). Spectra of the very large anisotropic scales in turbulent channels. *Physics of Fluids, 15*. doi:DOI: 10.1063/1.1570830

[16] Eckelmann, H. (1974). The structure of the viscous sublayer and the adjacent wall region in a turbulent channel flow. *Journal of Fluidmechanics, 65*, 439-459.

[17] Erni, P., Cramer, C., Marti, I., Windhab, E., & Fischer, P. (2009). Continuous flow structuring of anisotropic biopolymer particles. *Adv Colloid Interface Sci., 150*, 16-26. doi:10.1016/j.cis.2009.05.005

[18] Eshghinejadfard, A., Hosseini, S. A., & Thévenin, D. (2019). Effect of particle density in turbulent channel flows with resolved oblate spheroids. *Computers & Fluids, 184*, 29-39. doi:https://doi.org/10.1016/j.compfluid.2019.01.027

[19] *f-number (ƒ/#) or Aperture/Iris Size how much light or heat a Camera Lens provides to thermal or visible sensor*. (n.d.). Retrieved 11 15, 2022, from infinitioptics: https://www.infinitioptics.com/glossary/f-number

[20] *https://www.schuster-beflockung.de/beflockungstechnik-blog/woher-kommt-der-name-flock-where-does-the-name-flock*. (n.d.). Retrieved from SCHUSTER .

[21] Johann, N. (1929). *Untersuchungen über die Strömungen des Wassers in konvergenten und divergenten Kanälen* (Vol. 289). Berlin.

[22] Kane, I. A., & al, e. (2020). Seafloor microplastic hotspots controlled by deep-sea circulation. *Science, 368 (6495)*, 1140-1145. doi:10.1126/science.aba5899

[23] Khayat, R., & Cox, R. (1989). Inertia effects on the motion of long slender bodies. *Journal of Fluid Mechanics, 209*, 435-462. doi:10.1017/S0022112089003174

[24] Kim John, M. P. (1987). Turbulence statistics in fully developed channel flow at low Reynolds number. *Journal of Fluid Mechanics, 177*, 133 – 166.

[25] Klebanoff, P. S. (1955). *Characteristics of Turbulence in Boundary Layer with Zero Pressure Gradient.*

[26] Klewicki, J., & Falco, R. (1989). On accurately measuring statistics associated with small-scale structure in turbulent boundary layers using hot-wire probes. *Journal of Fluid Mechanics, 219*, 119-142. doi:10.1017/S0022112090002889

[27] Kline, S. J., Reynolds, W. C., Schraub, F. A., & Runstadlers, P. W. (1967). The structure of turbulent boundary layers. *Journal of Fluid Mechanics, 30(4)*, 741-773. doi:10.1017/S0022112067001740

[28] Kreplin , H.-P., & Eckelmann, H. (1979). Behavior of the three fluctuating velocity components in the wall region of a turbulent channel flow. *The Physics of Fluids, 22*, 1233. doi:https://doi.org/10.1063/1.862737

[29] Laufer, J. (1948). *Investigation of turbulent flow in a two-dimensional channel.* Dissertation (Ph.D.), California Institute of Technology. doi:10.7907/6ZYC-HJ88

[30] Lavoie, P., Avallone, G., de Gregorio, F., Romano, G. P., & Antonia, R. A. (2007). Spatial resolution of PIV for the measurement of turbulence. *Experiments in Fluids, 43(1)*, 39-51. doi:10.1007/s00348-007-0319-x

[31] Lilach, S., & René, v. H. (2011). Measurements of pollen grain dispersal in still air and stationary, near homogeneous, isotropic turbulence. *Journal of Aerosol Science, 42*, 867-882. doi:10.1016/j.jaerosci.2011.08.001

[32] Lundell, F., Söderberg, L. D., & Alfredsson, P. H. (2011). Fluid Mechanics of Papermaking. *Annual Review of Fluid Mechanics, 43*, 195-217. doi:10.1146/annurev-fluid-122109-160700

[33] Marusic, I., & Kunkel, G. J. (2003). Streamwise turbulence intensity formulation for flat-plate boundary layers. *Physics of Fluids, 15*, 2461. doi:https://doi.org/10.1063/1.1589014

[34] Moffet, R. C., & Prather, K. A. (2009). In-situ measurements of the mixing state and optical properties of soot with implications for radiative forcing estimates. *Proceedings of the National Academy of Sciences, 106*, 11872-11877. doi:10.1073/pnas.0900040106

[35] Monty, J., & Chong, M. (2009). Turbulent channel flow: Comparison of streamwise velocity data from experiments and direct numerical simulation. *Journal of Fluid Mechanics, 633*, 461-474. doi:10.1017/S0022112009007769

[36] Moser, R. D., Kim, J., & Mansour, N. N. (1999). Direct numerical simulation of turbulent channel flow up to Ret=590. *Physics of fluid, 11(4)*, 943. doi:https://doi.org/10.1063/1.869966

[37] MulberryDesign. (2022, 8). *Lasers for PIV.* Retrieved 9 10, 2022, from litron.co.uk: https://litron.co.uk/product-range/lasers-for-piv/ld60-532-piv-series/

[38] Nickels, T. B., & Marusic, I. (2001). On the different contributions of coherent structures to the spectra of a turbulent round jet and a turbulent boundary layer. *Journal of Fluid Mechanics, 448*, 367–385. doi:10.1017/S002211200100619X

[39] O'Connor, M. C. (2014, October Monday 27). *www.theguardian.com*. Retrieved from Inside the lonely fight against the biggest environmental problem you've never heard of: https://www.theguardian.com/sustainable-business/2014/oct/27/toxic-plastic-synthetic-microscopic-oceans-microbeads-microfibers-food-chain

[40] Pedley, T. J., & Kessler, J. O. (1992). Hydrodynamic Phenomena in Suspensions of Swimming Microorganisms. *Annual Review of Fluid Mechanics, 24*, 313-358.

[41] Pope, S. B. (2018). *Turbulent Flows.* Cornell University: Cambridge Univeristy Press.

[42] Raffel, M., Willert, C. E., Fulvio, S., Kähler, C. J., Wereley, S. T., & Kompenhans, J. (2018). *Particle Image Velocimetry.* Switzerland: Springer.

[43] Reichardt, H. (1938). Messungen turbulenter Schwankungen. *The science of nature, 26*, 404–408.

[44] Ross, P., Chastain, S., Vassilenko, E., & al, e. (2021). Pervasive distribution of polyester fibres in the Arctic Ocean is driven by Atlantic inputs. *Natural Communication, 12*, 106 . doi:10.1038/s41467-020-20347-1

[45] Scharnowski, S. B., & Kähler, C. (2019). Accurate turbulence level estimations using PIV/PTV. *Experiments in Fluids, 60(1)*. doi:10.1007/s00348-018-2646-5

[46] Shin, M., & Koch, D. L. (2005). Rotational and translational dispersion of fibres in isotropic turbulent flows. *Journal of Fluid Mechanics, 540*, 143-173. doi:10.1017/S0022112005005690

[47] Suaria, G., Achtypi, A., Perold, V., & al, e. (2020). Microfibers in oceanic surface waters: A global characterization. *Science Advances, 6*. doi:10.1126/sciadv.aay8493

[48] Thielicke, W. (2021). *PIVlab tutorial*. Retrieved 7 2022, from pivlab.blogspot: https://pivlab.blogspot.com/p/blog-page_19.html

[49] Timmins, B., & Wilson, B. (2012). A method for automatic estimation of instantaneous local uncertainty in particle image velocimetry measurements. *Experiments in fluid, 53*, 1133-1147. doi:10.1007/s00348-012-1341-1

[50] Townsend, A. A. (1956). *The Structure of Turbulent Shear Flow.* Cambridge University Press.

[51] *VEO-E 340L*. (2012). Retrieved 7 2022, from phantomhighspeed: https://www.phantomhighspeed.com/products/cameras/veo/veoe340l

[52] Voth, G. A., & Soldati, A. (2017). Anisotropic Particles in Turbulence. *Annual Review of Fluid Mechanics, 49*, 249-276 . doi:10.1146/annurev-fluid-010816-060135

[53] Vreman W., K. J. (2014). Comparison of direct numerical simulation databases of turbulent channel flow at Reτ = 180. *Physics of Fluids, 26*. doi:https://doi.org/10.1063/1.4861064

[54] Wilson, B. M., & Smith, B. L. (2013). Uncertainty on PIV mean and fluctuating velocity due to bias and random errors. *Measurement Science and Technology, 24(3)*. doi:10.1088/0957-0233/24/3/035302

List of figures

List of tables

Acknowledgement

During these last 8 months I had the opportunity and privilege to work with the Institute of Fluid Mechanics and Heat Transfer at the Technische Universität in Wien. Travelled to Wien for an Erasmus, the great opportunity to write the current thesis was given to me and was unexpected, but it was, with no doubt, the most exciting chance life ever gave to me. This opportunity made me live other months in the beautiful city of Wien with the most wonderful people, collecting the most beautiful experiences. Through these months I learned so much and I will always appreciate it. This is the reason why the first person I would like to thank is my co-relator, Professor Alfredo Soldati, who offered me this chance and believed in me from the first moment, together with all the advises and support that were needful for the realization of this thesis. For sure I need to thank also my relator Professor Giacomo Montenegro that also was so patient and so supportive, despite the difficulties of online meetings. I would also like to thank my supervisor Dr. Giuseppe Caridi, who for sure lighted in me the interest and the curiosity, made me learn a lot through these months and made me maybe more incisive than I was. I cannot miss to also thank my supervisor and colleague Vlad Giurgiu, who started my path and was always ready to help, support and advise me.

I will always be grateful for this opportunity and happy for the choice I made of starting in Wien my Master thesis and I will always bring with me the lectures, the advises and the experience.